

QC852
.C6
no.438
ATSL

OBSERVATIONS OF THUNDERSTORM OUTFLOWS
FROM DOPPLER RADAR AND
SURFACE MESONETWORK DATA

LIBRARIES
APR 10 1989
COLORADO STATE UNIVERSITY

BY
ROBERT EDWARD DATTORE

Principal Investigator: Peter C. Sinclair



**DEPARTMENT OF
ATMOSPHERIC SCIENCE**

PAPER NO.

438

OBSERVATIONS OF THUNDERSTORM OUTFLOWS FROM DOPPLER RADAR
AND SURFACE MESONETWORK DATA

by
Robert Edward Dattore

This report was prepared with support provided by the
National Science Foundation under Colorado State University
Contract AEO-8420980

Principal Investigator: Peter C. Sinclair

Department of Atmospheric Science
Colorado State University
Fort Collins, Colorado 80523

March 1989

Atmospheric Science Paper No. 438

QC852
C6
no. 438
ATSL

ABSTRACT

Observations of thunderstorm outflows and gust fronts are made from Doppler radar and surface mesonet network data. These data are used to determine the validity of the assumption of mass balance for the outflow-downdraft system, and to assess the accuracy of the empirical relationship derived from density current theory in predicting the propagation speed of the gust front. In addition, the combination of radar and surface data are used for analysis of the outflow and gust front, and several features which are characteristic of outflows and gust fronts are revealed by these analyses. The data used are taken from two experiments which were designed for studying thunderstorms and outflows. These programs are the MICROburst and SEVERE THUNDERSTORM (MIST) program of Summer, 1986, operated near Huntsville, AL, and the CONVECTIVE INITiation and DOWNBURST EXPeriment (CINDE) of Summer, 1987, operated near Denver, CO. Both programs had associated research Doppler radars, surface mesonet networks, and some sounding systems. From these data, eight outflow-gust front cases were obtained, three from MIST and five from CINDE. It is believed that this study represents the largest collection of Doppler radar and surface mesonet network supported outflow-gust front cases to date. The results of this study show that from mass balance for the outflow-downdraft system, reasonable calculations of the downdraft speed required for this mass balance to be realized are obtained. These calculations are determined to be reasonable by comparison with downdraft speeds observed by previous researchers from aircraft penetrations and numerical modelling studies. The empirical density current approximation is found to be inadequate in predicting the gust front speeds of this study, with some errors as much as 50% and an average error of 37%. It is found that, in addition to the hydrostatic pressure difference across the gust front, the airflow within the outflow and in the environment also significantly affect the gust front propagation speed, and the density current equation is modified to include these effects. This modified equation is then found to produce a different value for k than has been agreed upon previously by researchers. With

the new k -value and the above modifications, the density current approximation predicts the gust frontal speeds with a maximum error of 12% and an average error of 5%, exhibiting significant improvement over the unmodified density current relationship. The analyses derived from the radar and surface data reveal a variety of characteristics of thunderstorm outflows and gust fronts which have been previously observed. These include the marked gradients in temperature, dewpoint, wind speed, and pressure which exist across the front, as well as convergence along the entire length of the front and at gust front intersection points. Also noted is rotation in bends and clefts in the front, and in the analyses in which downdrafts are present, the downdrafts are observed to always be characterized by anticyclonic rotation.

ACKNOWLEDGEMENTS

I wish to express my gratitude to my adviser, Dr. Peter C. Sinclair, for his support and guidance, without whom this study would not have been possible. I would also like to thank the other members of my graduate committee, Dr. Richard H. Johnson and Dr. V. N. Bringi, for their helpful advice and suggestions. Much of the data for this study was archived at the National Center for Atmospheric Research in Boulder, CO, and special thanks go to Bob Rilling, who supplied me with data, often on a moment's notice. Other data was provided by the MIT Lincoln Laboratory under the sponsorship from the Federal Aviation Administration. Finally, special thanks go to Becky Armstrong for her immense help with and super knowledge of the word processing system with which this thesis was typed, and to Judy Sorbie for the fantastic drafting of many of the figures. This report was prepared with support provided by the National Science Foundation under Colorado State University Contract AEO-8420980.

Table of Contents

1	INTRODUCTION	1
2	PREVIOUS RESEARCH	4
2.1	Outflow observational studies	4
2.1.1	Early research	4
2.1.2	Doppler radar and other recent studies	6
2.2	Outflow modelling studies	8
2.3	Density current application to thunderstorm outflows	9
2.3.1	Density current theory	11
2.3.2	Gust front speed from density current equation	11
2.4	Brief discussion of some downdraft studies	12
2.5	Summary	14
3	DATA AND ANALYSIS	16
3.1	Data sources and types	16
3.1.1	Radar data systems	16
3.1.2	Surface networks	17
3.2	Method of analysis	19
3.2.1	Surface Analysis	19
3.2.2	Radar Analysis	19
4	CASE STUDIES AND RESULTS	27
4.1	MIST cases	27
4.1.1	14 July 1986	27

4.1.2	25 July 1986	43
4.1.3	31 July 1986	54
4.2	CINDE cases	63
4.2.1	27 June 1987	68
4.2.2	28 July 1987	82
4.2.3	6 August 1987	92
4.3	Summary	99
4.4	Gust front speed prediction	102
5	CONCLUSION AND FURTHER RESEARCH	108

List of Figures

2.1	Schematic diagram of a thunderstorm outflow.	7
2.2	Schematic diagram of a laboratory density current.	10
3.1	Surface station mesonetworks and Doppler radar positions for a) the MIST program and b) the CINDE program.	18
3.2	Typical meteorological traces associated with the passage of a gust front.	20
3.3	Graphical representation of the downdraft and outflow, showing the parameters required for mass balance.	22
3.4	PPI scans of a downdraft and outflow showing how both can be bounded.	25
3.5	RHI scan of radial velocity showing the height of an outflow.	26
4.1	Soundings for 14 July in both pre-storm and post-storm environments.	30
4.2	PPI scans of reflectivity and radial velocity at 17:45 on 14 July.	32
4.3	RHI scans of reflectivity and radial velocity at 17:45 through the outflow of 14 July.	33
4.4	Isochrones of the leading edge of the gust front of 14 July.	35
4.5	Streamline and isotach analysis at 18:45 on 14 July 1986.	37
4.6	PPI scan of radial velocity at 18:42 on 14 July.	38
4.7	Dry-bulb and dewpoint temperature analysis at 18:45 on 14 July.	40
4.8	Surface pressure field at 18:45 on 14 July.	41
4.9	Divergence and vorticity fields at 18:45 on 14 July.	42
4.10	PPI scans of reflectivity and radial velocity at 15:47 on 25 July.	45
4.11	RHI scans of reflectivity and radial velocity through the outflow of 25 July.	46
4.12	Isochrones of the leading edge of the gust front of 25 July.	48

4.13	Streamline and isotach analysis at 17:10 on 25 July 1986.	49
4.14	Dry-bulb and dewpoint temperature analysis at 17:10 on 25 July.	51
4.15	Surface pressure field at 17:10 on 25 July.	52
4.16	Divergence and vorticity fields at 17:10 on 25 July.	53
4.17	Soundings for 31 July in both the pre-storm and post-storm environments..	55
4.18	PPI scans of reflectivity and radial velocity at 13:35 on 31 July.	57
4.19	RHI scan of reflectivity and radial velocity at 13:35 through the outflow of 31 July.	58
4.20	Isochrones of the leading edge of the gust front of 31 July.	61
4.21	Streamline and isotach analysis at 13:50 on 31 July.	62
4.22	PPI and RHI scans of radial velocity at 13:51 on 31 July.	64
4.23	Dry-bulb and dewpoint temperature analysis at 13:50 on 31 July.	65
4.24	Surface pressure field at 13:50 on 31 July.	66
4.25	Divergence and vorticity fields at 13:50 on 31 July.	67
4.26	PPI scans of reflectivity and radial velocity at 14:12 on 27 June.	71
4.27	RHI scans of reflectivity and radial velocity through the storm and outflow of GF A on 27 June.	72
4.28	Isochrones of the leading edge of GF B of 27 June.	75
4.29	Streamline and isotach analysis at 17:00 on 27 June.	77
4.30	PPI and RHI scans of radial velocity at 16:58 on 27 June.	78
4.31	Dry-bulb and dewpoint temperature analysis at 17:00 on 27 June.	79
4.32	Surface pressure field at 17:00 on 27 June.	80
4.33	Divergence and vorticity fields at 17:00 on 27 June.	81
4.34	PPI scan of reflectivity and radial velocity at 16:57 on 28 July.	84
4.35	RHI scan of reflectivity and radial velocity at 16:57 through the outflow and storm of GF Y of 28 July.	85
4.36	Isochrones of the leading edge of the gust fronts of 28 July.	87
4.37	Streamline and isotach analysis at 17:10 on 28 July.	88
4.38	PPI scan of radial velocity at 17:09 on 28 July.	89

4.39	Dry-bulb and dewpoint temperature analysis at 17:10 on 28 July.	90
4.40	Surface pressure field at 17:10 on 28 July.	91
4.41	Divergence and vorticity fields at 17:10 on 28 July.	93
4.42	Isochrones of the leading edge of the gust front of 6 August.	94
4.43	Streamline and isotach analysis at 17:10 on 6 August.	95
4.44	Dry-bulb and dewpoint temperature analysis at 17:10 on 6 August.	96
4.45	Surface pressure analysis at 17:10 on 6 August.	97
4.46	Divergence and vorticity fields at 17:10 on 6 August.	98

List of Tables

2.1	Summary of downdraft speeds from aircraft penetrations.	13
3.1	Radar operating characteristics of MIST and CINDE radars.	17
4.1	Surface observations associated with gust front passages in MIST.	28
4.2	Mass balance calculations of downdraft speeds from the outflow of 14 July.	34
4.3	Mass balance calculations of downdraft speeds from the outflow of 25 July.	47
4.4	Mass balance calculations of downdraft speeds from the outflow of 31 July.	59
4.5	Surface observations associated with gust front passages in CINDE.	69
4.6	Mass balance calculations of downdraft speeds from the outflow of GF A of 27 June.	73
4.7	Mass balance calculations of downdraft speeds from the outflow of GF Y of 28 July.	86
4.8	Summary of the average downdraft speeds calculated for the five cases in MIST and CINDE.	99
4.9	Density current predictions for gust front speeds in MIST and CINDE.	103
4.10	Recalculations of k for the gust front speeds in MIST and CINDE from the modified density current approximation.	105
4.11	Recalculations of MIST and CINDE gust front propagation speeds from a modified density current approximation and $k=0.87$	106

Chapter 1

INTRODUCTION

When the downdraft air of a thunderstorm reaches the surface, it spreads outward as a pool of cool air. This pool of air is called the thunderstorm outflow, and its leading edge is defined as the gust front. With the passage of the gust front, a wind shift and increase, a temperature drop, and a pressure rise are all observed at the surface. The dewpoint temperature also changes, either increasing or decreasing, depending on the environment through which the gust front passes.

Gust fronts and outflows have become the focus of much research in recent years for several reasons. Gust fronts have been identified by several researchers as regions of large horizontal wind shears which may be hazardous to aircraft operations during takeoff and landing (Greene *et al.*, 1977; Zrnica and Lee, 1983; Fulton and Zrnica, 1985; Harris *et al.*, 1985). The gust front is also recognized for its effects on convection. A region that has been overrun by an outflow tends to be an area of suppressed convection while the gust front itself tends to be a location of enhanced convergence, strengthening existing convection and even being responsible for the production of new convection. Collisions of gust fronts with other gust fronts or other boundaries have also been observed by satellite (Purdom, 1979, 1986), radar (Weaver and Nelson, 1982; Wilson and Schreiber, 1986; Mueller and Carbone, 1987), and numerical models (Droegemeier and Wilhelmson, 1982, 1985a, 1985b) to be instrumental in the production of new convection.

Previous research in the area of gust fronts and outflows includes everything from the observed weather changes with a gust front passage to gust front and outflow speed and vertical structure to effects on the enhancement of new convection. While it is known that

the downdraft air of the parent thunderstorm is directly responsible for the gust front and outflow, most of this research has treated them separately. There have, however, been some numerical modelling studies which couple the downdraft and outflow in some way.

One of the focal points of this research is to couple the downdraft and outflow in such a way as to provide evidence supporting the idea that the downdraft is the sole source of air responsible for outflow formation, and that entrainment into and mixing out of the top and sides is negligible. A second focus of the research is to examine the adequacy with which the empirically derived density approximation for thunderstorm gust fronts predicts gust front propagation speed. It is found that, in the seven cases provided here, this approximation fails to predict the gust frontal speeds with an accuracy below 15% error, indicating the need for modification of this equation. With the modification proposed by this study, however, the equation shows marked improvement in speed prediction, with generally less than 10% error. The third focus of this research is to combine radar and surface mesonet network analysis so as to illustrate some of the features associated with outflows and gust fronts which are revealed by these analyses. It is believed that, although there have indeed been more-detailed outflow-gust front studies from one or two cases, this study represents the largest collection of Doppler radar and surface mesonet network supported outflow-gust front cases to date.

The research is accomplished by use of Doppler radar, surface mesonet network, and sounding data from two experiments that were designed for studying thunderstorm systems. The two experiments are the MIST (MIcroburst and Severe Thunderstorm) and CINDE (Convective INitiation and Downburst Experiment) programs operated near Huntsville, AL in 1986 and Denver, CO in 1987, respectively. From the radar data for five cases (three from MIST and two from CINDE), measurements of the outflows and downdrafts are made which then lead to calculations of the downdraft air speeds from the assumption of mass balance. The surface data is used for the study of gust front speed prediction for seven gust front cases (three from MIST and four from CINDE).

This thesis begins with a discussion of previous research related to this study and ends with suggestions for further research into gust fronts and outflows. The second chapter

brings the reader from the past up to the present on research in the area of gust fronts and outflows. It is evident from this summary that research coupling the downdraft and outflow is lacking. The topic of gust front speed is also discussed, including the theory behind the density current approximation, which is not observed to work adequately in predicting the gust front speeds of the seven cases. The third chapter describes the data and the data sources used for this research, and discusses the methods used to analyze this data. The fourth chapter presents the case studies and the results obtained from the outflow measurements and examines the prediction of the gust front speeds, and the fifth and final chapter presents the conclusions drawn from this study and leads the reader into the future in terms of what areas could benefit from further study and in what ways this might be accomplished.

Chapter 2

PREVIOUS RESEARCH

This chapter leads the reader from the past through to the present in research on thunderstorm gust fronts and outflows. Various observational studies (surface network, instrumented tower, and Doppler radar) and numerical modelling studies are examined, and the major contributions to the knowledge on the phenomena of outflows and gust fronts are highlighted. It should become apparent from the literature review that aside from a few modelling studies, the research has not coupled the downdraft and outflow, but rather has treated them separately. The chapter then continues by studying the theory behind the density current equation, as well as what modifications have been introduced to make it applicable to gust fronts and outflows in the atmosphere. The chapter ends with a brief discussion on some downdraft studies which have produced measurements of downdraft speeds, as this information will be used in comparison with some of the calculations of Chapter 4.

2.1 Outflow observational studies

2.1.1 Early research

It has been known, as far back as the early 1900's, that the thunderstorm downdraft is responsible for the typically observed strong, gusty winds which precede the onset of the rainfall. Humphreys (1914) made note of this phenomena associated with the thunderstorm in his paper, and from traces from the Weather Bureau, he observed that along with the strong winds, there is a pressure rise, wind shift, and temperature drop at the surface prior to the onset of precipitation. He attributed the strong winds, pressure rise, and

temperature drop to the downdraft and deduced that evaporation of raindrops within the downdraft causes cooling, establishing a downrush of air, which upon reaching the surface, rushes out horizontally along the surface. He noted that this colder air underruns the warmer ambient air, causing it to rise, and thus helping to maintain the thunderstorm updraft. These observations, though very informative on thunderstorm phenomena, were made simply through personal observations of thunderstorms.

In the mid-1940's, after World War II, there was a need for a great deal more information on the thunderstorm as it affected aircraft operations. From this came the idea for a large-scale experiment for the study of thunderstorms, and the Thunderstorm Project was set up in Florida. Byers and Braham (1949) summarize what was learned about thunderstorms in their report on the Thunderstorm Project. They were the first to observe the phenomena of the outflow and gust front. They noted that when the downdraft of a thunderstorm reaches the ground, it spreads out in what they called a divergent wind, thus recognizing that the downdraft and outflow of a thunderstorm are directly related. Through their observations of outflows and gust fronts, Byers and Braham learned things such as how the downdraft spreads out at the ground in an asymmetrical outflow in the direction of cell motion, with a well-defined leading edge that they called the "micro-cold" front and a diffuse trailing edge. They noted the same pressure, wind, and temperature changes associated with a gust front passage that Humphreys had seen prior to the onset of the precipitation, and they observed that as the gust front undercuts the warmer, ambient air, that air is lifted, helping to maintain the parent thunderstorm, and even causing new thunderstorm development.

In 1958, a 3 cm radar located at Texas A & M observed on a number of days echoes which were termed "thin lines" (Brown, 1960). These linear radar echoes appeared to originate at or near thunderstorm echoes. With the aid of a surface network surrounding the radar and capable of temperature, pressure, and wind measurements, Brown noted that the weather changes associated with the passage of the radar thin lines were the same as with a gust front passage. From this information, he concluded that the thin line (a gust front) was a boundary separating air modified by a thunderstorm downdraft (an outflow)

from the surrounding environment. These observations were the first to show that a radar is capable of "seeing" gust fronts.

Once the outflow and gust front were recognized as a part of the thunderstorm system and observed with a standard radar, observational studies of these weather phenomena became abundant. Earlier observations (late 1960's through mid-1970's) were made using surface station networks and instrumented towers (Goldman and Sloss, 1969; Charba, 1974; Goff, 1975, 1976). These studies provided detailed information on the meteorological events accompanying the gust front at the surface as well as a picture of the vertical structure of the gust front.

Goldman and Sloss (1969) were the first to use data from an instrumented tower for outflow research. Though only the lowest 150 m of the outflow were sampled, they were able to provide quantitative data on the vertical wind shears accompanying a gust front, as well as obtaining some idea of the vertical structure of an outflow.

Charba (1974) provided a detailed study of the lower portion of a gust front using data from a 444 m tower. Some of the significant features noted were a pressure jump that consistently preceded the gust front, large wind and temperature gradients in the frontal zone, a vertical bulge or head at the leading edge of the outflow, and an undercurrent and upward motion in the nose (fig. 2.1). Charba also noted cross-frontal wind shears more than ten times greater than the along-front shear values. Goff (1975, 1976) also studied the vertical structure of the outflow, noting how the gust front shape varies throughout its life cycle.

2.1.2 Doppler radar and other recent studies

While the instrumented tower provided a great deal of information on the structure and life cycle of a thunderstorm outflow, it can only sample the lower 0.5 km of an outflow which may be as deep as 2 km. Additionally, the tower can only sample the outflow at a single location, limiting the amount of outflow data that could be collected. Outflow studies began to utilize radar data for the observation and analysis of the gust front.

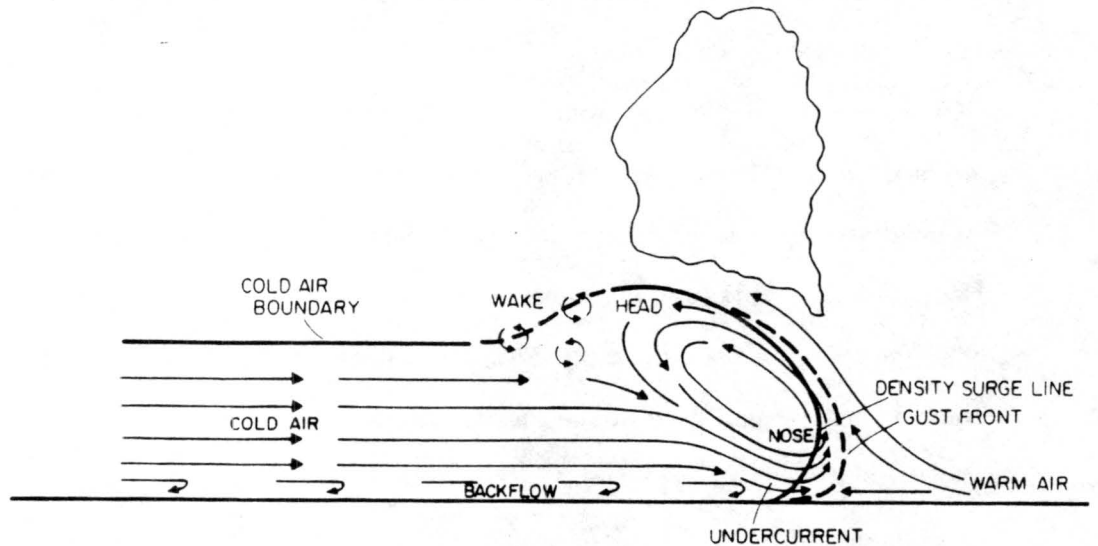


Figure 2.1: Schematic diagram of a thunderstorm outflow, constructed from the work of Charba (1974) and Goff (1975, 1976).

Wakimoto (1982) was the first to observe a gust front with Doppler radar. He observed a thin band of higher reflectivity values associated with the gust front, much the same as did Brown in 1958. From a combination of Doppler and surface network data, Wakimoto was able to expand on the four stages of the gust front lifecycle previously introduced by Goff.

Other Doppler radar observations of gust fronts showed initiation of new convection along the gust front by lifting of the environmental air (Mueller and Carbone, 1987) and initiation of convection associated with gust front intersections (Weaver and Nelson, 1982). Doppler radar data was also studied in terms of its usefulness to aircraft safety, with emphasis on gust front tracking and prediction. Zrnic and Lee (1983) showed that the Doppler spectrum width clearly denoted the gust front position, even when the gust front was aligned *along* a radial, when it would be less likely to be observed in the reflectivity field. Fulton and Zrnic (1985) observed wind shears with Doppler data having values as high as or higher than values associated with Colorado microbursts, and Harris *et al.* (1985) developed an algorithm to delineate areas of wind shear above a threshold level in the Doppler data.

Recent non-Doppler studies of gust fronts include airborne measurements of the vertical velocity field ahead of and within the thunderstorm outflow. The observations of Sinclair

and Purdom (1983, 1984) of Florida and Colorado outflows and Sinclair *et al.* (1988) of both a Colorado and an Alabama outflow show that just ahead of the gust front, there is strong upward motion as the warmer, environmental air rises above the cooler outflow. Gust front penetrations show a well-defined solenoidal circulation within the nose of the outflow, providing strong convergence between outflow and ambient air at the outflow interface, which can be responsible for the development of new convection. Measurements behind the outflow head show a turbulent environment, where mixing of air above and below the outflow interface is occurring. This observation appears to support the existence of Kelvin-Helmholtz instability along the outflow interface behind the head, which has been observed in laboratory density current experiments by Simpson (1969, 1972), in the atmosphere by Mueller and Carbone (1987), and modelled by Droegemeier and Wilhelmson (1986, 1987). The airborne measurements of the Alabama outflow agree well with the measurements of a Doppler wind profiler over which the gust front passed.

2.2 Outflow modelling studies

Several outflow modelling studies have been undertaken in order to examine the structure and dynamics of thunderstorm outflows and gust fronts. Mitchell and Hovermale (1977) investigated the thunderstorm gust front by use of a two-dimensional numerical model. The model maintained a steady downdraft cold source, with $w=17 \text{ ms}^{-1}$, which drove the outflow and gust front. Their findings were especially important at the time since outflow data above tower height was lacking, and the model provided data throughout the entire height of the outflow. Their findings included outflow structural features such as the protruding nose and the elevated head. They observed wind speed and shear profiles within the outflow and across the gust front much the same as found in the observational studies. Additionally, Mitchell and Hovermale observed that soon after the gust front was initiated, the outflow reached a state of constant balance between pressure gradient and surface frictional drag forces. They concluded that the thunderstorm outflow is dynamically similar to a density current.

Droegemeier and Wilhelmson (1987) also used a two-dimensional numerical model for the investigation of thunderstorm outflow dynamics. From the gust front speeds observed in their model experiments, they calculated the internal densimetric Froude number, Fr , for each of their outflow cases and found the values to be somewhat less than that predicted by theory ($Fr=2$) but significantly larger than observed for atmospheric density currents ($Fr=0.75$).

Addis (1984) used a one-dimensional numerical model to simulate the slope, depth, and propagation speed of tropical squall line outflows. The main focus of his research was to relate the dimensions and characteristics of thunderstorm outflows to the dimensions and characteristics of the parent downdrafts. He employed the principle of mass conservation and the assumption of incompressibility in his model experiments, and he assumed that the air speed profile in the downdraft could be approximated by a cosine curve. From these, he calculated the maximum speed required in the downdraft to drive the outflow. Important findings included the observation that a radial outflow, such as from an isolated cell, while being shallower, requires a stronger downdraft to maintain it than the deeper unidirectional outflow such as with a more organized convective system. He also noted that once downdraft cessation has occurred, the radial outflow is found to decay much more rapidly than does the unidirectional outflow.

2.3 Density current application to thunderstorm outflows

A density current is a mass of heavier fluid flowing along a horizontal surface and displacing the less dense ambient environment. The motive force of the density current is the hydrostatic pressure gradient acting across the interface separating the two fluids, and this gradient exists because of the greater hydrostatic pressure within the denser fluid. Some of the commonly observed types of density currents are the displacement of clear water by mud-laden water (turbidity current) and the intrusion of salty water into a mass of fresh water (saline current).

Keulegan (1958) performed density current experiments by releasing a saline solution of greater density into laboratory tanks of fresh water of lesser density. His observations

of these currents formed the basis of what is known about the overall shape of the density current. He noted that a wider current has a longer and flatter frontal head, while a narrower current has a shorter and higher head. From his measurements, he showed that the height of the head is approximately twice the depth of the density current body.

Simpson (1969, 1972) also conducted density current experiments in the laboratory by releasing a saline solution into a tank of fresh water. Observations of the structure of the laboratory-induced density current seemed to compare well with features observed in atmospheric density currents, such as sea-breeze fronts and thunderstorm outflows. Some of these features are the flow pattern within the head, turbulent billows behind the head on the density current interface, an overhanging nose just above the surface, and a lobe and cleft structure along the leading edge of the current. In addition, Simpson found values for the internal Froude number of his laboratory density currents to be similar to the values computed for gust front density currents. Figure 2.2 illustrates a typical laboratory density current, obtained from the observations of both Keulegan and Simpson. The similarity

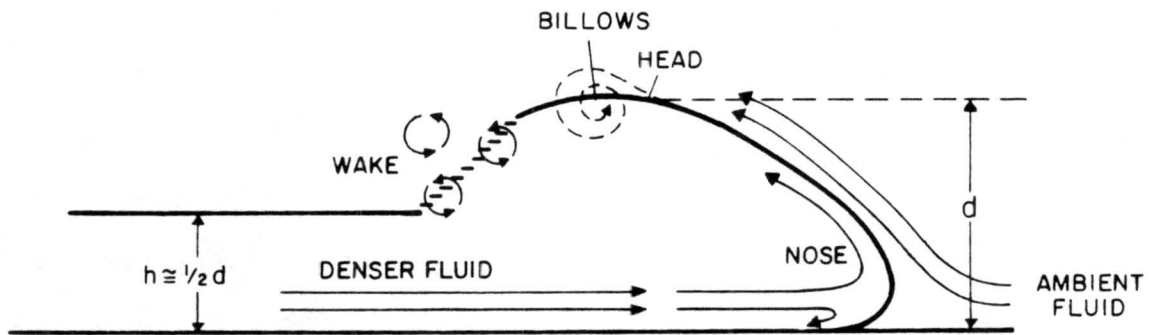


Figure 2.2: Schematic diagram of a laboratory density current, constructed from the work of Keulegan (1958) and Simpson (1969, 1972).

between laboratory and atmospheric density currents can be seen in a comparison of Figs. 2.1 and 2.2.

Along with the laboratory tank experiments described here, both observational and modelling studies led other researchers to conclude that the thunderstorm outflow is dynamically similar to a density current. Charba (1974), in his observational study of a gust front, concluded that the gust front and density current are dynamically similar, where the

pressure gradient forces within the current are balanced by frictional drag at the surface. In numerical modelling investigations of thunderstorm outflows, the results obtained by Mitchell and Hovermale (1977) and Thorpe *et al.* (1980) led them to this same conclusion.

2.3.1 Density current theory

A theoretical analysis of the density current was undertaken by von Kármán (1940), in which he made use of Bernoulli's equation. By assuming a) steady, ideal flow for the density current where there is no friction and b) hydrostatic pressure everywhere along the density current interface, he applied Bernoulli's equation along the streamline separating the heavier fluid from the ambient environment. From this, he obtained a relationship for the propagation speed of the density current, V , equivalent to

$$V = k\sqrt{gH\frac{\rho_2 - \rho_1}{\rho_1}} \quad (2.1)$$

where ρ_2 and ρ_1 are the densities of the heavier fluid and ambient environment, respectively, and H is the mean depth of the density current. This result is confirmed by Benjamin (1968), although he obtained it through a different approach.

From a closer look at Equation (2.1) it is noted that k is the square root of the internal Froude number for the density current, where the internal Froude number is defined as the ratio of inertial to gravitational forces. The value for k obtained by von Kármán is $\sqrt{2}$. For atmospheric density currents, however, the value of k is much less, since von Kármán did not consider the effects of friction. The empirical studies on gust front speed discussed in the next section involuntarily include frictional effects in the computations for the values of k .

2.3.2 Gust front speed from density current equation

A more convenient form of Equation (2.1) may be written

$$V = k\sqrt{\frac{\Delta p}{\rho}} \quad (2.2)$$

where Δp is the difference in the hydrostatic pressure at the surface between the environment and the outflow head and ρ is the environmental density. For the density fluids assumed

in von Kármán's derivation, both (2.1) and (2.2) will give the same result, but for density currents in the atmosphere, the two equations would give different results, since Equation (2.1) addresses the density difference over the height of the outflow, while Equation (2.2) includes the difference throughout the height of the outflow head (Seitter, 1983).

The similarity between thunderstorm outflows and density currents that has been observed has led researchers to apply the density current equation to the propagation speed of the gust front. Wakimoto (1982) notes that researchers generally agree on an average value for $k=0.75$, though the range of k is 0.70–1.08. For three gust front cases that he analyzed, an average value of $k=0.77$ resulted. Seitter (1983) analyzed 20 gust front cases, including the three of Wakimoto, and obtained an average $k=0.79$. The value for k observed by Simpson (1969) in his laboratory tank experiments was 0.75.

2.4 Brief discussion of some downdraft studies

The point of this section on downdraft studies is neither to discuss the evolution of downdraft research nor the processes by which downdrafts are formed and maintained, but rather to provide the reader with some of the results that have been obtained pertaining to the air speeds associated with downdrafts. Then, the results given here may be compared to the resulting calculations for downdraft speeds obtained in this study.

The results of several observational and modelling studies on downdraft speed are summarized here. One of the earliest observational studies of thunderstorm downdrafts is reported by Byers and Braham (1949), when they discuss the results of the Thunderstorm Project. During the experiment, they observed downdraft speeds, measured by airplane in Florida thunderstorms, in the range of less than 3 to about 12 ms^{-1} , with a maximum observed speed of 24 ms^{-1} . In a combined observation-modelling study of downdrafts, Knupp (1987) found downdraft vertical velocities for High Plains thunderstorms to fall in the range of $1\text{--}15 \text{ ms}^{-1}$, and he noted that other downdraft modellers have reported peak vertical velocities of several to $\sim 15 \text{ ms}^{-1}$. Knupp also presented downdraft measurements from aircraft penetrations, and these are given in Table 2.1.

Table 2.1: Summary of downdraft speed from aircraft penetrations, taken from Knupp (1987). For individual references for each measurement, see Knupp (1987).

Location	Downdraft Speed (max/mean) (ms^{-1})	Cloud Type
Florida	8/4.8	Precip. towering Cu
	7/2.5	Cb
	6/4.1	Precip. towering Cu
	23.5/6.8	Cb
Illinois	7.8/3.5	Cb
N.E. Colorado	10/6	Cb
	20/5-10	Cb, some intense
	11/7	Cb
	14/12	Cb, hail
	15/11	Precip. Cu
Oklahoma	10/	Cb
	>20/	Cb
	10-20/8.5	Squall line
Montana	20/	Severe storm

Other modelling study results include those of Addis (1984), which were given in Section 2.2. The speeds he obtained for tropical thunderstorm downdrafts varied from 1 to 11 ms^{-1} , depending on the type of convection with which the downdraft was associated. Srivastava (1985, 1987) found, in two modelling studies of downdrafts typical of the High Plains of Colorado, downdraft speeds mainly in the range of a few to $\sim 20 \text{ms}^{-1}$, with an extreme case of $w=28 \text{ms}^{-1}$.

The observations of the researchers given in this section will be compared to the downdraft speed results obtained for five downdraft-outflow cases in Chapter 4. It will be seen that the results from these cases compare well to the observations noted in this section.

2.5 Summary

This chapter has presented several aspects of thunderstorm outflows and gust fronts revealed by observational and numerical modelling studies. Some of these features will be observed in the analysis which follow in Chapter 4. Also revealed in the literature review of this chapter is the lack of studies coupling the outflow and downdraft. Addis (1984) has attempted to answer the question of whether or not the characteristics of an outflow can lead to some indication of the type of downdraft by showing that different outflow geometries lead to different downdraft speed requirements. Other numerical modelling studies by Mitchell and Hovermale (1977) and Thorpe, *et al.* (1980) have simply used a downdraft in the model to create and maintain the outflow, without saying much else about the relationship between the two. All of these modelling experiments have employed the principle of mass continuity between the downdraft and outflow, so as to generate the outflow, but it appears that nobody has actually shown that mass balance is a good assumption, even though one would think so. Is it possible that there is mass flux into the back of the outflow from the environment if the environmental flow is towards the back of the outflow? Is there mixing out of outflow air into the environment along the outflow top and sides? While this study does not attempt to use the data to specifically answer these questions, the data is used to show whether or not mass continuity is indeed a good assumption, and whether or not

entrainment of air into and mixing of air out of the outflow is appreciable and requires consideration when modelling these phenomena.

Finally, the theory behind density currents has been presented along with how it has been applied to atmospheric gust fronts. The literature makes the approximation appear to be accurate in predicting gust front speed, but this is actually only true in the average. The average value of k even has a range of values from which researchers cannot agree on an exact value, and then these average k -values have ranges of their own, which in many cases is a rather large range. With $k = 0.79$, the approximation is applied to the cases in this study with errors ranging from around 20–50%. Modification is proposed to this approximation which provides marked improvement in the accuracy with which the approximation predicts gust front speed.

Chapter 3

DATA AND ANALYSIS

3.1 Data sources and types

Research Doppler radars and surface instrumented mesonetworks provided the data used in this study. The two sources of these data are the National Center for Atmospheric Research (NCAR) and the FAA Lincoln Laboratory Operational Weather Study (FLOWS). Both NCAR and FLOWS had associated Doppler radars and NCAR provided the surface mesonetworks.

3.1.1 Radar data systems

Doppler radar data for the MIST cases include data from the NCAR CP-2 and the FLOWS FL-2 radars. Table 3.1 gives some of the operating characteristics of these radars. Both radars operated at a wavelength of 10 cm, making them ideal for the observation of gust fronts. Scan modes included both Plan Position Indicator (PPI) and Range Height Indicator (RHI). The elevation increments of the PPI scans varied over time and for each radar, but both radars began scanning at an elevation of 0.0° . Generally, the NCAR CP-2 scanned at elevation increments of 0.5° - 1.0° and the FLOWS FL-2 scanned at increments of 1.0° .

Doppler radar data for the CINDE cases include data from the NCAR CP-3 and the FLOWS FL-2 radars. Table 3.1 gives the operating characteristics for these radars. As in MIST, the FL-2 radar operated at 10 cm, and the NCAR CP-3 radar operated at a wavelength of 5.4 cm. Generally, a longer wavelength radar is more ideal for the observations of gust fronts because it is the turbulence associated with the gust front that is actually

Table 3.1: Radar operating characteristics of MIST and CINDE radars.

Radar	Wave-length (cm)	Beam-width (deg)	Maximum Range (km)	Pulse Repetition Frequency (s^{-1})	Maximum Unambiguous Velocity (ms^{-1})
CP-2	10.67	0.93	156	960	± 12.82
FL-2	10.6	0.96	48-200	690* 1150**	$\pm 18.23^*$ $\pm 30.58^{**}$
CP-3	5.45	1.11	110	1250	± 17.03

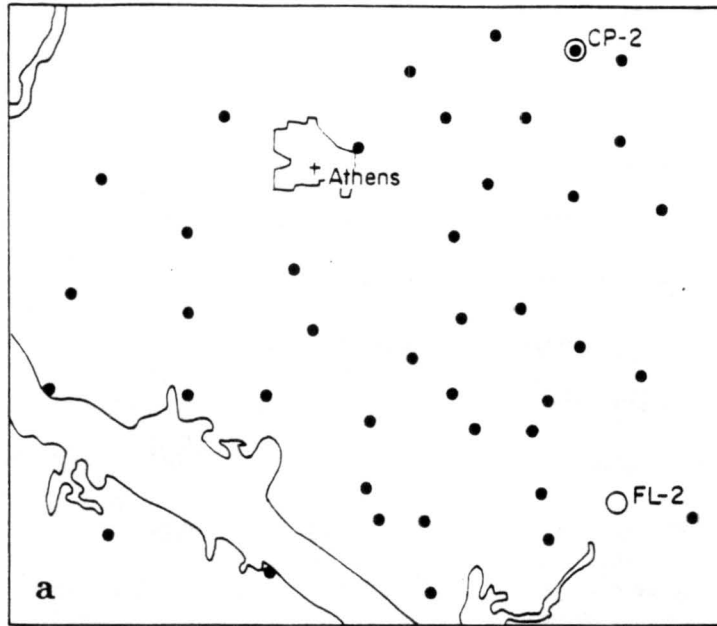
*MIST specifications

**CINDE specifications

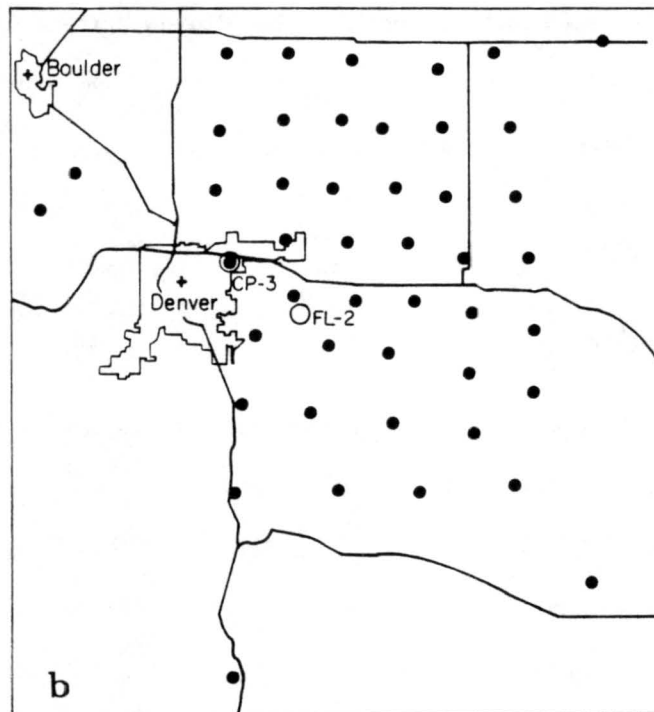
being observed by the radar, and this is accomplished better with longer wavelength radars. An example of a situation where this would not be true is if the gust front is well-defined by insects, and in this case, their small size would make shorter wavelength radars more ideal. While the CP-3 radar had a somewhat less ideal wavelength for gust front observations, this radar data was chosen for one of the days because of the unavailability of CP-2 or FL-2 data, and it appears to be adequate for use in this study.

3.1.2 Surface networks

Surface data was taken from the NCAR second generation **Portable Automated Mesonet (PAM II)** network for both MIST and CINDE. The mesonet stations provided one-minute data averages of temperature, dewpoint temperature, wind speed and direction, and precipitation. Also provided were wind gusts, as well as derived parameters such as the relative humidity. Figure 3.1 displays the PAM II surface networks for both the MIST and CINDE programs, as well as the Doppler radar positions.



0 5 10 km



0 10 20 km

Figure 3.1: Surface station mesonet networks and Doppler radar positions for a) the MIST program and b) the CINDE program.

3.2 Method of analysis

3.2.1 Surface Analysis

Data from the surface mesonetworks of MIST and CINDE are archived on the RDSS VAX computer at NCAR. By use of a software package, developed specifically for the purpose of mesonetwork data perusal and implemented on the NCAR RDSS VAX, time series plots of different meteorological parameters for the individual stations and contour analyses for a single parameter at a given time and for the entire mesonetwork were used for the surface analyses of Chapter 4. The time series plots provided gust front passage times for each station, from which the isochrone analyses were derived, as well as the mesonetwork-calculated gust front propagation speeds. The time series plots also provided temperature and pressure data from which calculations were made of the hydrostatic pressure increase Δp in the head and the density ρ of the environment through which the gust front moved. This information is used in Equation (2.2), the density current approximation to atmospheric gust fronts, to discuss its applicability to the cases of this study. Figure 3.2 shows a typical time series plot at an individual station associated with a gust frontal passage. The contour analyses provide some insights into the characteristics of thunderstorm gust fronts and outflows and examples of these are included in the figures of Chapter 4.

3.2.2 Radar Analysis

Radar data in raw form on magnetic tape were acquired for the MIST and CINDE cases of this study. A software package for use in radar data perusal, editing, and display is also available on the NCAR RDSS VAX, as well as at CSU. A good deal of radar data editing and display were required for the radar analyses of these cases, since parameters for mass continuity are radar-derived. Included in the radar editing process were velocity unfolding, removal of ground clutter, filtering of the reflectivity and velocity fields, and subtraction of storm motion, all for the purpose of displaying the data and extracting the required parameter information for use in the mass continuity equation for downdraft speed. The formulation of this equation follows, as well as how the radar was used in deriving the equation parameter information. Once the radar data had been edited, the scans were

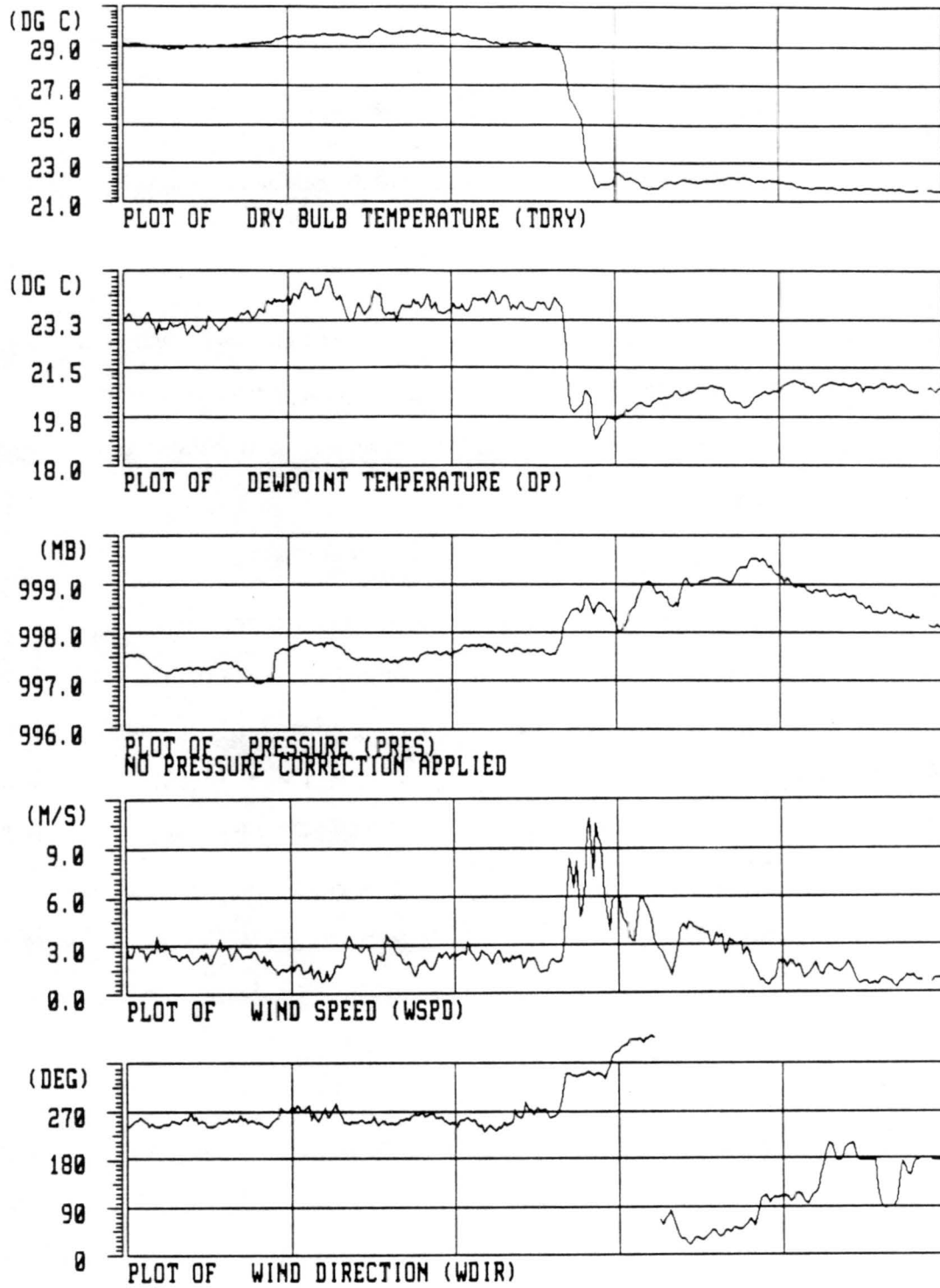


Figure 3.2: Typical meteorological traces associated with the passage of a gust front.

converted to cartesian space with yet another software package developed at NCAR, and these converted scans were displayed in hardcopy, providing the radar analyses of the figures in Chapter 4.

Mass balance for the outflow-downdraft system

The vertical flux of mass in the downdraft W can be expressed by

$$W = \rho w A_{dd} \quad (3.1)$$

where ρ , w , and A_{dd} are the density, air speed, and cross-sectional area of the downdraft, respectively. With the use of Equation (3.1), the equation for the balance of mass of an outflow, where the air flowing out of the downdraft is translated into an increase in the outflow mass, can be written as

$$\frac{\partial(\rho V)}{\partial t} = W \quad (3.2)$$

where ρ and V are the outflow density and volume, respectively.

The density of the outflow air can be considered constant from the gust front back to the downdraft. In an extreme case, the density difference in the outflow from the leading edge back to the downdraft is under 4%. Also, Wakimoto (1982), by scale analysis of the continuity equation, showed that the density variation with height in the outflow may be neglected. Then, if the cross-sectional area of the downdraft is taken at the top of the outflow, where $\rho_{outflow} \approx \rho_{downdraft}$, Equation (3.2) can be integrated with respect to time to obtain a relationship for the average air speed in the downdraft \bar{w} given by

$$\bar{w} = \frac{\Delta V}{\bar{A}_{dd} \Delta t} \quad (3.3)$$

(see Figure 3.3 for a graphical depiction). From Doppler radar data, an outflow volume increase and an average downdraft cross-sectional area can be obtained for some time increment, and Equation (3.3) will yield the average downdraft speed at the top of the outflow. This downdraft speed is then compared with other downdraft speed measurements so as to give an indication of the validity of mass balance for the outflow-downdraft system.

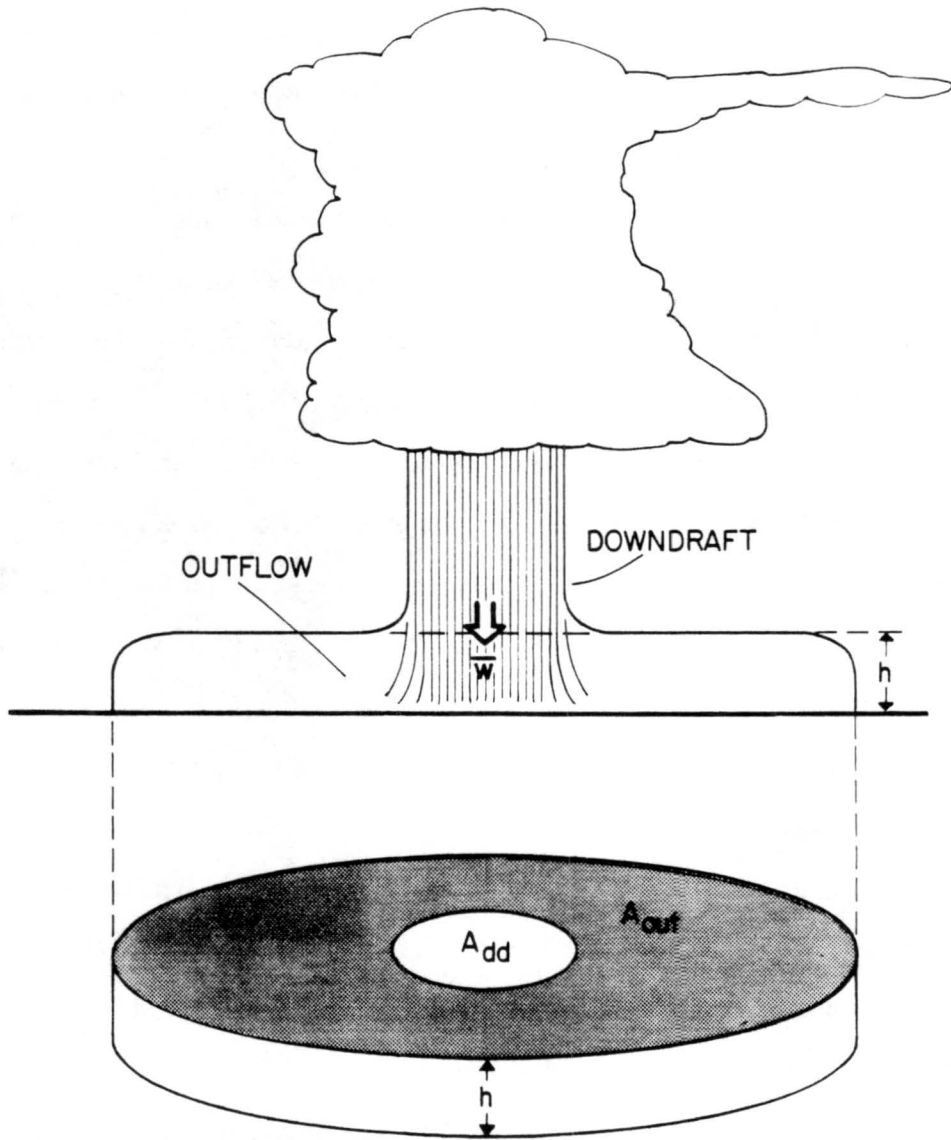


Figure 3.3: Graphical representation of the downdraft and outflow, showing the parameters required for mass balance.

Method for determination of equation parameters

There are three parameters which must be determined so that calculations of \bar{w} from mass balance may be made. These parameters are the outflow areal coverage A_{out} and outflow height h , and the downdraft cross-sectional area A_{dd} . Then, the outflow volume V can be determined from A_{out} and h .

The radar scans provide the three parameters that are required for the calculations of \bar{w} . The outflow leading edge and sides are generally well-defined in the PPI scans in either the radar reflectivity field or the Doppler spectral width, or both. For a radial outflow, the back edge of the outflow is also visible in the reflectivity field and/or spectral width. For a unidirectional outflow, an outflow in which there is one favored direction in which most of the downdraft air moves, this is not the case, and the back edge must be determined from the radial velocity field, and it usually is located not far behind the back side of the convection. For both types of outflow orientations, the outflow boundary is obtainable, and from this, the areal coverage of the outflow can be determined. Figure 3.4 shows how an outflow has been determined from the reflectivity, radial velocity, and spectral width fields, and then bounded. The RHI scans, when available, provide a very good determination of the outflow height h , and when not available, h can be determined from the PPI scans, but with somewhat less accuracy. When RHI scans are available, the top of the outflow is well-defined as a boundary between the outflow and the inflow velocities (see fig. 3.5). Then, A_{out} and h give the outflow volume V .

The downdraft is found by using both the radar reflectivity and radial velocity fields. The downdraft boundaries are centered around the highest reflectivity values, where the heaviest precipitation is occurring, and the boundaries themselves are determined by the radial velocity structure. Since the downdraft cross-sectional area is taken at the top of the outflow, the forward edge of the downdraft often appears in the radial velocity field as the approximately 0 ms^{-1} contour (in a storm-relative frame) separating the storm inflow from the downdraft. The back edge of the downdraft appears in the reflectivity field as a sharp contour in the reflectivity values. From the determination of the downdraft boundaries, the

cross-sectional area A_{dd} can then be figured (see fig. 3.4). These calculations are included for five gust front-outflow cases in Chapter 4.

Once these three parameters have been determined for several different times, the average downdraft speed over this time increment can be calculated from Equation (3.3), and then the result can be compared with the previous downdraft measurements of Table 2.1.

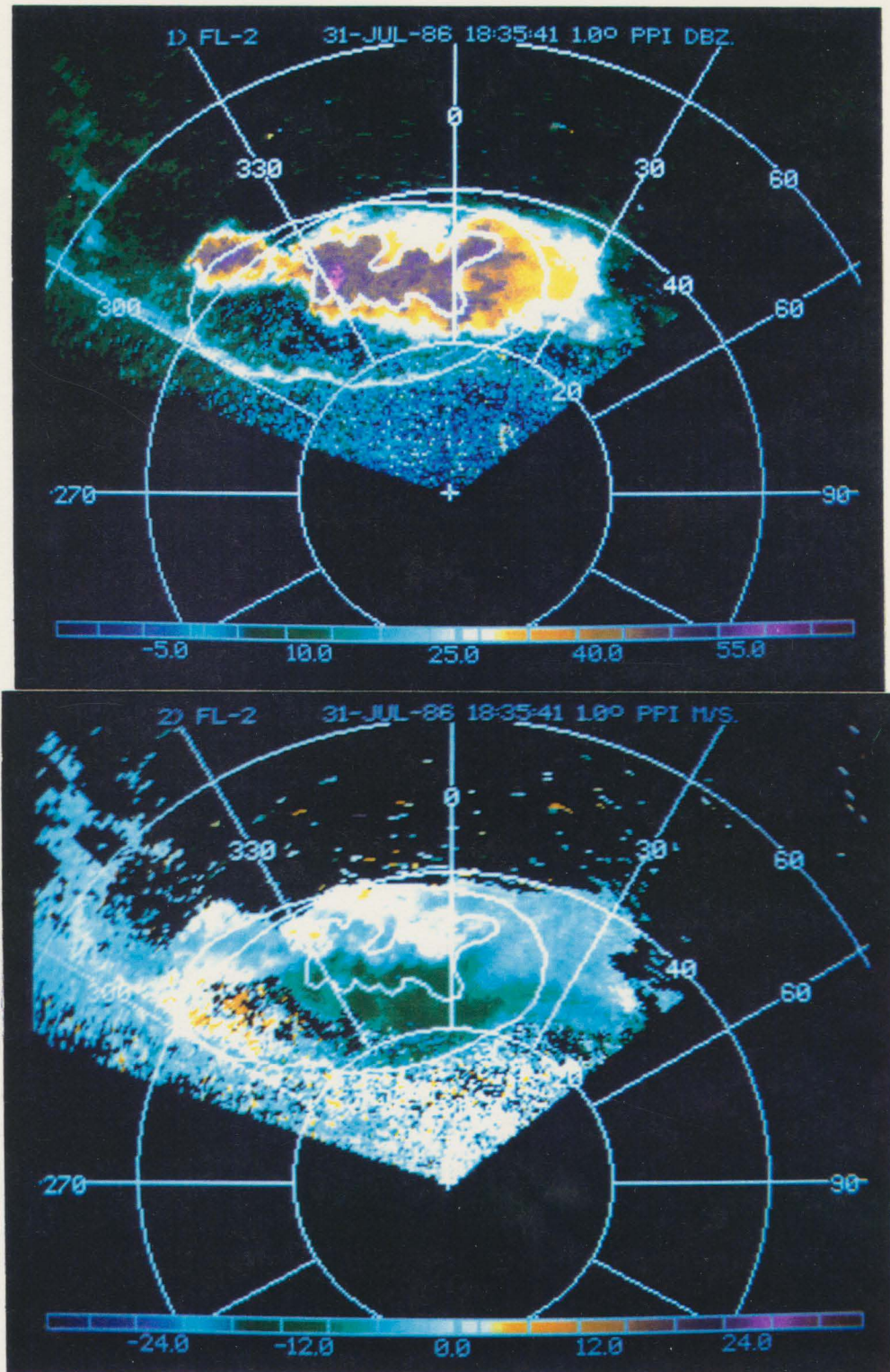


Figure 3.4: PPI scans of (a) reflectivity and (b) radial velocity for an outflow and downdraft. The radar is located at the cross. The downdraft and outflow have been bounded so that their areas can be determined, and the boundary is given in white for both downdraft and outflow. The scan height ranges from 0.3 to 0.6 km AGL from nearest to radar to farthest from radar.

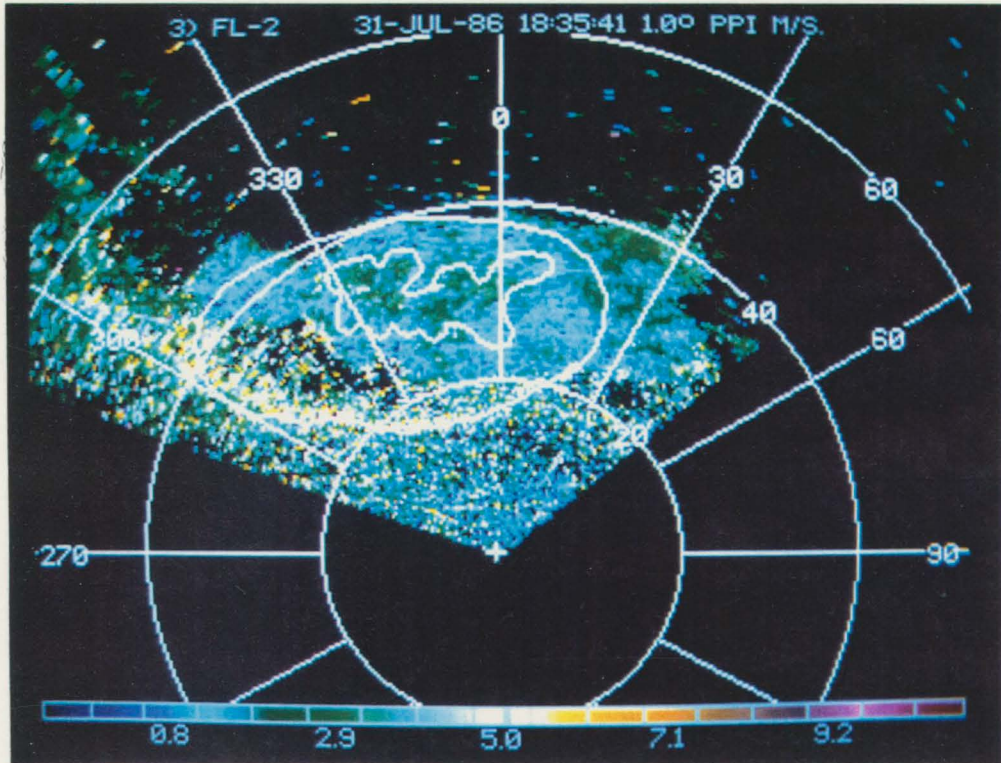


Figure 3.4 continued, showing in (c) the spectral width.

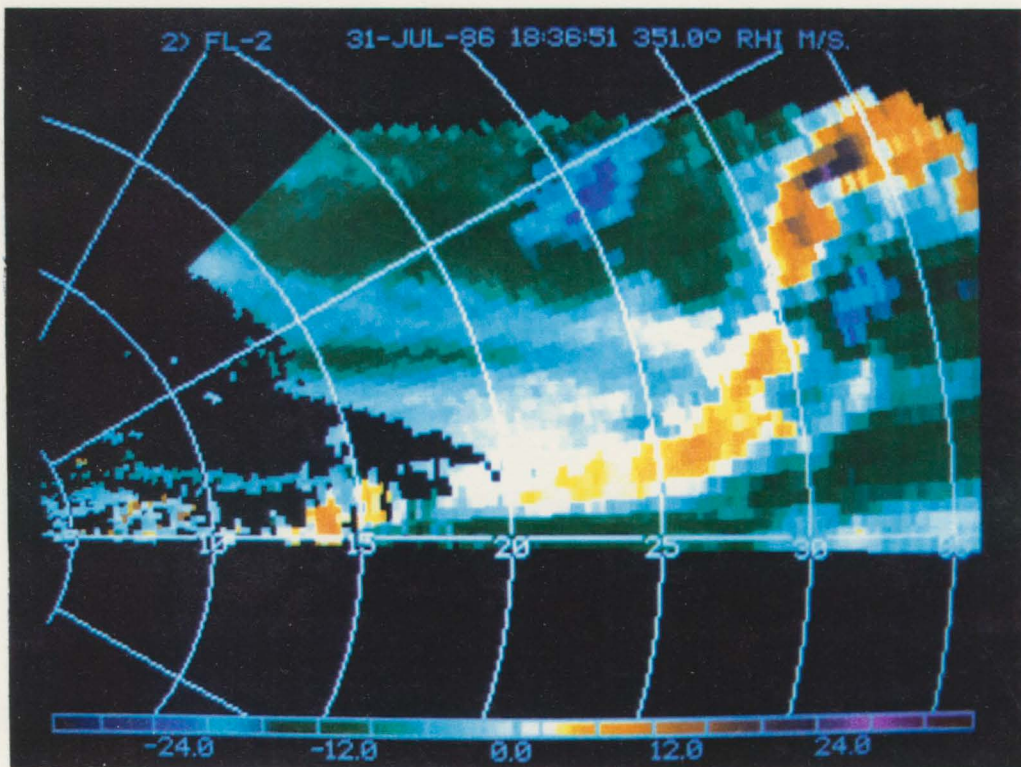


Figure 3.5: RHI scan of radial velocity showing the height of the outflow as the transition between outflow (green) and inflow (yellow) velocities.

Chapter 4

CASE STUDIES AND RESULTS

4.1 MIST cases

The MIST program was run in the summer of 1986 in northern Alabama near Huntsville. MIST ran concurrently with FLOWS and the Satellite Precipitation And Cloud Experiment (SPACE), and all three experiments formed the COoperative Huntsville Meteorological EXperiment (COHMEX) of 1986. The purpose of the MIST program was the study of microbursts and severe thunderstorms, including the study of thunderstorm outflow-gust front systems. Doppler radar and surface mesonet network data proved to be very useful for several outflow-gust front cases during the MIST program.

Three cases in MIST have been chosen for this study. All three cases include a gust front and outflow which is observable by one of the Doppler radars. Each of these storms was a convective system on a larger scale than an isolated thunderstorm, and all three of the outflows associated with these systems had unidirectional configurations. In addition, all three of the gust fronts moved over the PAM II surface mesonet network at some stage in their lifetimes. Table 4.1 summarizes what was observed at the surface with the passage of each gust front through the mesonet. A complete discussion of each case follows in the next three subsections.

4.1.1 14 July 1986

Radar Analysis

During the late afternoon hours of 14 July, a large area of strong convection began to move into observation range of the NCAR CP-2 Doppler radar. This convection was located

Table 4.1: Surface observations from the NCAR PAM II mesonet stations, associated with the passage of each MIST gust front. T , T_d , and p are dry bulb temperature, dewpoint temperature, and pressure, respectively. For the gust fronts of 25 July and 31 July, dewpoint temperature changes are omitted because some stations recorded slight rises in T_d , while other stations reported slight falls.

Date	$\overline{\Delta T}$ (C°)	ΔT_{max} (C°)	ΔT_{min} (C°)	$\overline{\Delta T}_d$ (C°)	$\Delta T_{d_{max}}$ (C°)	$\Delta T_{d_{min}}$ (C°)	$\overline{\Delta p}$ (mb)	Δp_{max} (mb)	Δp_{min} (mb)
14 July 1986	-6.1	-7.8	-2.0	-3.9	-5.8	-2.0	0.70	1.08	0.33
25 July 1986	-3.3	-6.1	-2.1	—	—	—	0.81	1.24	0.44
31 July 1986	-9.1	-12.0	-4.6	—	—	—	0.80	1.41	0.35

well to the northwest of the radar site, and as it moved to the southeast, its associated gust front became visible in the lowest PPI scan. The radar observed the gust front to be moving east-southeastward, and as it did so, it initiated new convection which developed into a multicell system. This new system initiated its own gust front and outflow, and it is this system and its associated outflow that are of interest to this study.

A large area of convection began to move into observation range of the NCAR CP-2 Doppler radar near 16:30 CDT on 14 July. This area of convection was strong, with associated radar reflectivity values of over 60 dBZ and storm tops to over 11 km AGL. The convection was moving southeastward, and its associated gust front appeared in the lowest elevation (0.4°) PPI scan just before 17:00. The radar observed a gust front motion of 12 ms^{-1} towards the east-southeast. Prior to this time, the gust front was not observable by the radar, even in the lowest elevation scan, because of distance from the radar and the curvature of the earth.

At 17:10, the radar observed the first cell to develop along the leading edge of the old outflow. Figure 4.1 shows the observed soundings in both the pre-storm and post-storm environments. The stability indices calculated from the pre-storm sounding indicated the likelihood of some thunderstorm activity for this day. In addition, the pre-storm sounding indicates a Lifting Condensation Level (LCL) of about 900 mb, while the top of the old outflow indicated by the post-storm sounding is 925 mb. From this, it is apparent that the old outflow was deep enough to displace surface air upwards to the LCL, and thus, cause new convective development along its leading edge.

Additional cells quickly continued to develop along the leading edge of the old outflow, and a multicellular system formed behind the gust front. The convection associated with this new system became intense, with reflectivity values of over 65 dBZ and tops to over 12 km AGL. This system began to move east-southward and it initiated a new gust front. By 17:25, the new gust front was observable in the radar scans as a thin band of up to 10 dBZ reflectivity. The new outflow took on a unidirectional configuration as most of the downdraft air spread out in the forward direction.

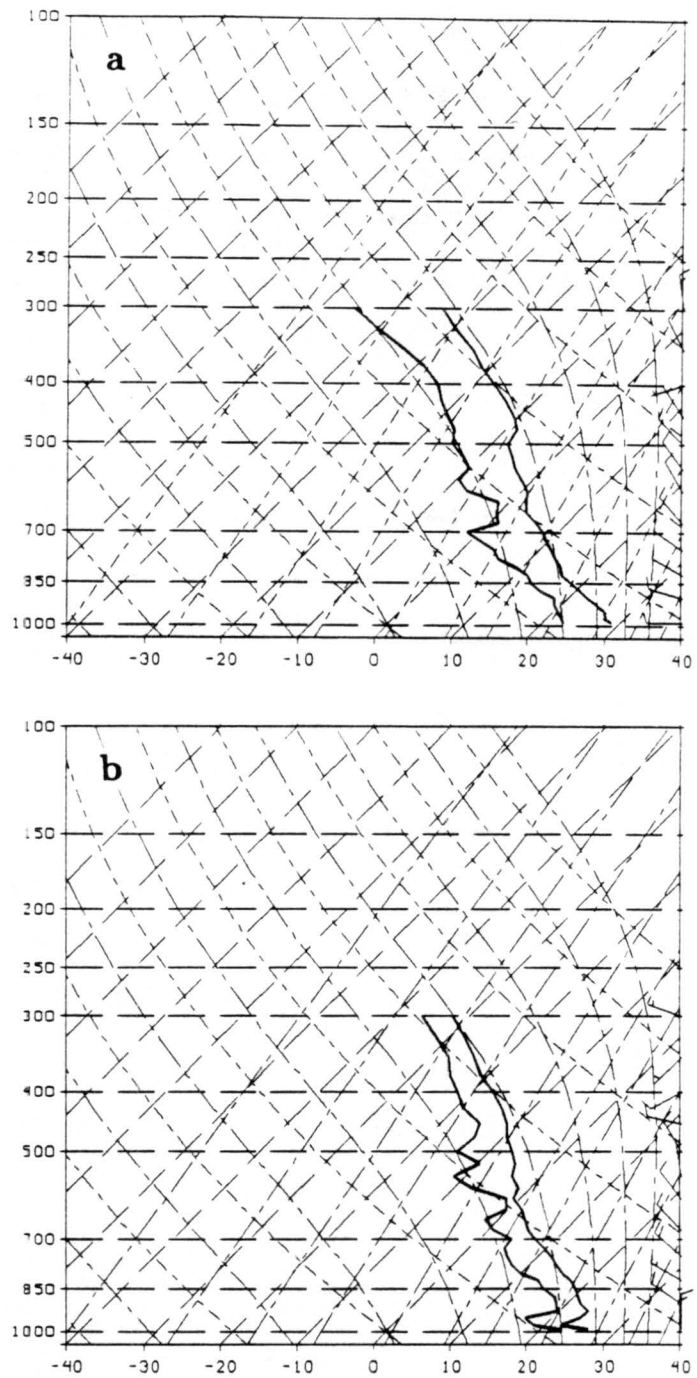


Figure 4.1: Soundings for 14 July in the (a) pre-storm and (b) post-storm environments. The soundings are from St. Joseph, TN, which is about 75 km to the northwest of CP-2. The depth of the old outflow is indicated in the post-storm sounding as a layer of cooler, drier air.

By 17:45, the gust front had moved to over 15 km ahead of the downdraft. The gust front is indicated in Figure 4.2a as a band of up to 10 dBZ reflectivity, and it extended lengthwise for over 60 km, which was indicative of its unidirectional configuration. Outflow air reflectivities were generally below about 3 dBZ. The radar observed a gust front motion of 17 ms^{-1} towards the east-southeast. Figure 4.2b also depicts the gust front location nicely as it appeared as a steep gradient in the radial velocities. Observed wind speeds behind the gust front were $18\text{-}20 \text{ ms}^{-1}$, with speeds as great as 25 ms^{-1} at the base of the downdraft, all in a ground-relative frame. The downdraft was associated with reflectivities $\geq 35 \text{ dBZ}$, and it appeared in the radial velocity field as a core of strongest wind speeds.

An RHI scan through the outflow and downdraft is shown in Figure 4.3. The gust front was about 15 km ahead of the downdraft center. The outflow height was best illustrated in the radial velocity field, which gave an average depth of 2.0 km, making it the deepest outflow of the five cases in this study. The top of the outflow appeared as a sharp gradient in the radial velocities, as did the gust front. Another interesting feature given in Figure 4.3 is the rear inflow that was present into the back of the downdraft. This rear inflow was centered at about 4 km AGL, as indicated by the radial velocity field, and this high momentum air in the mid-levels was being channeled directly into the back of the downdraft.

Calculations for the downdraft air speed were made for a period of more than 21 minutes. During this time, the downdraft was in its mature stage, and just near the end, it began to show the first signs of collapse, so this time period covers the period of strongest downdraft speed. The results of the mass balance calculations are given in Table 4.2. The resulting average speed for the downdraft is 7 ms^{-1} , which is good to $\pm 2 \text{ ms}^{-1}$, and discrete values for \bar{w} varied from 6 to 9 ms^{-1} .

From Table 4.2, it is obvious that the outflow was quite large, owing to its unidirectional nature, as was the downdraft area which was driving it. The outflow volume rate of increase was fairly steady over the 21 minute time period, with the greatest rate of increase between 17:40 and 17:45, which was also the time of maximum downdraft areal coverage and greatest downdraft speed, and hence, mass flux out of the downdraft was at its greatest, accounting

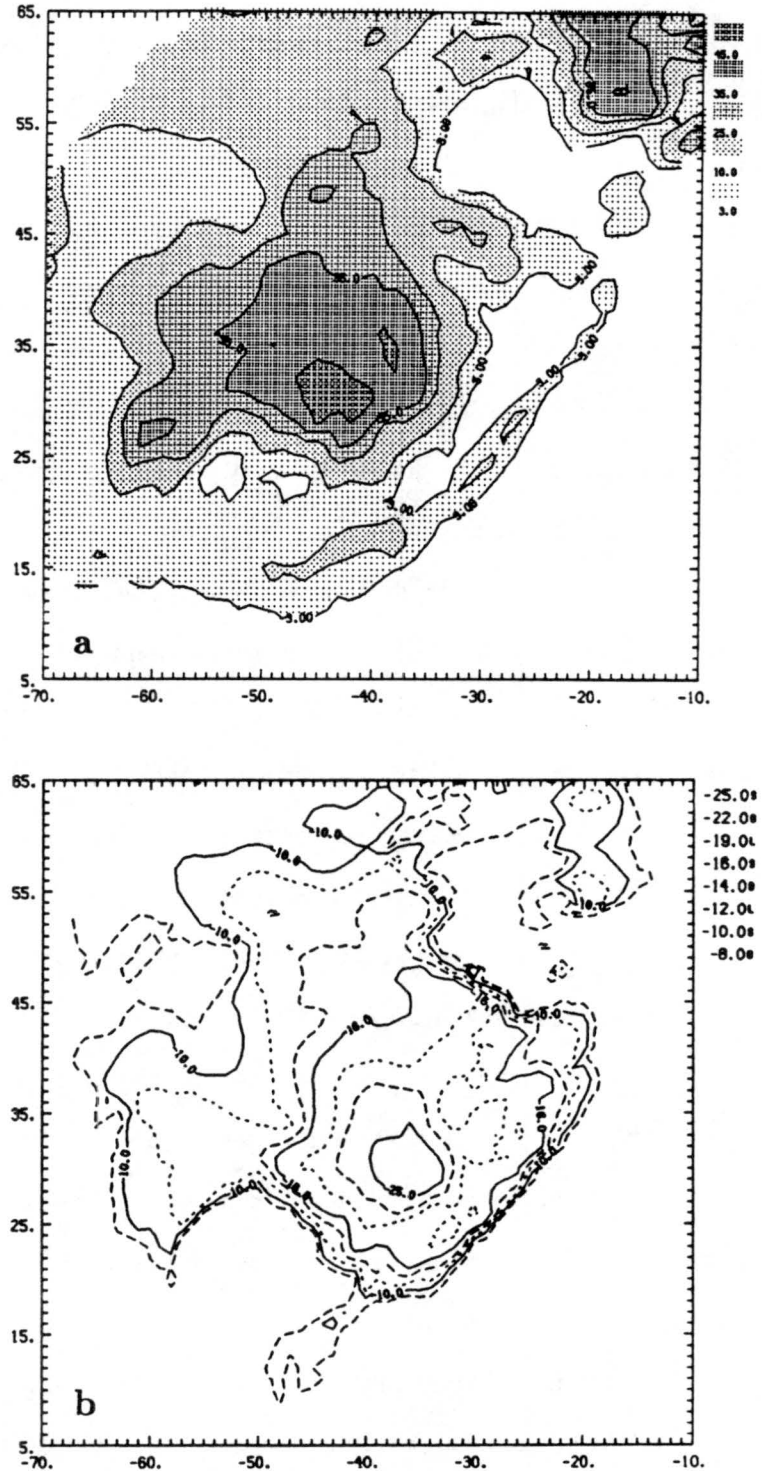


Figure 4.2: PPI scans at 17:45 for the gust front and storm system of 14 July, showing in (a) the reflectivity field and in (b) the radial velocity field observed by the NCAR CP-2 Doppler radar. The scan height is 0.4 km AGL and the radar is located at (0,0).

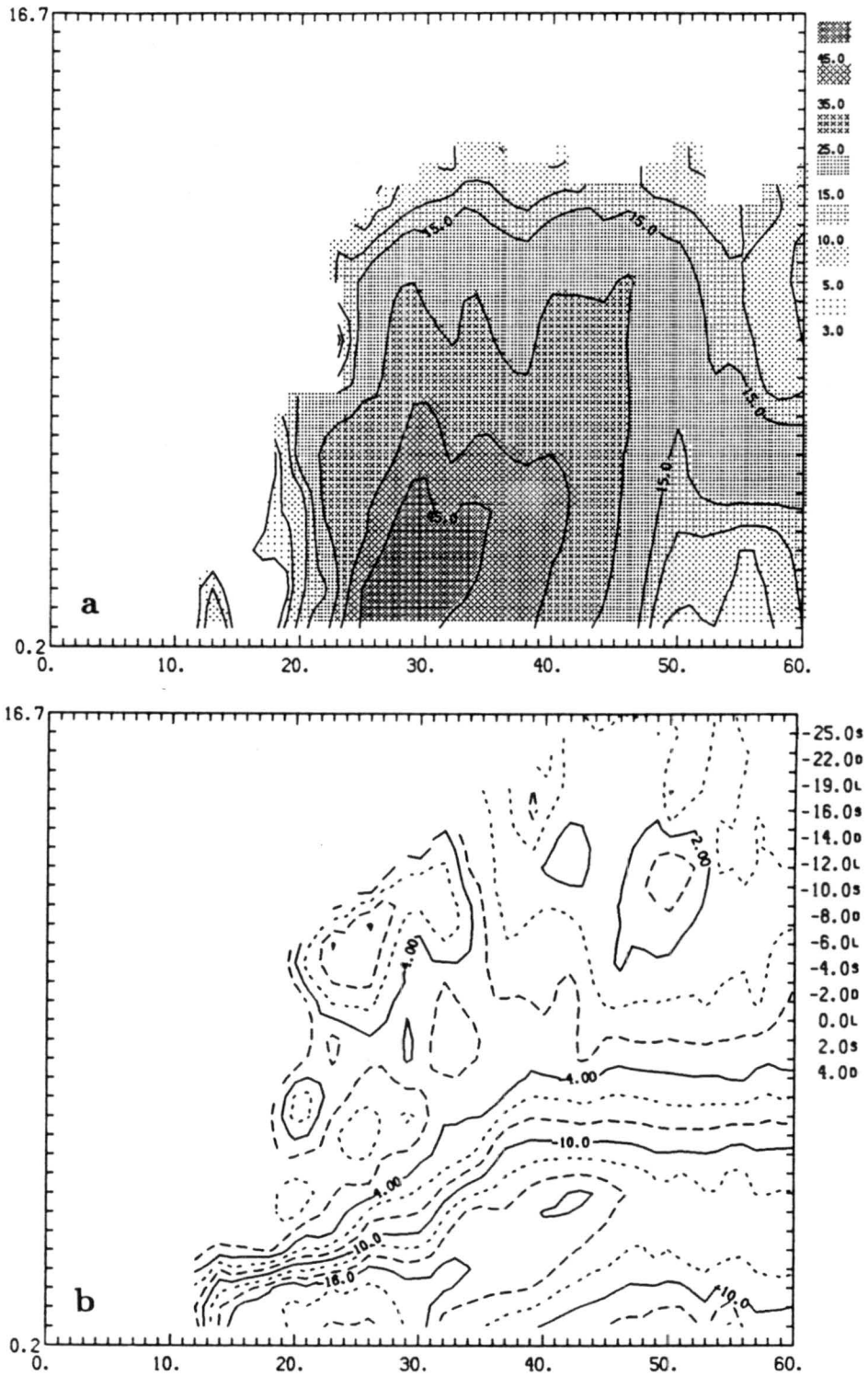


Figure 4.3: RHI scans at 17:45 through the outflow and downdraft of 14 July, showing in (a) the reflectivity field and in (b) the radial velocity field. Ground level is at 0.3 km MSL.

Table 4.2: Mass balance calculations of downdraft speeds from the outflow of 14 July. Outflow height is $h=2.0$ km. Error limits are for ΔV : ± 25 km³ and for A_{dd} : ± 5 km².

Time	Δt (min)	V_{out} (km ³)	ΔV (km ³)	A_{dd} (km ²)	\bar{A}_{dd} (km ²)	\bar{w} (ms ⁻¹)
173355		1427		146		
	3.2		179		146	6±2
173706		1606		145		
	3.5		171		136	6±2
174034		1777		128		
	2.0		154		144	9±3
174233		1931		160		
	3.4		248		160	8±2
174554		2179		161		
	3.2		215		137	8±2
174907		2394		113		
	6.3		324		111	8±2
175527		2718		109		
Avg						7±2

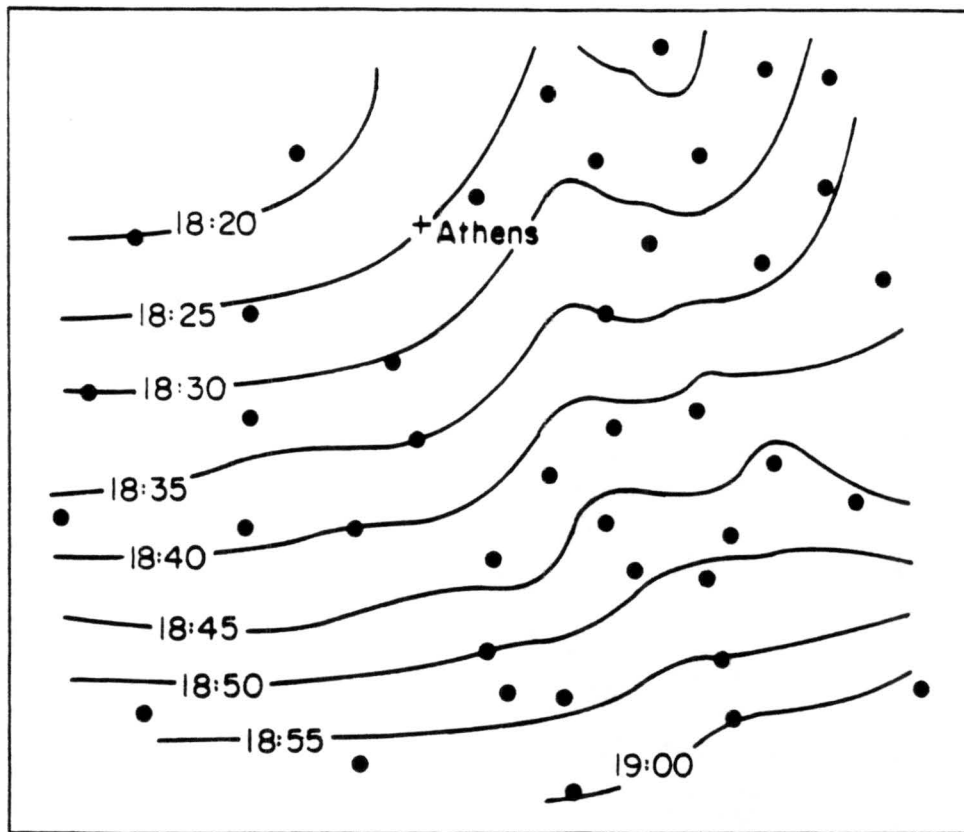


Figure 4.4: Isochrones of the leading edge of the gust front of 14 July.

for the observed pattern of outflow volume increase. By 17:55, the outflow volume rate of increase was just beginning to decline, as was downdraft areal coverage.

Surface Mesonetwork Analysis

By 18:20, the gust front had moved into the northwest portion of the NCAR PAM II surface network. The isochrone analysis of Figure 4.4 shows that the gust front traversed the network over a period of about 40 minutes. The propagation speed calculated from the isochrone analysis was 10 ms^{-1} , and this is significantly lower than the 17 ms^{-1} speed observed by the radar. This discrepancy can be explained by considering the stage of the lifecycle in which the gust front was at the times that the propagation speeds were figured. The radar observed speed was calculated while the downdraft behind the gust front was

very active, while the mesonetwork-observed speed was calculated some time after the downdraft had begun to collapse, and at this point, the winds behind the gust front had decreased considerably. This observation of differing gust front speeds at different lifecycle stages indicates a dependence of frontal speed on lifecycle stage, and this dependence is a manifestation of the airflow within the outflow, which evidently contributes significantly to the frontal speed. In fact, it will be shown in Section 4.4 that the density current approximation, which considers only the effect of the pressure gradient immediately behind the front, is inadequate in predicting the speed of this gust front, and of the fronts of the other cases included in this study. It turns out that with modification of the density current approximation, so that airflow behind the gust front is included, the resulting speeds for the cases show marked improvement over calculations with airflow in the outflow neglected.

Analysis of several fields associated with the gust front was carried out at 18:45, by which time the gust front had traversed the northern two-thirds of the network. The streamline and isotach analysis of Figure 4.5 shows that the the wind flowed nearly parallel to the direction of frontal motion behind the gust front, and that the gust front was a zone of increased wind speed gradient, with the fastest speeds just to the rear of the boundary, hence the name "gust front". That the wind flow was nearly parallel to the axis of frontal motion indicates that, provided a radial is oriented perpendicular to the gust front, the radar observed wind speeds behind the front and along this radial adequately estimates the actual wind speeds. This is important since in this study, comparisons will be made between radar and surface mesonetwork observed wind speeds.

It is noted from Figure 4.5 that the gust front speed exceeded the wind speeds observed behind the front. This appears to be true within the surface layer where the mesonetwork wind measurements are made, but above this layer, as indicated by the radar scan of Figure 4.6, the wind speeds were faster than frontal speed. Friction in the surface layer is responsible for the reduction of wind speed there, but a more interesting result of this discussion of wind speed behind the front is that, because the radar observed wind speeds are faster than frontal speed, there must be a piling up of mass just behind the frontal boundary, and just as the accumulation of mass below the downdraft causes the observed "thunderstorm high",

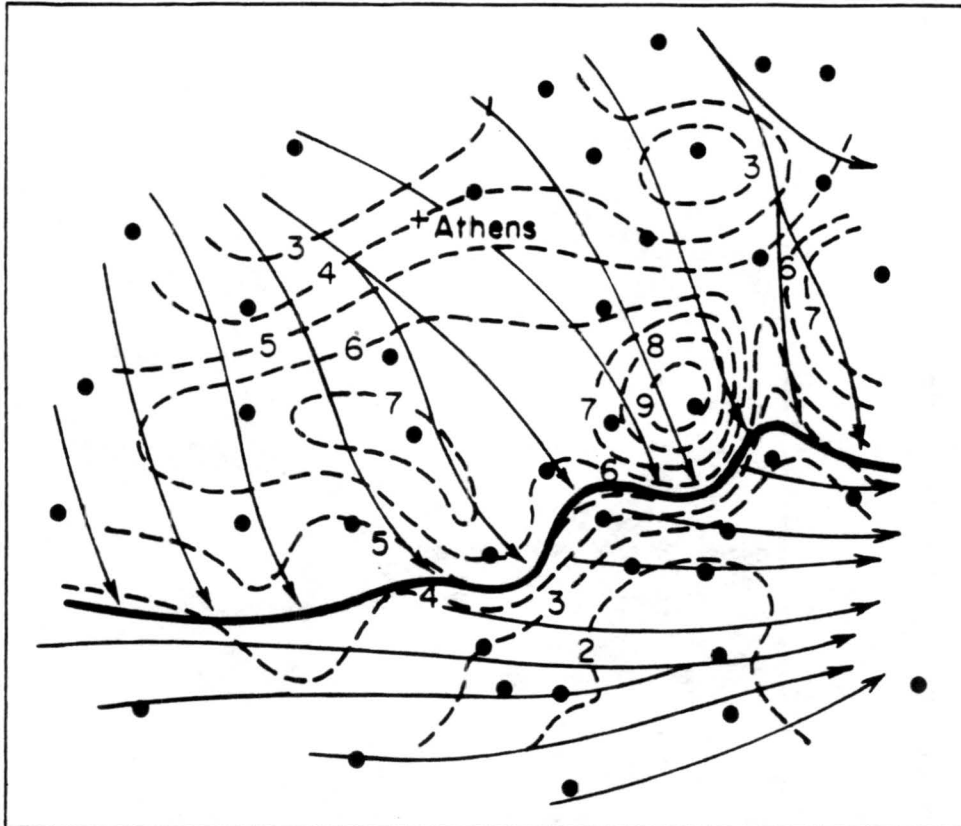


Figure 4.5: Streamline and isotach analysis at 18:45 on 14 July 1986. Streamlines are thin solid lines, isotachs are dashed lines in ms^{-1} , and the gust front is indicated by the thick solid line.

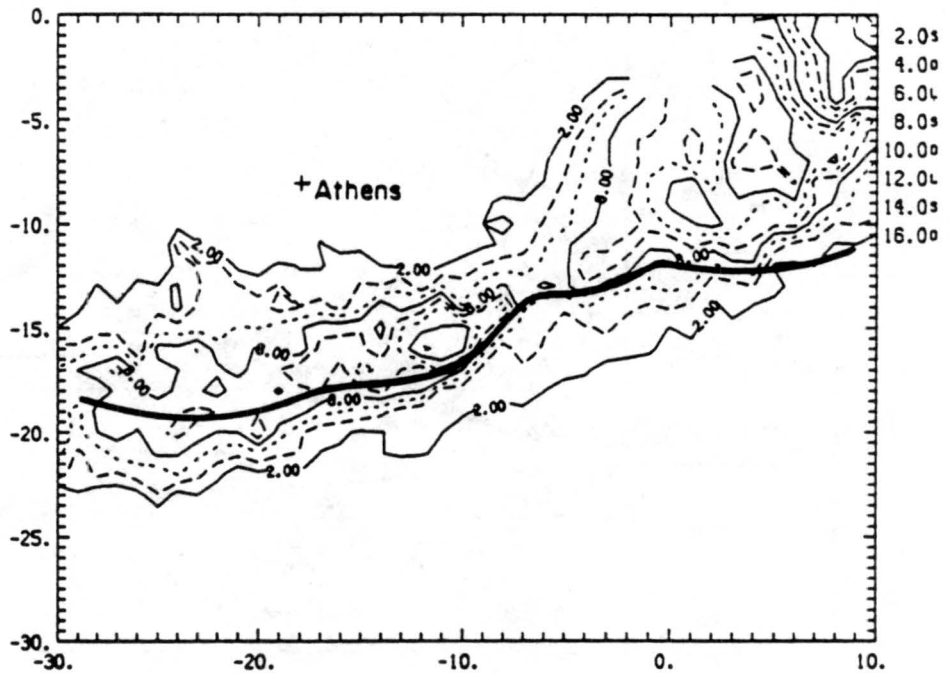


Figure 4.6: PPI scan at 18:42 showing observed radial velocities associated with the gust front of 14 July 1986. Scan height is 0.4 km AGL and the CP-2 Doppler radar is located at (0,0).

the accumulation of mass behind the gust front appears to be responsible for a pressure excess there which directly affects the speed at which the front moves.

Other features revealed by the isotach and streamline analysis are the wind flow ahead of the gust front and a “lobe and cleft” structure along the front in the eastern portion of the network. Out ahead of the front, the environmental flow was directed essentially parallel to the frontal motion, but near the frontal boundary, the environmental wind was observed to begin a shift into the direction of frontal motion, and this is in keeping with observations that a wind shift occurs prior to frontal passage. The “lobe and cleft” structure indicated by the isotach analysis is actually due to the intersection of two separate gust fronts. That there are two separate fronts is indicated by the radar scan of Figure 4.6, where it can be seen that there was a downdraft just behind the front in the eastern portion of the network. Since, however, only a small part of the second gust front is evident in the surface data, the two fronts are treated as a single gust front for the purpose of discussion of this case. The lobe and cleft structure observed in the isotach analysis is also evident in the other analyses.

The dry-bulb and dewpoint temperature analysis (fig. 4.7) indicate that the gust front was a discontinuity in both fields. The gradient of both fields were strongest at and just behind the gust front, with an air temperature drop of up to 9°C and a dewpoint drop of as much as 4–5°C between environmental and outflow air, indicating that the outflow was a pool of cooler, drier air relative to the environment. This analysis also indicates the observed lobe and cleft structure of the eastern portion of the gust front. The pressure field associated with this gust front is given in Figure 4.8. The outflow is seen to have been characterized by higher pressure, as compared to environmental values. The pressure field also shows that the gust front was defined as an increased gradient in surface pressure, making the pressure rise associated with the frontal passage evident.

Figure 4.9a shows the divergence field associated with the gust front. Convergence was evident along and just ahead of the front, with the largest values along the central and eastern portions of the front. Looking back to the isochrone analysis (fig. 4.4), it is evident that this was the fastest moving portion of the front, leading to the largest convergence in

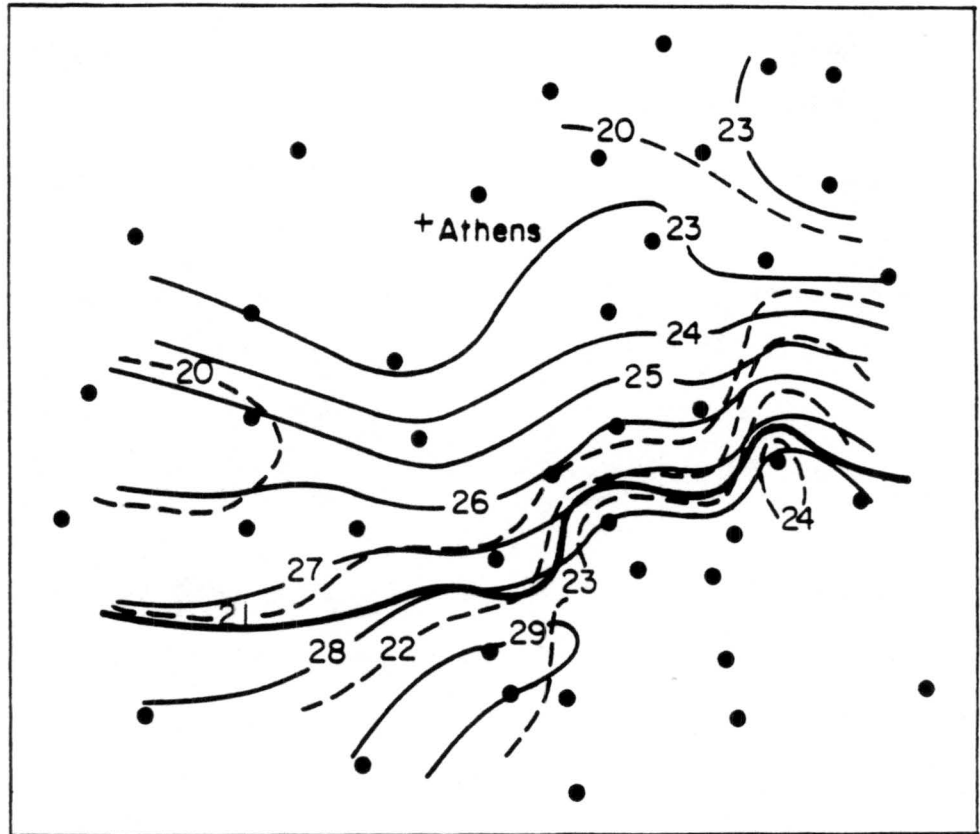


Figure 4.7: Dry-bulb and dewpoint temperature analysis associated with the gust front of 14 July 1986. Thin solid lines are isotherms in $^{\circ}\text{C}$, dashed lines are isodrosotherms in $^{\circ}\text{C}$, and the thick solid line is the gust front.

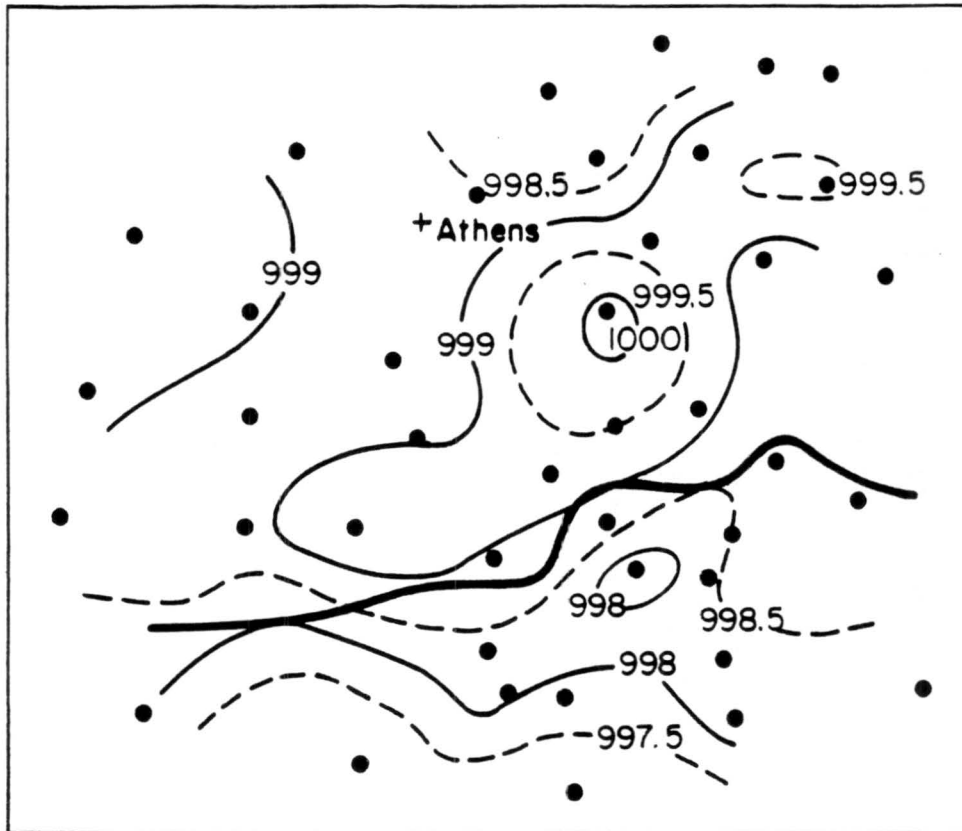


Figure 4.8: Surface pressure field associated with the gust front of 14 July 1986. Contours are in 0.5 mb increments, with solid lines representing whole values and dashed lines representing half-values. Pressures have been adjusted to the mean elevation of the network, which is 201 m MSL. The thick solid line is the gust front.

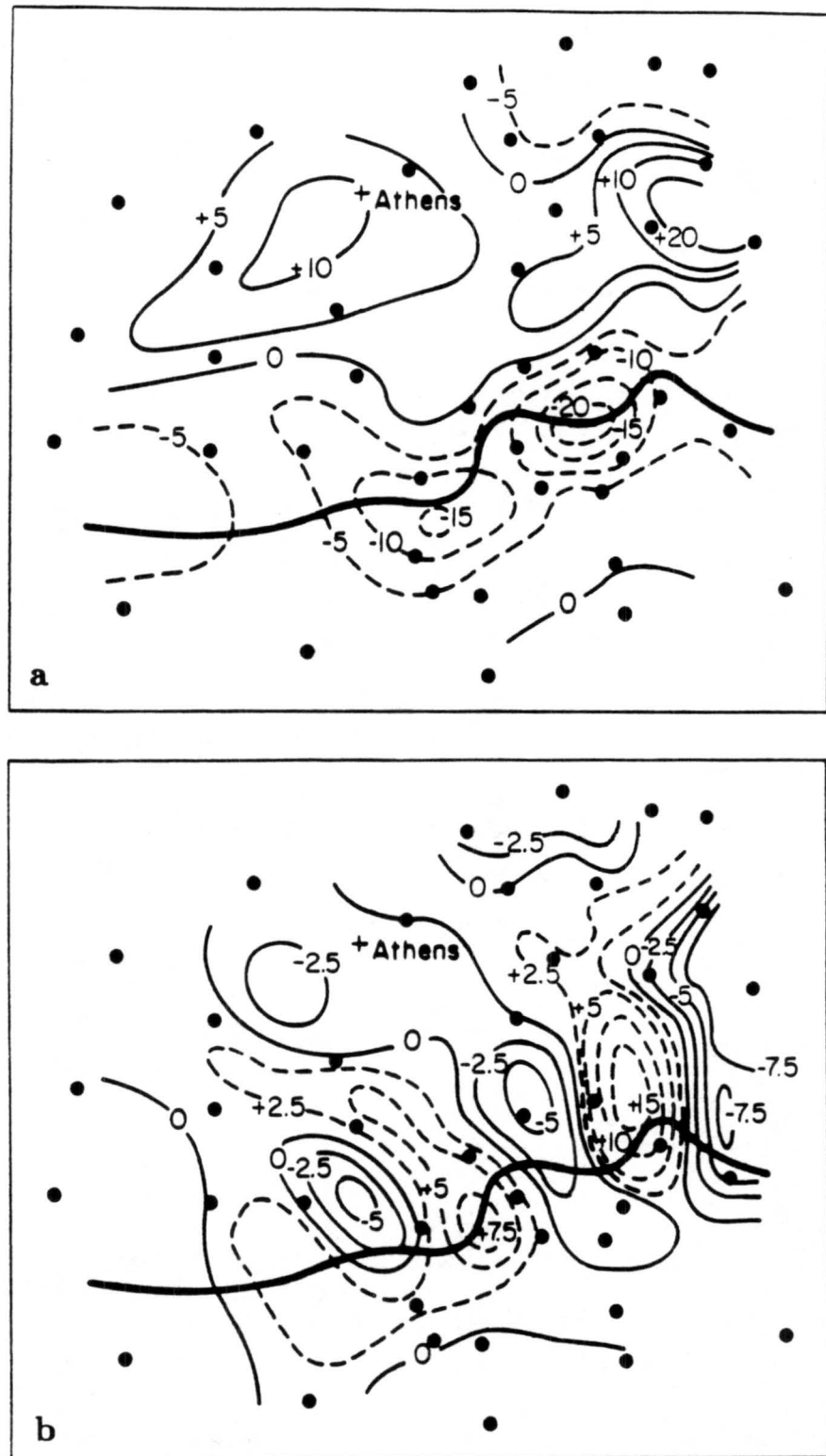


Figure 4.9: Divergence (a) and vorticity (b) fields associated with the gust front of 14 July 1986. In (a), solid lines indicate divergence and dashed lines indicate convergence ($s^{-1} \times 10^{-4}$), and in (b), solid lines indicate anticyclonic vorticity and dashed lines indicate cyclonic vorticity ($s^{-1} \times 10^{-4}$).

this region. This convergence has been observed to be in association with the development of arc cloud lines above gust fronts, and even the initiation of new convection. In the outflow, the air was characterized by divergence, with two separate pronounced regions. The weaker region is due to the dying downdraft behind the gust front, and the stronger region is due to the active downdraft located to the rear of the second gust front. The rest of the outflow was characterized by neither strong convergence or divergence. Figure 4.9b illustrates the vorticity field associated with the gust front. Most of the outflow was characterized by a nearly non-rotational flow. However, areas of vorticity are observed along and to the rear of the gust front, with large cyclonic vorticity associated with the lobe. It is in these regions of rotational flow that vortices have been observed to occur in association with gust fronts, and the analysis indicates that gust front intersections are one way of generating these areas of rotation. Anticyclonic rotation is evident on the extreme eastern edge of the network, and this was associated with a downdraft in that location (see divergence field of fig. 4.9a). Another area of weak anticyclonic rotation was located to the rear of the central portion of the gust front, again in association with the dying downdraft at that location.

4.1.2 25 July 1986

Radar Analysis

Intense convection broke out to the southeast of the surface mesonet network during the mid-afternoon hours of 25 July. A gust front and outflow were initiated by this convection, and as the gust front moved to the northwest, cells began to form along its leading edge. Several of these cells developed individually and then merged into a large area of convection, which then maintained the gust front that was responsible for its formation. It is after this large area of convection forms and begins to maintain the gust front and outflow responsible for its formation that it becomes of interest to this case.

On 25 July, the FLOWS FL-2 Doppler radar observed intense convection to the southeast of the radar site, with reflectivities of over 65 dBZ and storm tops to over 10 km AGL. This area of convection was moving slowly to the northwest, and it had an associated gust front and outflow. Just prior to 15:00 CDT, this gust front became observable in the lowest

elevation (0.4°) PPI scan. The gust front, located over 50 km to the southeast of FL-2, was moving to the northwest. The initiation of this gust front was not visible to the radar because of distance from the radar and curvature of the earth.

The first cells began to develop along the leading edge of this outflow just after 15:00. The convection quickly intensified, with reflectivity values exceeding 65 dBZ and storm tops reaching to over 10 km AGL. At this time, two distinct cells had formed, and they developed downdrafts in less than 15 minutes and began to push the gust front. Within another 15 minutes, two more cells formed, developed downdrafts, and then all of the cells merged into a large area of convection. This system extended lengthwise for over 50 km, and the outflow that it was pushing was unidirectional in nature. While the convection remained nearly stationary, the radar observed a gust front motion of 8 ms^{-1} to the northwest. Eventually, the gust front would move to over 20 km ahead of the downdrafts.

Figure 4.10 shows the convection, gust front, and outflow as they appeared in the radar PPI scans at 15:47. The separate downdrafts are distinguishable within the convective system, which extends lengthwise for over 50 km, as cores of highest reflectivities. The edges of the downdrafts were found to be associated with the 35 dBZ contour. The radial velocity field also illustrates the locations of the downdrafts as the cores of strongest wind speeds. The gust front appeared in the radar scans as a band of up to 15 dBZ reflectivity (fig. 4.10a), and the unidirectional nature of the outflow is clearly visible. The outflow air was associated with reflectivities below about 8 dBZ. Figure 4.10b also indicates the location of the gust front, as it appeared as a gradient in the radial velocity field. Wind speeds observed by the radar in the outflow were about 10 ms^{-1} , though they appear to be less in Fig. 4.10b. This is because the velocities were smoothed for plotting purposes, and they appear somewhat less than actual. Air speeds at the bases of the downdraft ranged from $10\text{--}12 \text{ ms}^{-1}$ and were as high as 15 ms^{-1} , all in a ground-relative frame.

An RHI scan through the outflow and storm system is given in Figure 4.11. The gust front was about 15 km ahead of the downdraft, which appeared as a core of high reflectivity. The radial velocity field (fig. 4.11b) indicates the low-level outflow below the inflow into the storm updraft. The outflow top and leading edge appeared as gradients in the radial

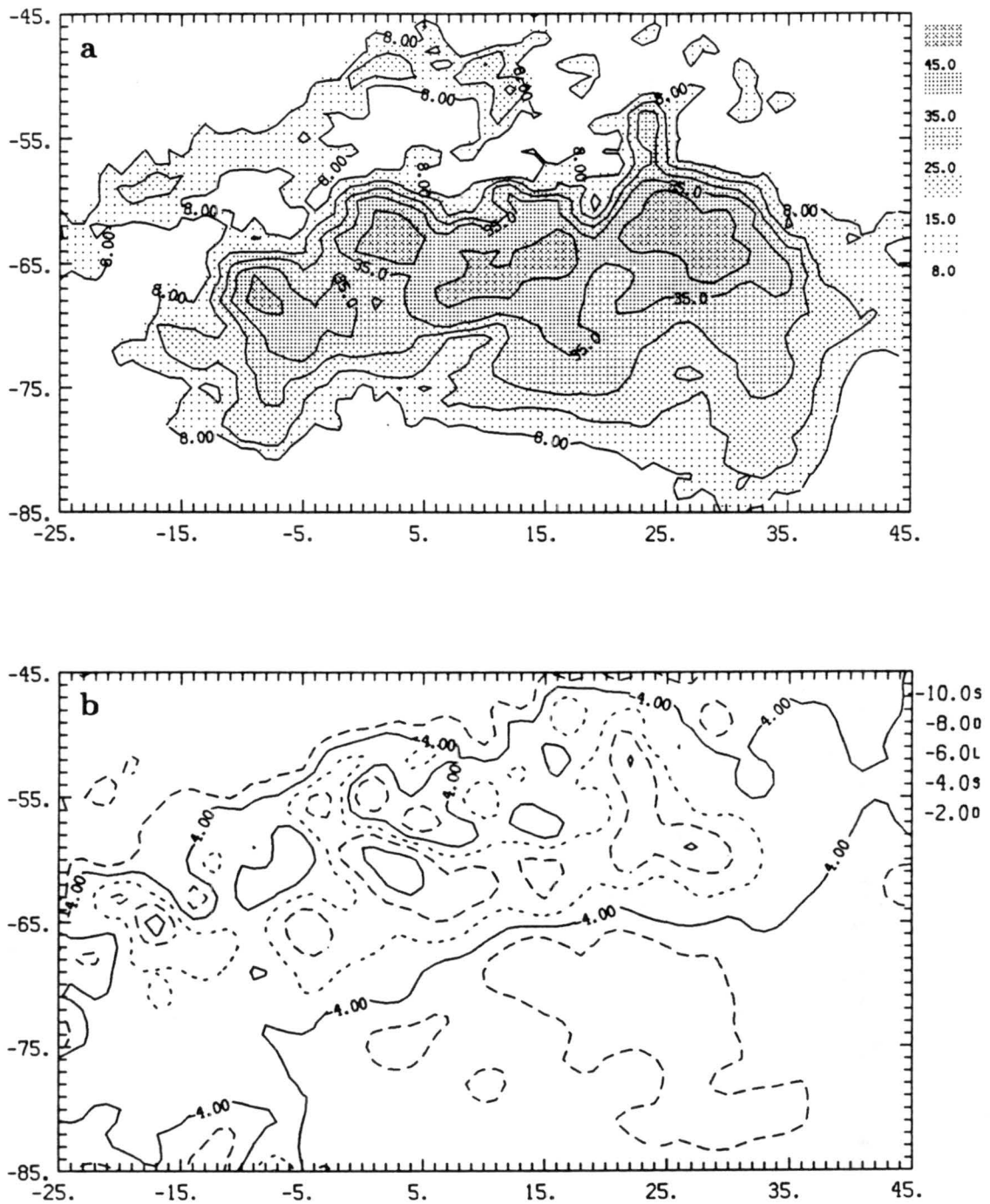


Figure 4.10: PPI scans at 15:47 for the outflow and convective system of 25 July, showing in (a) the reflectivity field and in (b) the radial velocity field observed by the FLOWS FL-2 Doppler radar. The scan height is 0.4 km AGL and the radar is located at (2.4, -21.7).

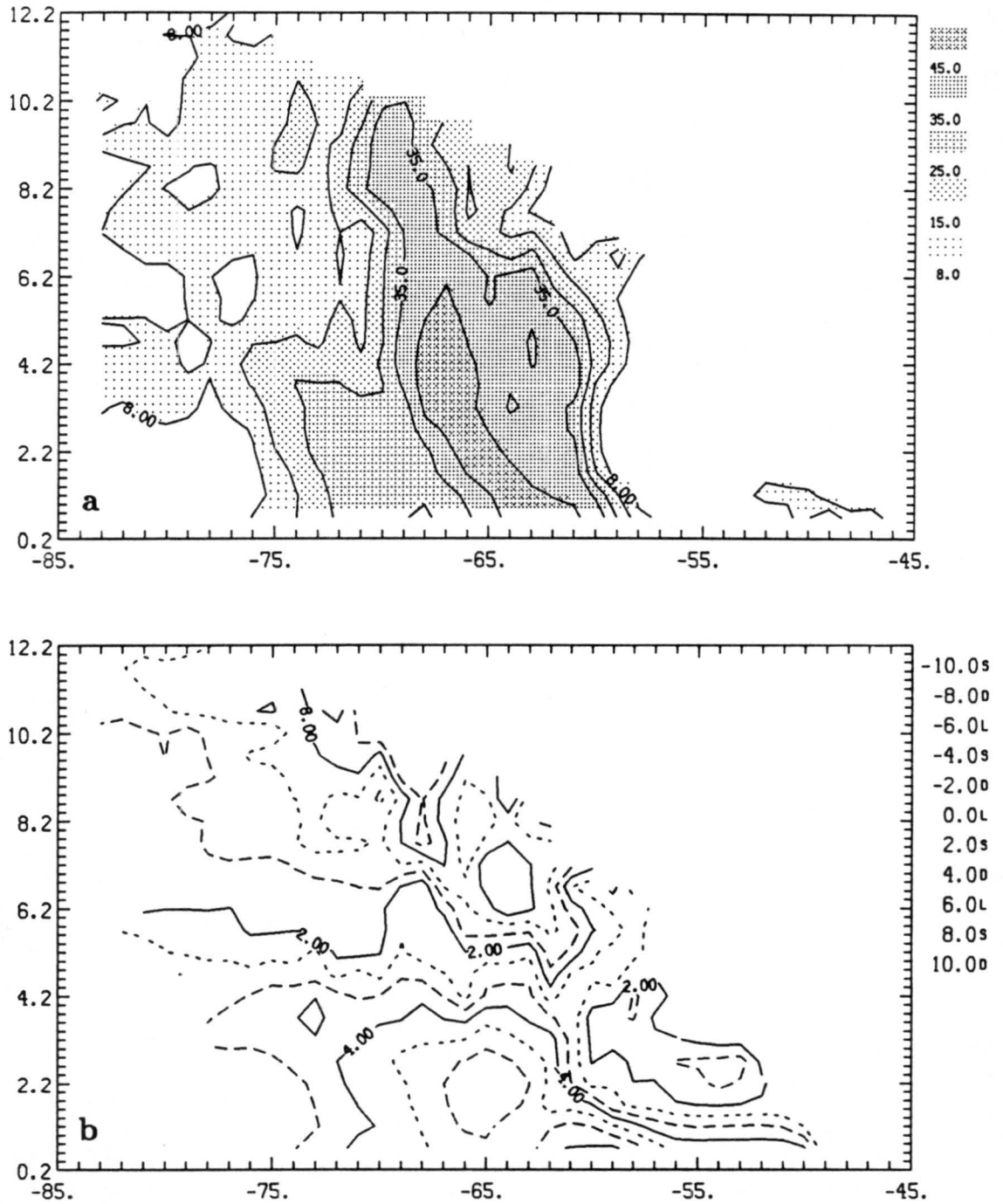


Figure 4.11: RHI scans at 15:47 through the outflow and convective system of 25 July, showing in (a) the reflectivity field and in (b) the radial velocity field. Ground level is 0.2 km MSL.

velocities observed by the radar, with smoothed outflow speeds of up to 6 ms^{-1} and speeds at the downdraft base approaching 9 ms^{-1} . The RHI scan through the storm indicates that there was no rear inflow present into the back of the downdraft in this case.

The downdraft air speeds calculated from mass balance for the four downdrafts are given in Table 4.3. The downdraft speeds given are averages for all of the downdrafts present

Table 4.3: Mass balance calculations of downdraft speeds from the outflow of 25 July. Outflow height is $h=1.1 \text{ km}$. Error limits are for ΔV : $\pm 50 \text{ km}^3$ and for A_{dd} : $\pm 5 \text{ km}^2$.

Time	Δt (min)	V_{out} (km^3)	ΔV (km^3)	A_{dd} (km^2)	\bar{A}_{dd} (km^2)	\bar{w} (ms^{-1})
153416		2538		125		
	9.1		420		146	5 ± 1
154232		2958		168		
	9.1		454		221	4 ± 1
155231		3412		274		
	9.1		513		206	5 ± 1
160138		3925		137		
Avg						5

during each time interval, since it is not possible to determine how much of the outflow increase was due to each separate downdraft. Over a total time period of more than 27 minutes, an average value of 5 ms^{-1} , good to $\pm 1 \text{ ms}^{-1}$, was calculated for the downdrafts of this case. During each of the three time intervals in the table, however, not all of the four downdrafts were always present. From Table 4.3, it is obvious that the outflow was quite large, owing to its unidirectional nature. The greatest outflow volume increases coincide with the greatest downdraft areal coverage, and over a period of more than 27 minutes, the discrete downdraft speeds remained constant. Thus, the greatest mass flux out of the downdraft occurred when downdraft areal coverage was greatest, and hence, the correlation between greatest outflow volume increase and greatest downdraft cross-sectional area.

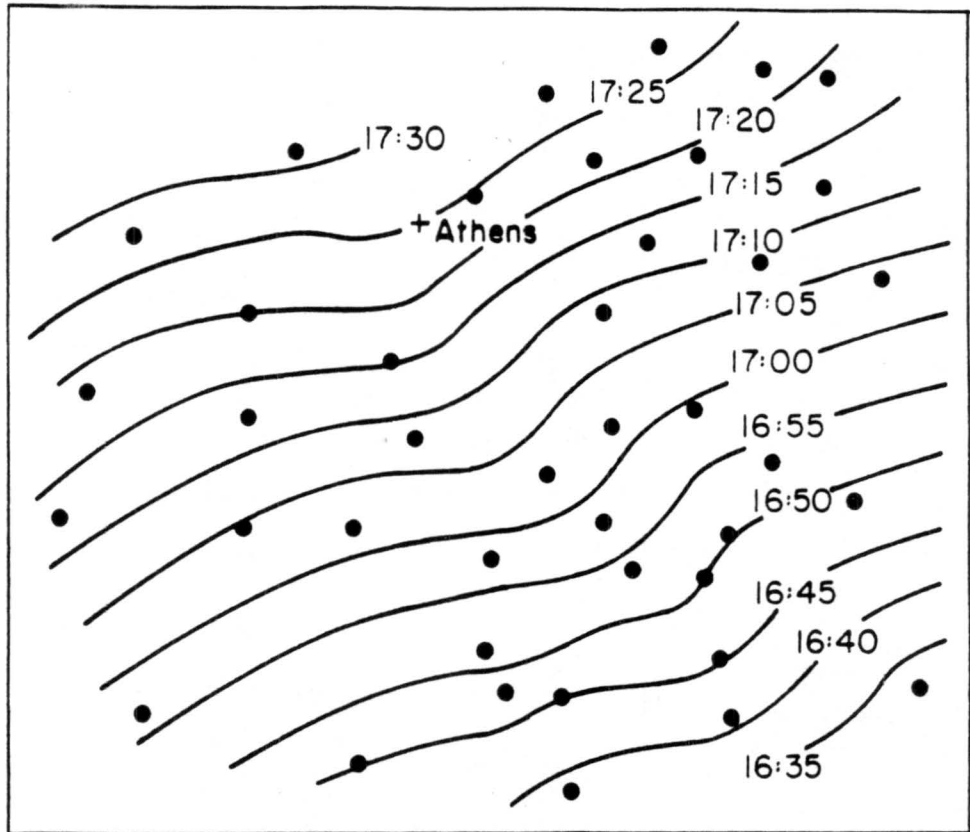


Figure 4.12: Isochrones of the leading edge of the gust front of 25 July.

Surface Mesonetwork Analysis

By 16:35, the gust front was beginning to enter the southeast portion of the surface network. The isochrone analysis of Figure 4.12 shows that the gust front took nearly an hour in traversing the network, exiting on the northwest side. From the isochrone analysis, a gust front propagation speed of 8 ms^{-1} was calculated, and this is in agreement with the speed observed by the radar. This is a reasonable result since the gust front had not progressed to a different stage in its lifecycle between the time of the radar analyses and the isochrone analysis of Figure 4.12. It was noted in the section on radar analysis that the gust front had initiated these new downdrafts, and they in turn became responsible for continuing to push the gust front along, since the downdrafts which originally initiated the gust front had begun to collapse. Thus, the cold source behind the gust front continued to

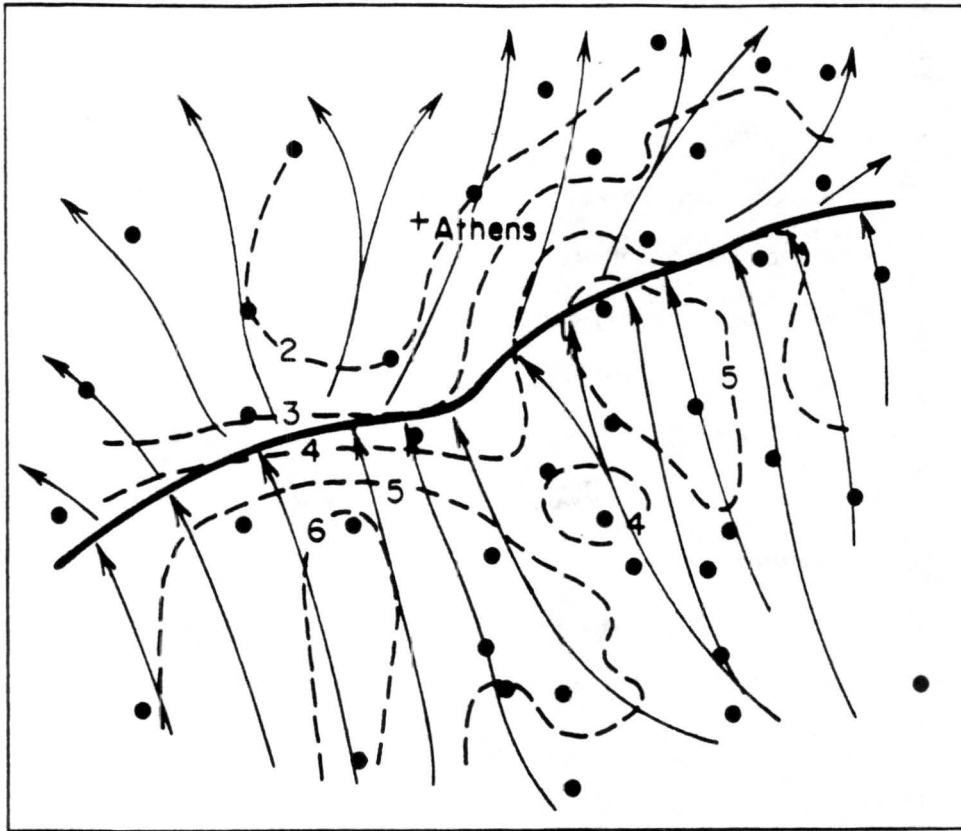


Figure 4.13: Streamline and isotach analysis at 17:10 on 25 July 1986. Streamlines are solid lines, isotachs are dashed lines in ms^{-1} , and the gust front is indicated by the thick solid line.

remain active, and hence, the agreement between radar observed and isochrone calculated propagation speeds. This gust front is rather interesting because it turns out that the gust front essentially maintained itself. As it moved along, it continued to initiate new convection, which in turn contributed to the outflow, and this self-perpetuation continued for several hours.

Surface analysis for the gust front was carried out at 17:10, by which time the gust front had reached the central portion of the network. The streamline and isotach analysis for this case are given in Figure 4.13. As in the previous case, wind flow behind the gust front was oriented essentially perpendicular to the front itself. Again, there was an increased gradient in the surface wind speed all along the gust front, with speeds weakening to the rear. The

weak gradient in wind speed for this case is indicative of the weakness of the gust front. This gust front was, in fact, the weakest of the three MIST cases, and the other analyses also support this. Ahead of the gust front, the environmental flow was moving in nearly the same direction as the gust front, and it might be expected that this scenario would cause enhancement of the gust front speed, just as opposing flow might be expected to hinder gust front forward progress somewhat. For this reason, Seitter (1983) has proposed a modification to the density current approximation which accounts for the environmental flow through which the gust front is moving, and this is discussed in detail in Section 4.4. One other feature revealed by the isotach analysis is some evidence of a cleft in the front in the central portion of the network. This cleft is also observed in some, but not all, of the other analyses for this case.

The gust front appears as a weak temperature drop in the dry-bulb temperature analysis (fig. 4.14). The temperature drop was on the order of about 3°C with the passage of the front, and this is the smallest temperature change associated with the MIST gust fronts. The dewpoint analysis (fig. 4.14) shows an inconsistent dewpoint temperature field associated with the gust front in the way that depending upon location, there was either a slight rise or a slight fall in dewpoint with frontal passage. Further behind the gust front, the analysis shows some indication of the outflow being slightly drier than the environment through which it is moving. The cleft in the front suggested by the isotach analysis is not evident in the dry-bulb and dewpoint analyses. The pressure field (fig. 4.15), however, does suggest this cleft. The pressure rise associated with the frontal passage is also illustrated, with generally higher pressure in the outflow, though these higher pressure areas occurred in "pockets". It appears that the inconsistencies in the dewpoint and pressure fields behind the front exist because of the locations of downdrafts to the rear of the gust front.

Figure 4.16a shows the divergence field associated with the gust front. In general, convergence existed along the entire length of the front, with the largest values occurring along or just to the rear of the front. Since the wind direction changed little across the front, most of the observed convergence was due to speed convergence. The region of pronounced divergence just to the rear of the central portion of the gust front is due to a downdraft

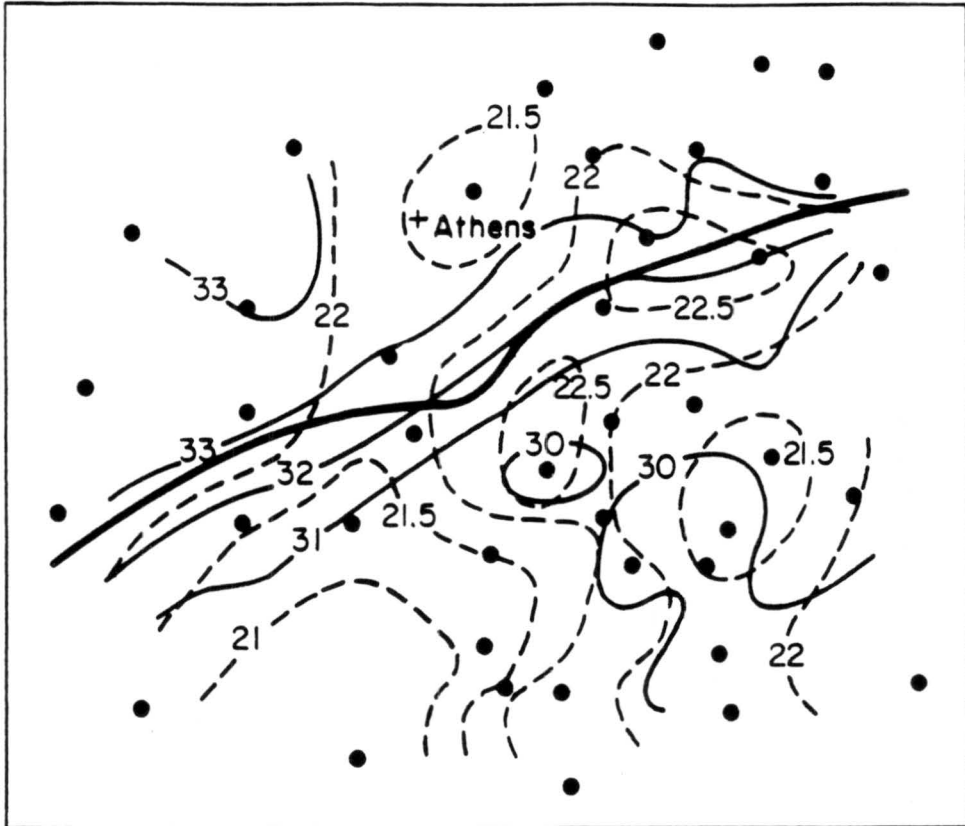


Figure 4.14: Dry-bulb and dewpoint temperature analysis associated with the gust front of 25 July 1986. Solid lines are isotherms in $^{\circ}\text{C}$, dashed lines are isodrosotherms in $^{\circ}\text{C}$, and the thick solid line is the gust front.

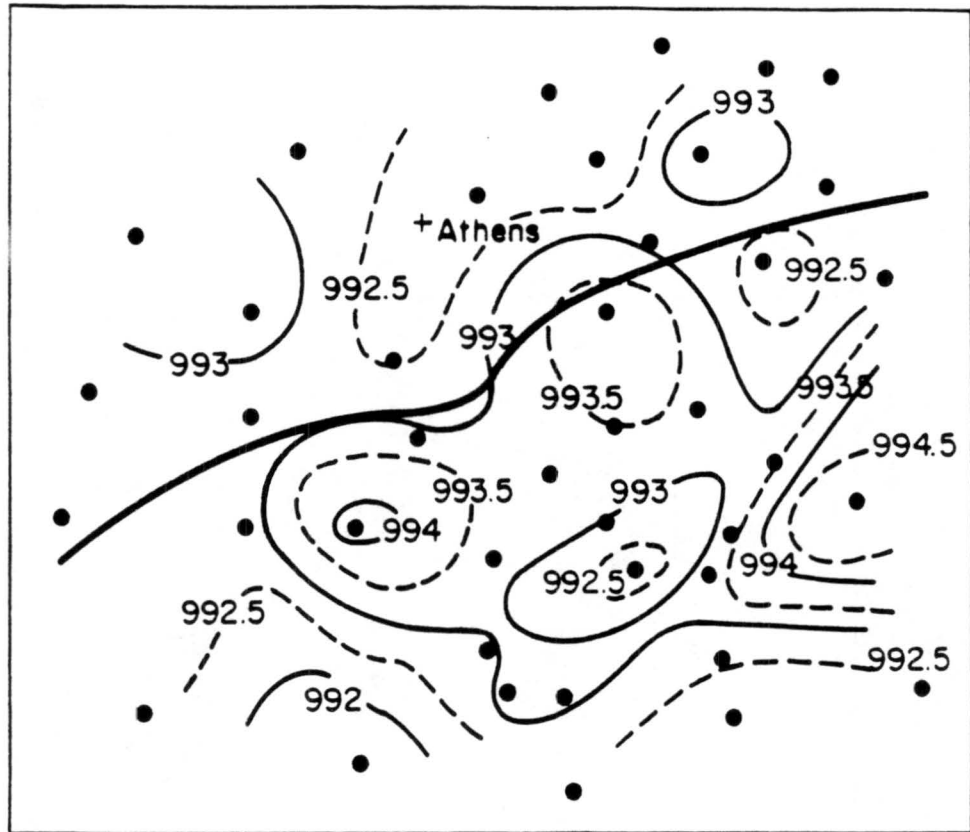


Figure 4.15: Surface pressure field associated with the gust front on 25 July 1986. Contours are in 0.5 mb increments, with solid lines representing whole values and dashed lines representing half-values. Pressures have been adjusted to the mean elevation of the network, which is 201 m MSL.

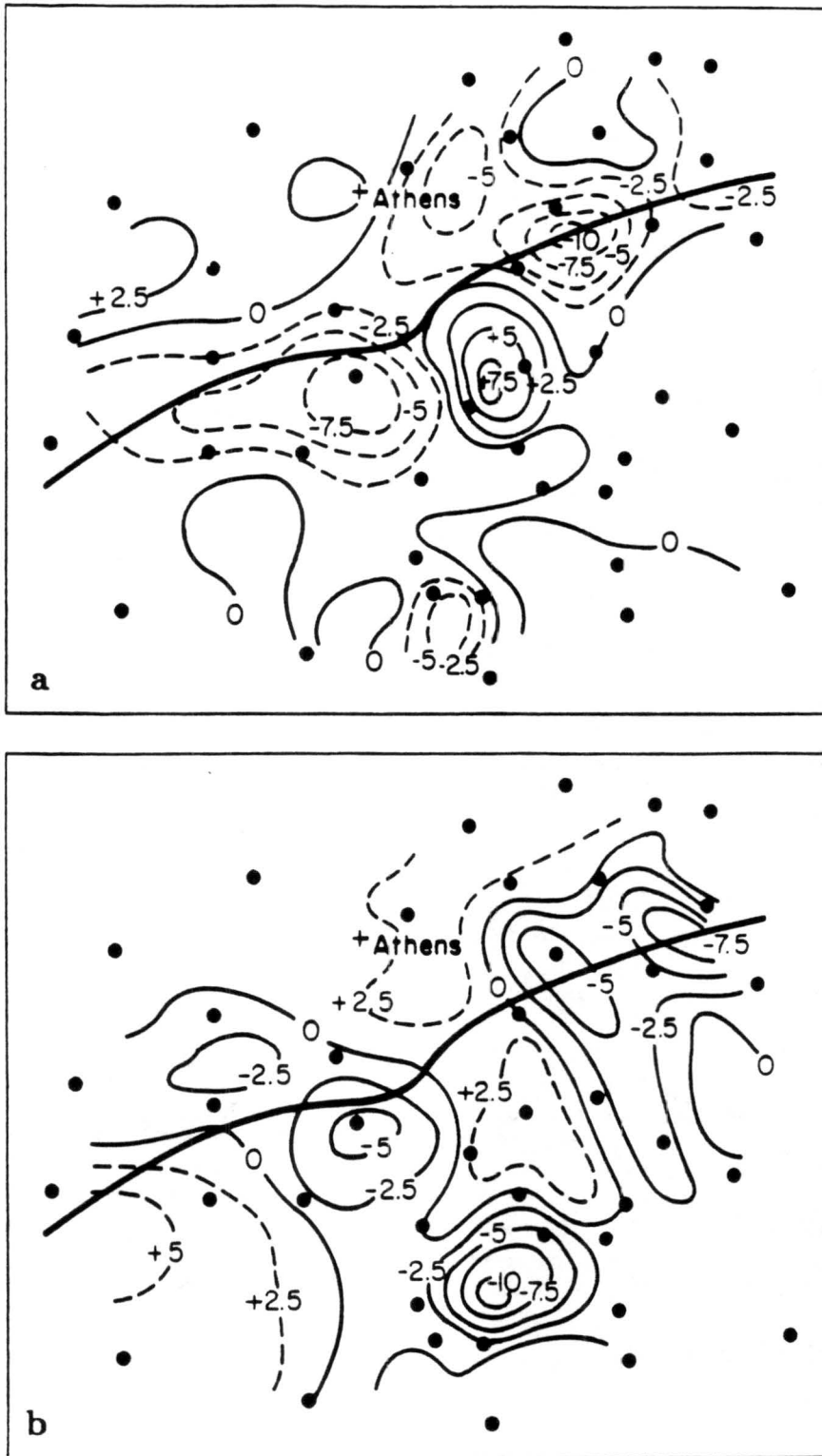


Figure 4.16: Divergence (a) and vorticity (b) fields associated with the gust front of 25 July 1986. In (a), solid lines indicate divergence and dashed lines indicate convergence ($s^{-1} \times 10^{-4}$), and in (b), solid lines indicate anticyclonic vorticity and dashed lines indicate cyclonic vorticity ($s^{-1} \times 10^{-4}$).

at that location. Another downdraft is evident further to the rear of the gust front, with the remainder of the outflow having no major areas of convergence or divergence. The vorticity analysis of Figure 4.16b indicates areas of rotation along the gust front, but the most pronounced areas were associated with downdrafts located behind the gust front, and they were exhibiting anticyclonic rotation, as in the previous case.

4.1.3 31 July 1986

Radar Analysis

Doppler radar data from this day show that a gust front was initiated in the late morning hours by an area of convection well to the north-northwest of the surface mesonet network. This gust front moved slowly southward, and by very early afternoon, it initiated new convection. The new convection developed quickly as separate cells, but later merged into a more organized convective system, which initiated a new gust front and outflow. It is this convective system and its associated outflow that are of interest to this study.

The FLOWS FL-2 Doppler radar observed a gust front to move into observation range in the late morning hours of 31 July. The gust front had been initiated earlier by convection well to the north-northwest of the radar, and it began to move slowly southward. The initiation of this gust front was not observable by the radar, even in the lowest elevation (0.4°) PPI scan, due to distance from the radar and curvature of the earth.

At 12:40 CDT, the first cell developed along the leading edge of the old outflow. Figure 4.17 illustrates both the pre-storm and post-storm environmental soundings for this date. Stability indices calculated from the pre-storm sounding indicated the strong likelihood of thunderstorm activity, with possible severe weather. Also, the pre-storm sounding indicates an LCL of about 850 mb, while the post-storm sounding indicates an old outflow depth up to 900 mb. Allowing for the nearly two-hour difference between the time that the gust front initiated new convection and the time of the sounding, where some outflow depth decrease likely occurred, it appears that the old outflow was deep enough to raise surface environmental air upwards to the LCL, and in this way, initiate new convection along its leading edge.

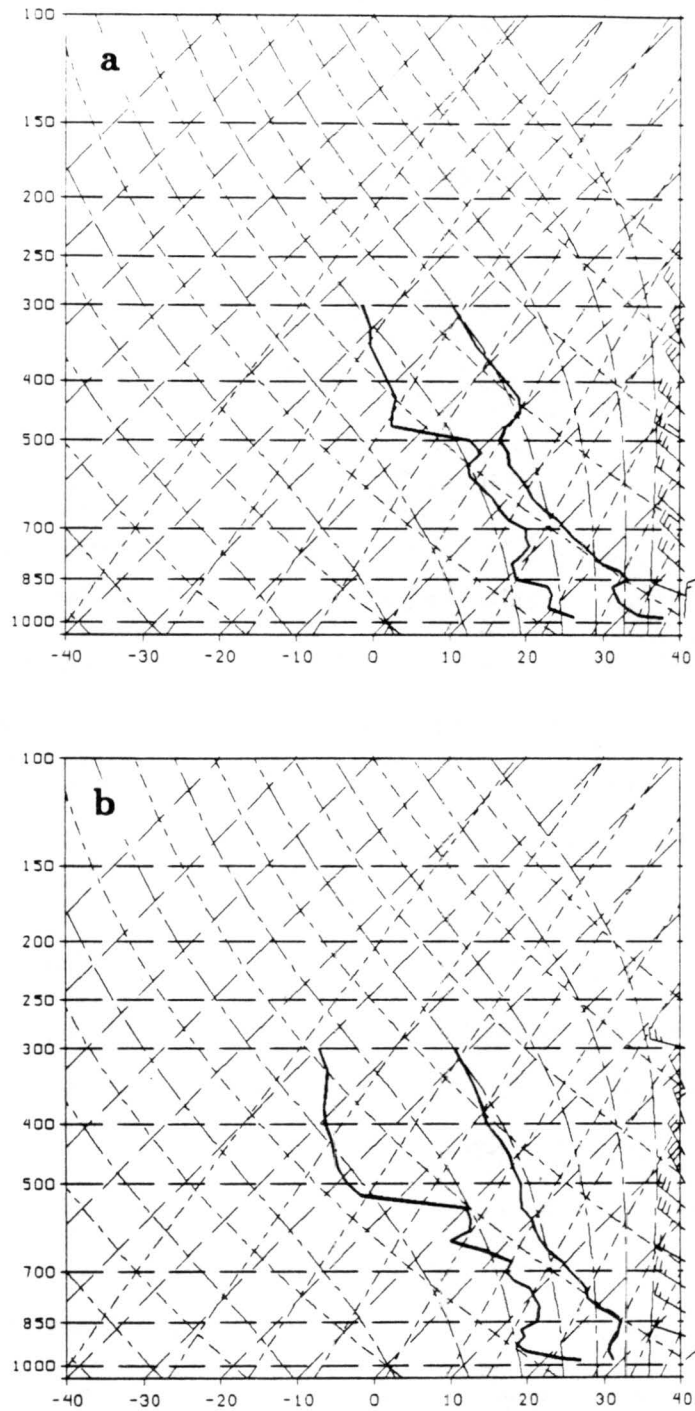


Figure 4.17: Soundings for 31 July in both the pre-storm and post-storm soundings. The soundings are taken at Hazel Green, AL, which is located about 25 km north-northeast of FL-2. The depth of the old outflow is indicated in the post-storm sounding as a layer of cooler, drier air at the surface.

This first cell developed at about 50 km to the northwest of the radar and began moving east-southeastward at about 7 ms^{-1} . This cell quickly formed a downdraft and subsequently initiated a new gust front and outflow. The new gust front was first observable by the radar just prior to 13:00, appearing as a thin band of weak reflectivities, with maximum values approaching 5 dBZ. The cell itself had become intense, with reflectivities of over 65 dBZ and a storm top to over 10 km AGL.

Just as the first cell was initiating the new gust front, a second cell was forming along the leading edge of the old outflow to the west-northwest of the first cell. This second storm began to move east-southeastward also at about 7 ms^{-1} , and it too became intense, with reflectivities to over 65 dBZ and a top to over 10 km. As this cell quickly developed and enlarged, it developed a downdraft, and both of the cells began to merge into a more organized convective system, which was responsible for maintaining the new gust front and outflow. The radar observed a gust front motion of 11 ms^{-1} to the south.

Eventually, a third cell formed along the leading edge of the outflow, to the west-northwest of the older activity. In time, this cell would also merge with the convective system, which would then extend lengthwise for over 50 km. The outflow would then be characterized by a unidirectional configuration. Figure 4.18 shows PPI scans of the convective activity and its associated outflow at 13:35. The separate downdrafts were distinguishable in the reflectivity and radial velocity fields as cores of highest values. The third cell can be seen to be forming to the west-northwest of the older convective activity. The outflow, which was unidirectional in nature, appeared as a band of up to 15 dBZ reflectivity, as well as a gradient in the radial velocities observed by the radar. The air in the outflow was associated with reflectivity values below 8 dBZ. Wind speeds in the outflow were observed by the radar to be in the range of $11\text{--}14 \text{ ms}^{-1}$ while at the bases of the downdrafts, speeds approached 16 ms^{-1} , all in a ground-relative frame.

An RHI scan (fig. 4.19) through the outflow and storm show that the downdraft was associated with the 35 dBZ contour, and extended to over 5 km AGL. The outflow top and leading edge appeared in the radial velocity field as a gradient in the velocities, giving a mean depth for the outflow of 1.2 km. Another interesting feature illustrated in the RHI

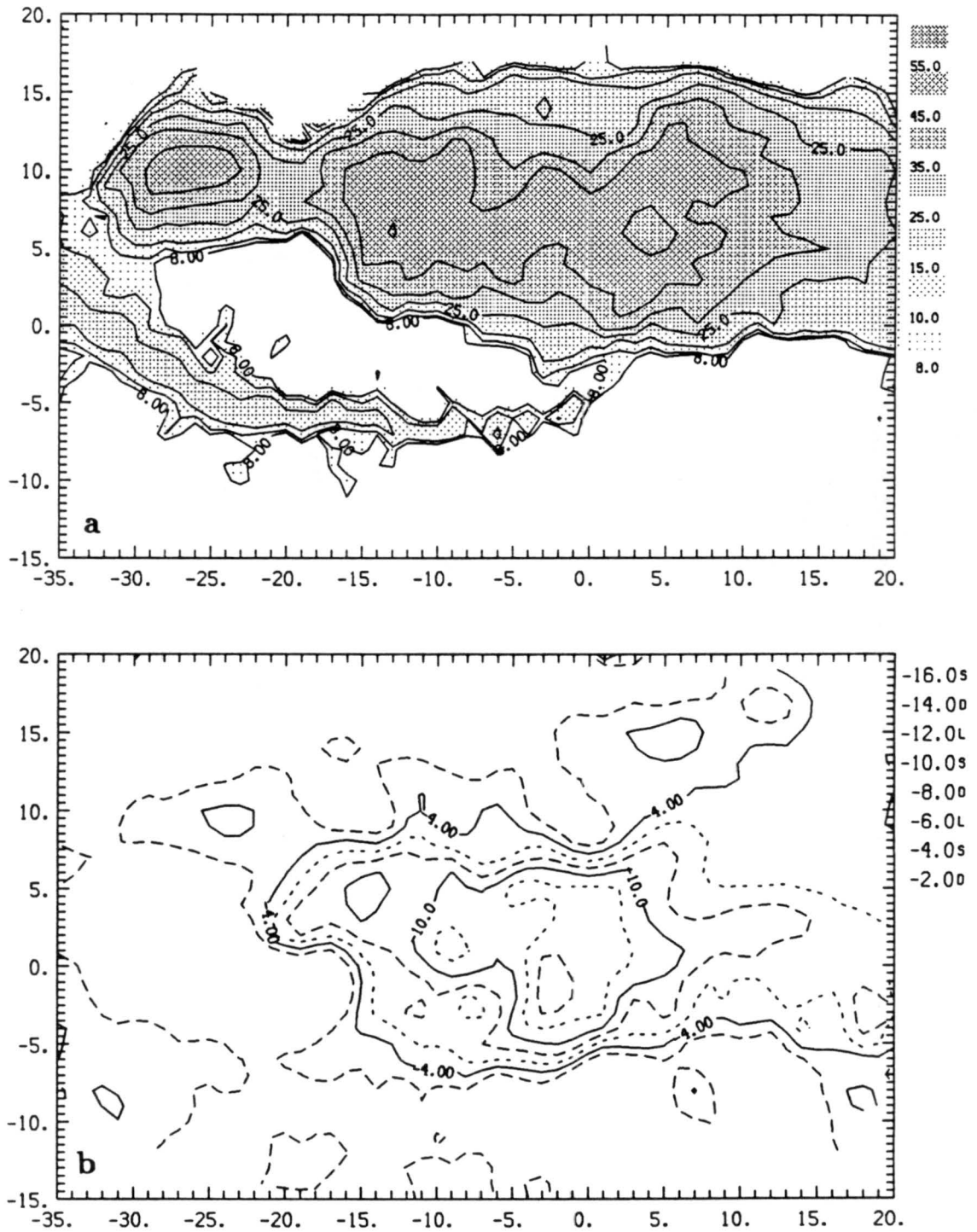


Figure 4.18: PPI scans for the outflow and storm system of 31 July, showing in (a) the reflectivity field and in (b) the radial velocity field. The scan height is 0.4 km AGL and the FLOWS FL-2 radar is located at (2.4,-21.7).

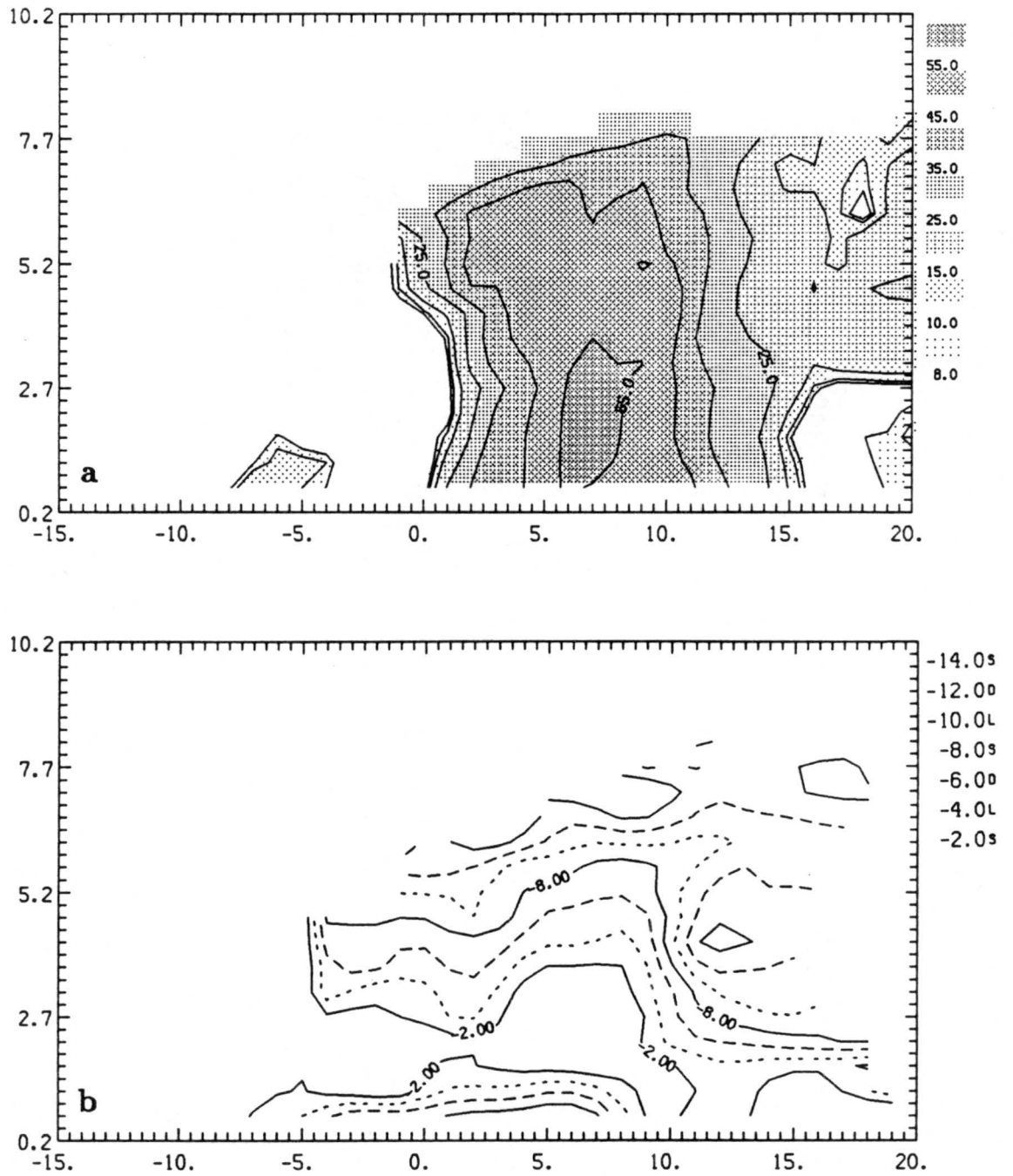


Figure 4.19: RHI scan at 13:35 through the outflow and storm system of 31 July, showing in (a) the reflectivity field and in (b) the radial velocity field. Ground level is at 0.3 km.

Table 4.4: Mass balance calculations of downdraft speeds from the outflow of 31 July. Outflow height is $h=1.2$ km. Error limits are for ΔV : 10 km^3 and for A_{dd} : 5 km^2 .

Time	Δt (min)	V_{out} (km^3)	ΔV (km^3)	A_{dd} (km^2)	\bar{A}_{dd} (km^2)	\bar{w} (ms^{-1})
130429		95		39		
	4.5		18		38	2 ± 2
130901		113		37		
	4.5		33		44	3 ± 2
131334		146		52		
	4.6		100		64	6 ± 1
131910		246		77		
	5.2		160		69	7 ± 2
132419		406		61		
	5.4		170		83	6 ± 1
132943		576		105		
	5.8		174		106	5 ± 1
133529		750		107		
	5.0		176		122	5 ± 1
134031		926		138		
	5.0		179		148	4 ± 1
134532		1105		158		
Avg						5 ± 1

scan is the presence of a rear inflow into the back of the downdraft, centered at about 4 km AGL. This rear inflow appeared as a streak of strongest wind speeds, with speeds as high as 15 ms^{-1} in a ground-relative frame.

Calculations for the downdraft air speeds were made from mass balance between the downdraft and the outflow for a period of 40 minutes, and the results are summarized in Table 4.4. Though there were two downdrafts present, they are treated as a single downdraft since it is not possible to determine the separate contributions of the downdrafts to the entire outflow volume. The resulting average value for \bar{w} was 5 ms^{-1} , good to $\pm 1 \text{ ms}^{-1}$, with discrete values of \bar{w} ranging from $2\text{--}6 \text{ ms}^{-1}$. Table 4.4 indicates that the outflow

became rather large toward the end of the period, as did the combined areal coverage of the downdrafts. As the downdraft areal coverage generally maintained an upward trend, so did the outflow volume rate of increase, being largest at the end of the period when downdraft coverage was largest. The discrete values of \bar{w} were smaller at the beginning of the period when the outflow size was smaller and the downdraft was still newly developed, but as both the downdraft and outflow continued to grow in size, the values of \bar{w} increased and then leveled off, remaining fairly constant for the rest of the time.

Surface Mesonetwork Analysis

By 13:20, the gust front had entered the northeast side of the surface network, and the isochrone analysis for this case (fig. 4.20) shows that within 40 minutes, the gust front exited the south end of the network. The isochrone analysis gives a propagation speed of 12 ms^{-1} , agreeing with the 11 ms^{-1} speed observed by the radar, and as in the previous case, the downdrafts were still quite active as the gust front was traversing the surface network. In fact, the gust front had been initiated only about 20 minutes before it began to enter the network, making it the gust front initiated closest to the network. Also, because the mesonetwork data was collected for the gust front so soon after initiation, the surface analyses make this front appear to be the strongest of the MIST cases. From the data, it is evident that the gust front of 25 July is the weakest of the cases, since this gust front was weaker with an active cold source behind it than was the gust front of 14 July with a decaying cold source behind it. However, a comparison between the gust fronts of 14 July and of this case are not possible, since the fronts were in different stages of their lifecycles while they passing through the mesonetwork.

Surface analysis was carried out for this gust front at 13:50, which was within 50 minutes of gust front formation. By this time, the gust front had traversed nearly two-thirds of the network. The streamline and isotach analysis (fig. 4.21) shows, as in the previous cases, flow perpendicular to the gust front in the outflow, and a marked increase in wind speed gradient all along the front. The gust front speed is again noted to exceed the wind speeds observed at the surface behind the front, and the radar scans of Figure 4.22 show that there

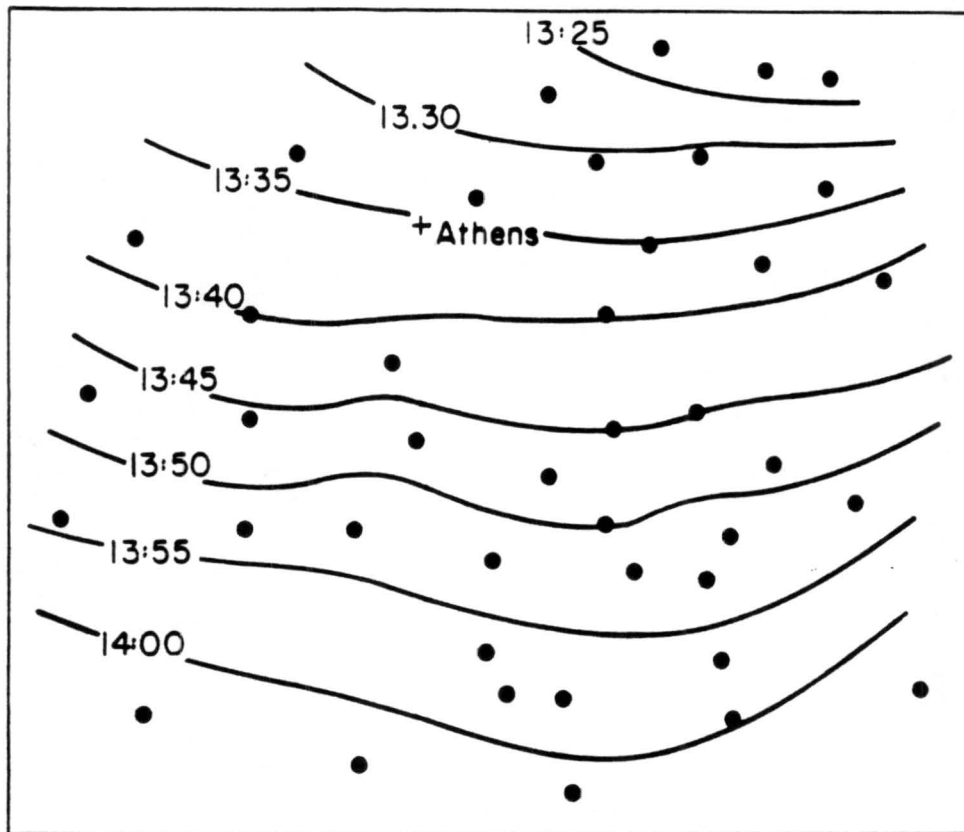


Figure 4.20: Isochrones of the leading edge of the gust front of 31 July.

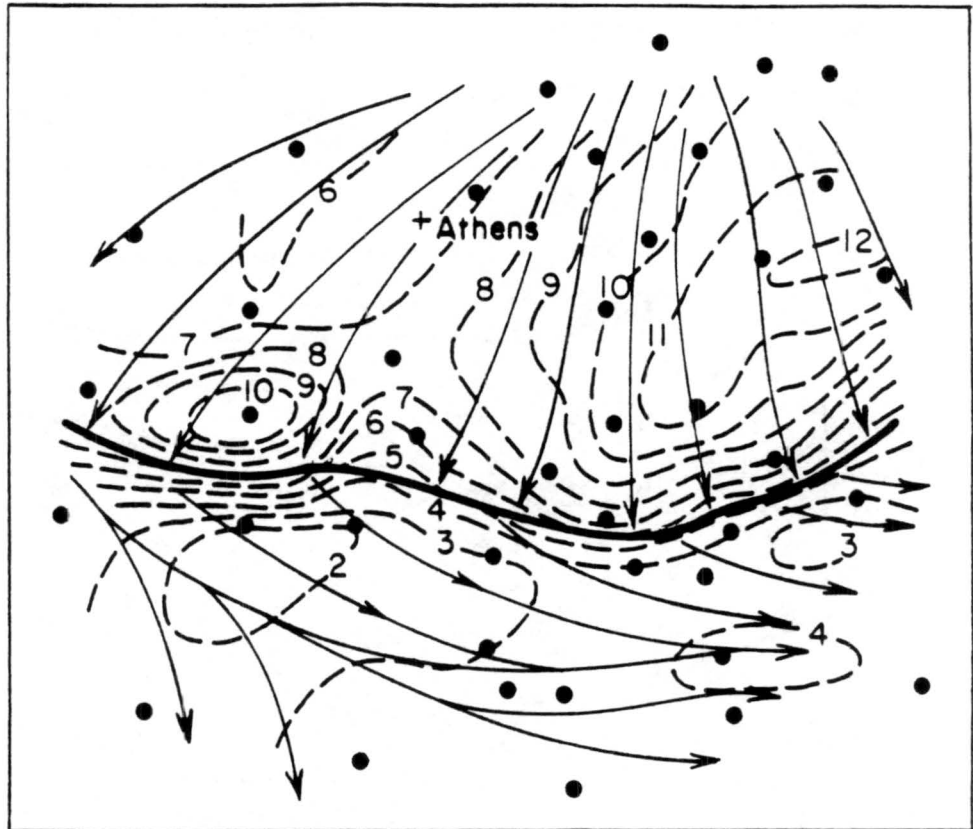


Figure 4.21: Streamline and isotach analysis at 13:50 on 31 July 1986. Streamlines are thin solid lines, isotachs are dashed lines in ms^{-1} , and the gust front is indicated by the thick solid line.

were stronger wind speeds in the outflow at some distance above the surface, illustrating the influence of friction very near the surface. Ahead of the gust front, the environmental flow was essentially parallel to the front, and the wind shift prior to gust frontal passage is also evident. The isotach analysis also reveals some evidence of two clefs along the front, with the more pronounced cleft on the western portion of the gust front, and a weakly defined one on the eastern portion of the front.

The dry-bulb temperature analysis of Figure 4.23 shows that the gust front was very well-defined as a marked gradient in temperature. The air temperature drop with the gust front passage was on the order of 8–9°C. The dewpoint analysis (fig. 4.23) is, as in the case of 25 July, somewhat confused, depending upon location, because of the downdraft positions to the rear of the gust front, but the outflow seems to appear somewhat drier than the environmental air. The clefs, while not apparent in the temperature analysis, seem to be indicated in the dewpoint analysis. The pressure analysis (fig. 4.24) shows the pressure increase with the frontal passage, and general higher pressure in the outflow, though there were localized pressure maximums, again associated with the downdraft positions. The clefs are not evident in the pressure analysis.

The divergence and vorticity fields are given in Figure 4.25. As in the other cases, pronounced convergence occurred along the entire length of the gust front, due to in this case, both wind speed and directional convergence. The outflow was characterized by general divergence, with localized maximums, all due to the downdrafts in the convective area following the front. The vorticity field shows several areas of rotation along and to the rear of the gust front. The largest cyclonic rotations occurred along the front, and the largest anticyclonic rotations occurred in the outflow in association with the downdrafts.

4.2 CINDE cases

The CINDE project was run in the summer of 1987 in northeast Colorado near Denver. The purpose of CINDE was the study of processes leading to the initiation of convective storms and their downdrafts, and the processes involved in the forcing of these downdrafts. Since gust fronts play an important part in the initiation of new convection, gust front-

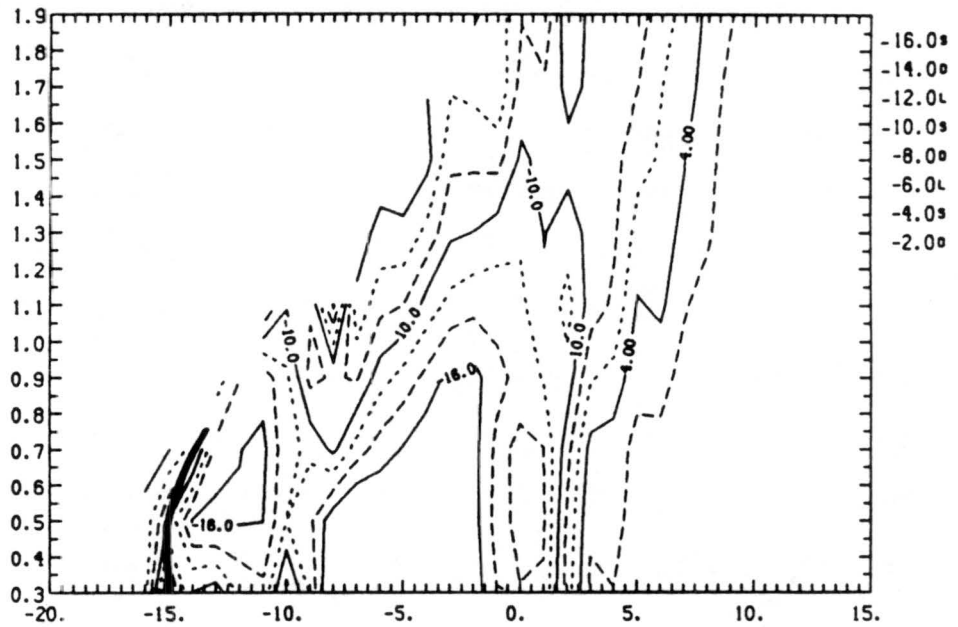
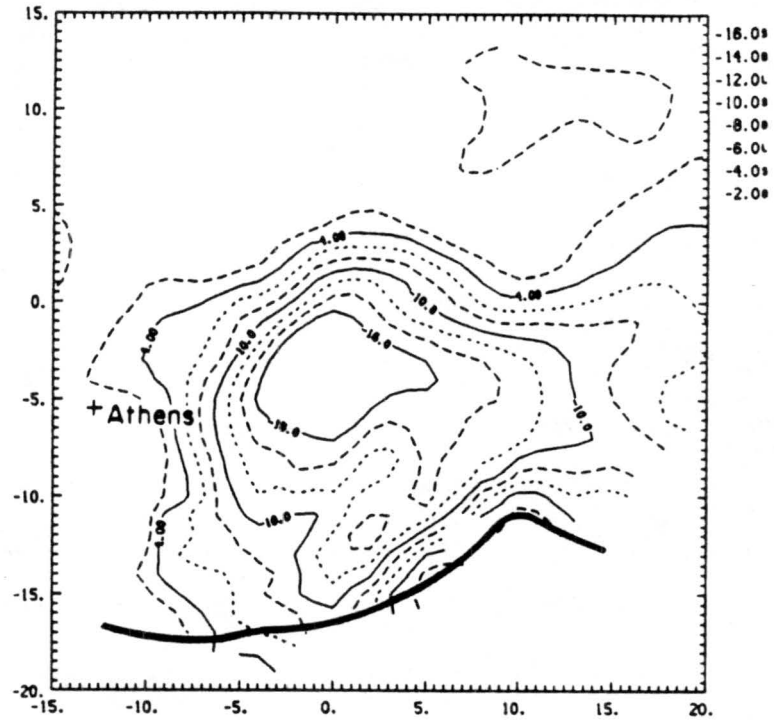


Figure 4.22: PPI and RHI scans at 13:51 showing observed radial velocities associated with the gust front of 31 July 1986. Scan height is 0.5 km AGL, ground level is 0.2 km MSL, and the FL-2 Doppler radar is located at (2.4,-21.7).

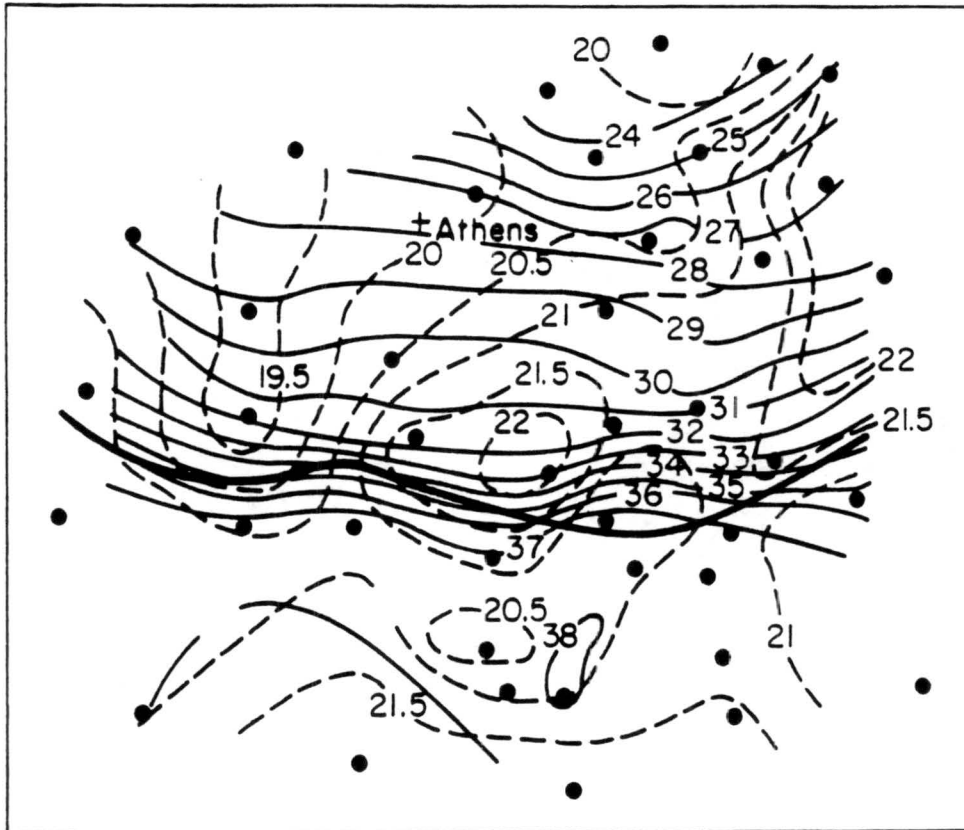


Figure 4.23: Dry-bulb and dewpoint temperature analysis associated with the gust front of 31 July 1986. Solid lines are isotherms in °C, dashed lines are isodrosotherms in °C, and the thick solid line is the gust front.

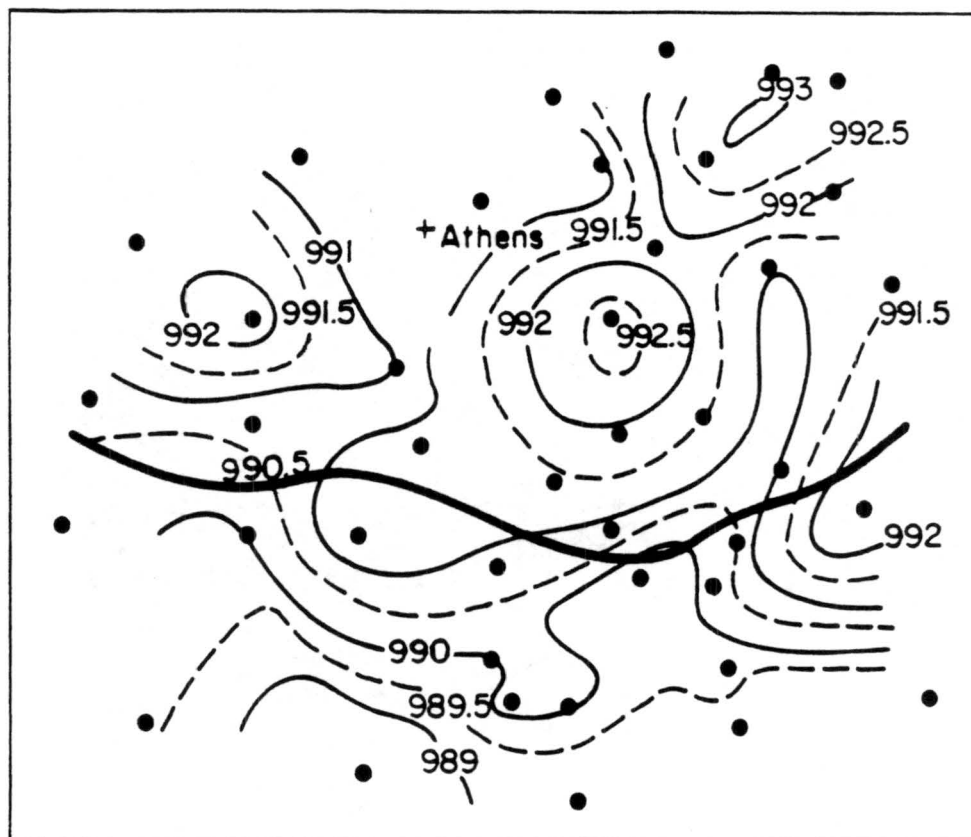


Figure 4.24: Surface pressure field associated with the gust front of 31 July 1986. Contours are in 0.5 mb increments with solid lines representing whole values and dashed lines representing half-values. Pressures have been adjusted to the mean height of the network, which is 201 m.

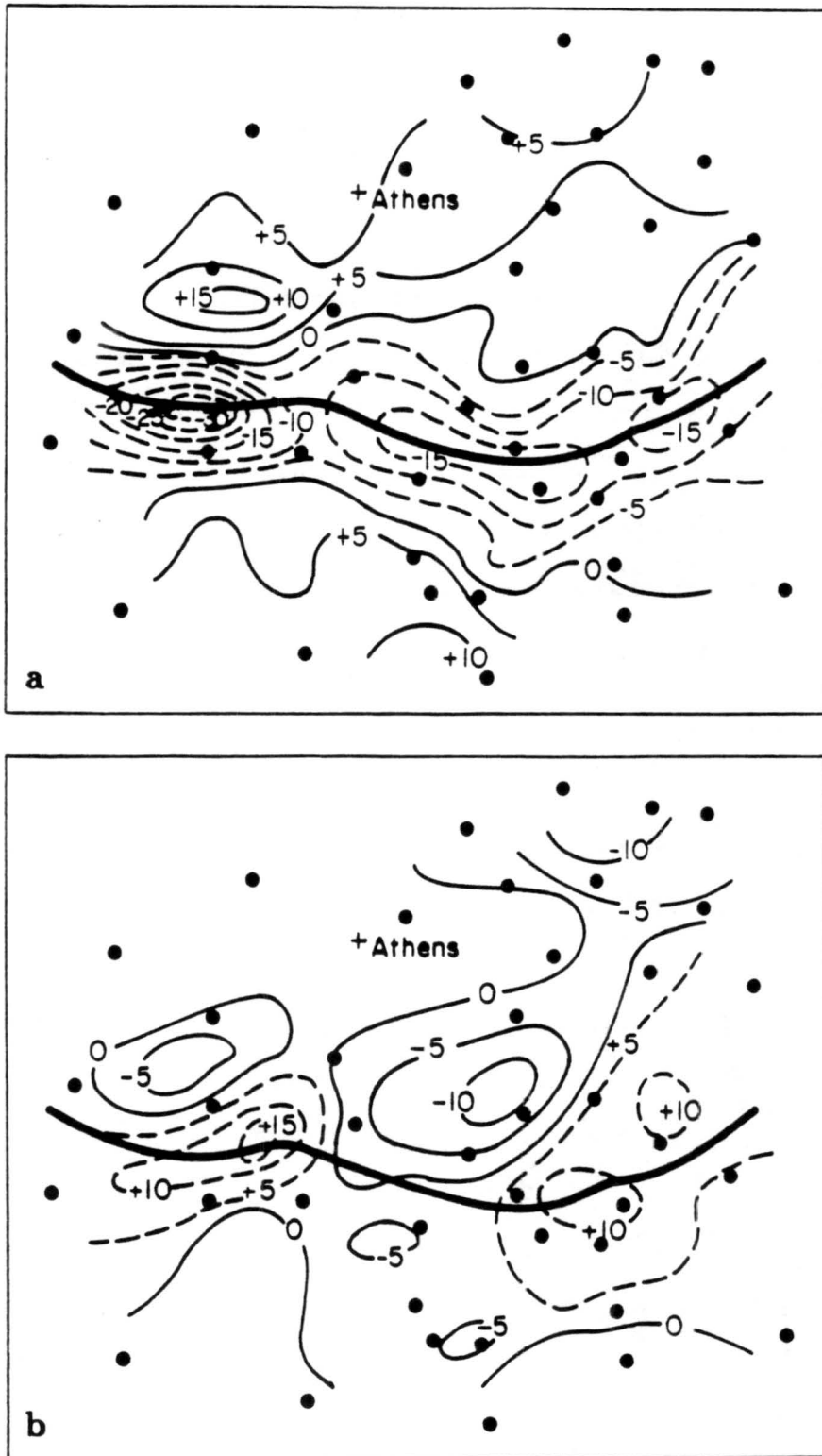


Figure 4.25: Divergence (a) and vorticity (b) fields associated with the gust front of 31 July 1986. In (a), solid lines indicate divergence and dashed lines indicate convergence ($s^{-1} \times 10^{-4}$), and in (b), solid lines indicate anticyclonic vorticity and dashed lines indicate cyclonic vorticity ($s^{-1} \times 10^{-4}$).

outflow systems were documented well with Doppler radar and surface mesonetwork data during CINDE.

Three days from the CINDE program were chosen for analysis, providing five outflow-gust front cases. Two of these cases were isolated thunderstorm cases, where the storms produced radial outflows, and they were used to calculate downdraft speeds, while for the other three cases, the parent thunderstorms were never found. Four of the five gust fronts either formed within the surface mesonetwork or moved into the network at some point in their life cycles, and these four gust fronts were used to address the accuracy of the density current approximation. Table 4.5 summarizes the observed changes in temperature, dewpoint, and pressure at the surface with the passage of these gust fronts. A complete discussion of each gust front is included in this section.

4.2.1 27 June 1987

Doppler radar observed two separate outflow-gust fronts on this day, and these will herein be referred to as GF A and GF B. GF A was associated with a thunderstorm cell that the radar observed from formation to dissipation. Mass balance calculations are available for GF A, but since it did not move into the surface mesonetwork, surface data is not available. GF B is of unknown origin, but the radar observed it for over an hour as it moved southward. GF B eventually moved into the mesonetwork, and surface data is available. The parent thunderstorm of GF B was not found, so mass balance calculations were not made for this gust front.

GF A

Doppler radar observed the formation of a thunderstorm and its associated outflow and gust front in the early afternoon hours of 27 June. The cell formed over the Colorado Rocky Mountains, to the northwest of the radar, and then proceeded to move southeastward over the adjacent plains. The radar observed the storm from formation to dissipation, which was over 60 minutes in duration. During the life cycle of the storm, it produced an outflow and gust front, making it of interest to this study.

Table 4.8: Surface observations from the NCAR PAM II mesonet stations, associated with the passage of each CINDE gust front. T , T_d , and p are dry bulb temperature, dewpoint temperature, and pressure, respectively.

Date		$\overline{\Delta T}$ (C°)	ΔT_{max} (C°)	ΔT_{min} (C°)	$\overline{\Delta T_d}$ (C°)	$\Delta T_{d_{max}}$ (C°)	$\Delta T_{d_{min}}$ (C°)	$\overline{\Delta p}$ (mb)	Δp_{max} (mb)	Δp_{min} (mb)
27 June 1987	GF B	-3.2	-5.0	-1.8	+2.5	+4.8	+1.1	0.59	0.79	0.47
28 July 1987	GF X	-5.6	-10.7	-2.5	+3.6	+5.7	+1.1	0.78	1.19	0.35
	GF Y	-6.3	-11.3	-3.1	+4.7	+6.7	+1.0	0.39	0.67	0.16
6 August 1987		-7.9	-10.4	-4.9	+6.3	+10.0	+3.4	1.60	2.68	1.10

On 27 June, the NCAR CP-3 Doppler radar observed the formation of an isolated thunderstorm over the Colorado Rockies. The thunderstorm formed early in the afternoon at about 13:30 MDT, 75 km to the northwest of the radar site. No sounding data are available for the pre-storm environment or through the outflow. Once the storm had formed, it began to move southeastward at 11 ms^{-1} . Within about 15 minutes, it developed a downdraft, and by this time, it had moved off of the foothills and onto the adjacent plains. By 13:55, a gust front had become visible in the radar PPI scans.

The thunderstorm was most intense during its time over the foothills of the Rockies, when it had associated reflectivity factors to 55 dBZ and a top to over 7 km AGL. As the thunderstorm moved off of the foothills, it began to rain out, and the reflectivity factors quickly dropped to maximum values just over 35 dBZ. It was as the storm rained out that gust front formation occurred. The gust front appeared weakly in the reflectivity field as a diffuse band of up to about 7 dBZ, but it was better defined in the radial velocity field, where it was evident that the outflow was radial in nature. The radar observed the gust front to be expanding radially away from the downdraft at 9 ms^{-1} .

Figure 4.26 shows the thunderstorm and outflow as they appeared in the radar PPI scans at 14:12. The storm is seen to be nearly centered over the outflow, which is associated with reflectivity factors of less than 7 dBZ. In the radial velocity field, the gust front appears as a gradient on the southeast side in negative velocity values, while on the northwest and north sides, the velocities become weakly positive. Noting that the velocities are in a ground-relative frame, it is evident that the outflow was radial in nature, with the 0 ms^{-1} velocity contour running roughly northwest to southeast, perpendicular to the gust front and beneath the downdraft, which was associated with the 30 dBZ contour. The radar observed wind speeds in the outflow of $8\text{--}10 \text{ ms}^{-1}$ ahead of the downdraft, with speeds of up to 12 ms^{-1} at the base of the downdraft.

An RHI scan through the thunderstorm and outflow is given in Figure 4.27. The downdraft was outlined by the 30 dBZ contour in the reflectivity field, and the leading edge of the outflow appeared as the 7 dBZ contour. The gust front was located over 10 km ahead of the downdraft center on both sides. The storm extended to over 7 km AGL. In the

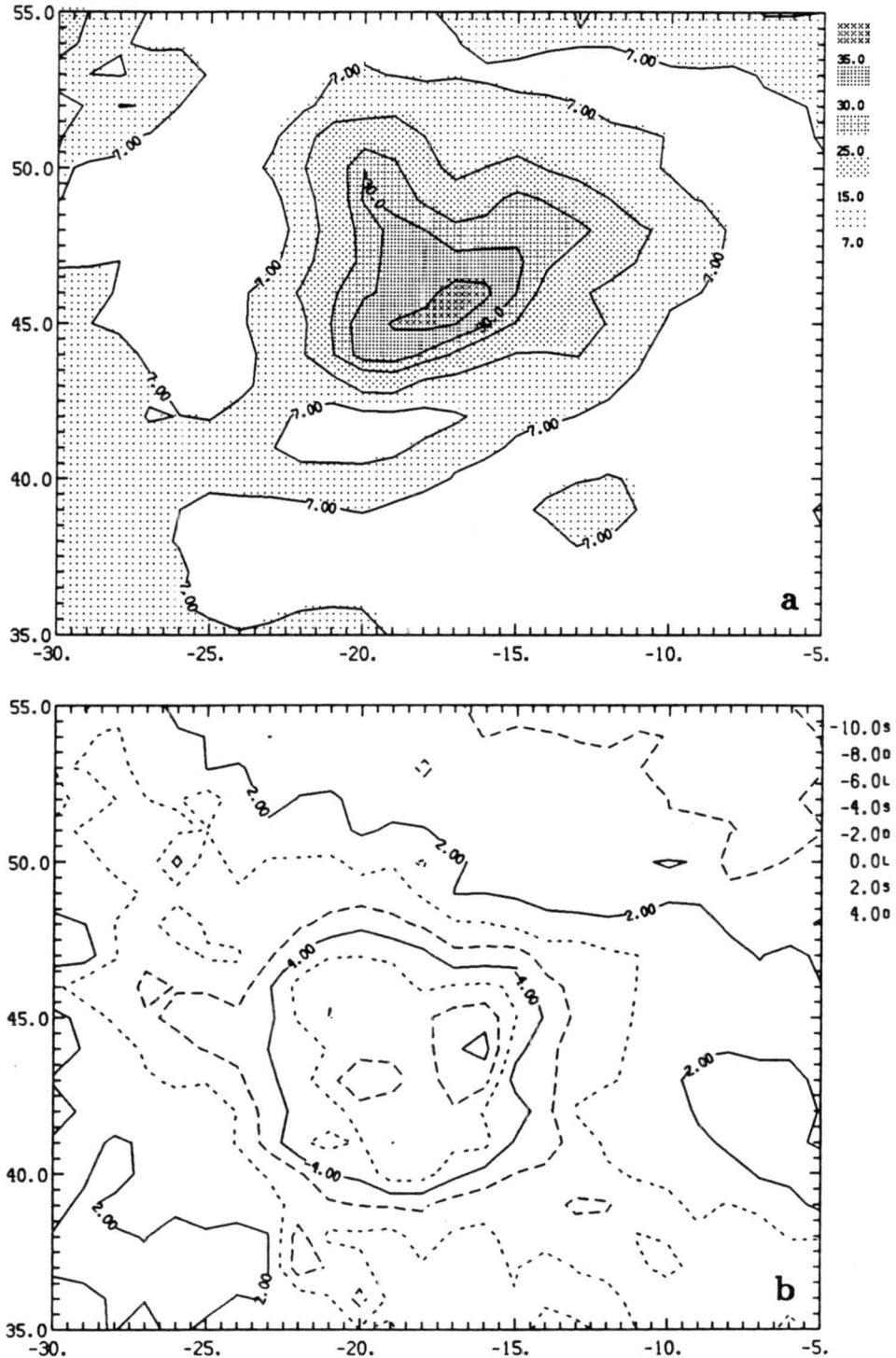


Figure 4.26: PPI scans at 14:12 for the thunderstorm and outflow of GF A of 27 June, showing in (a) the reflectivity field and in (b) the radial velocity field. The scan height is 0.6 km AGL and the NCAR CP-3 Doppler radar is located at (0,0).

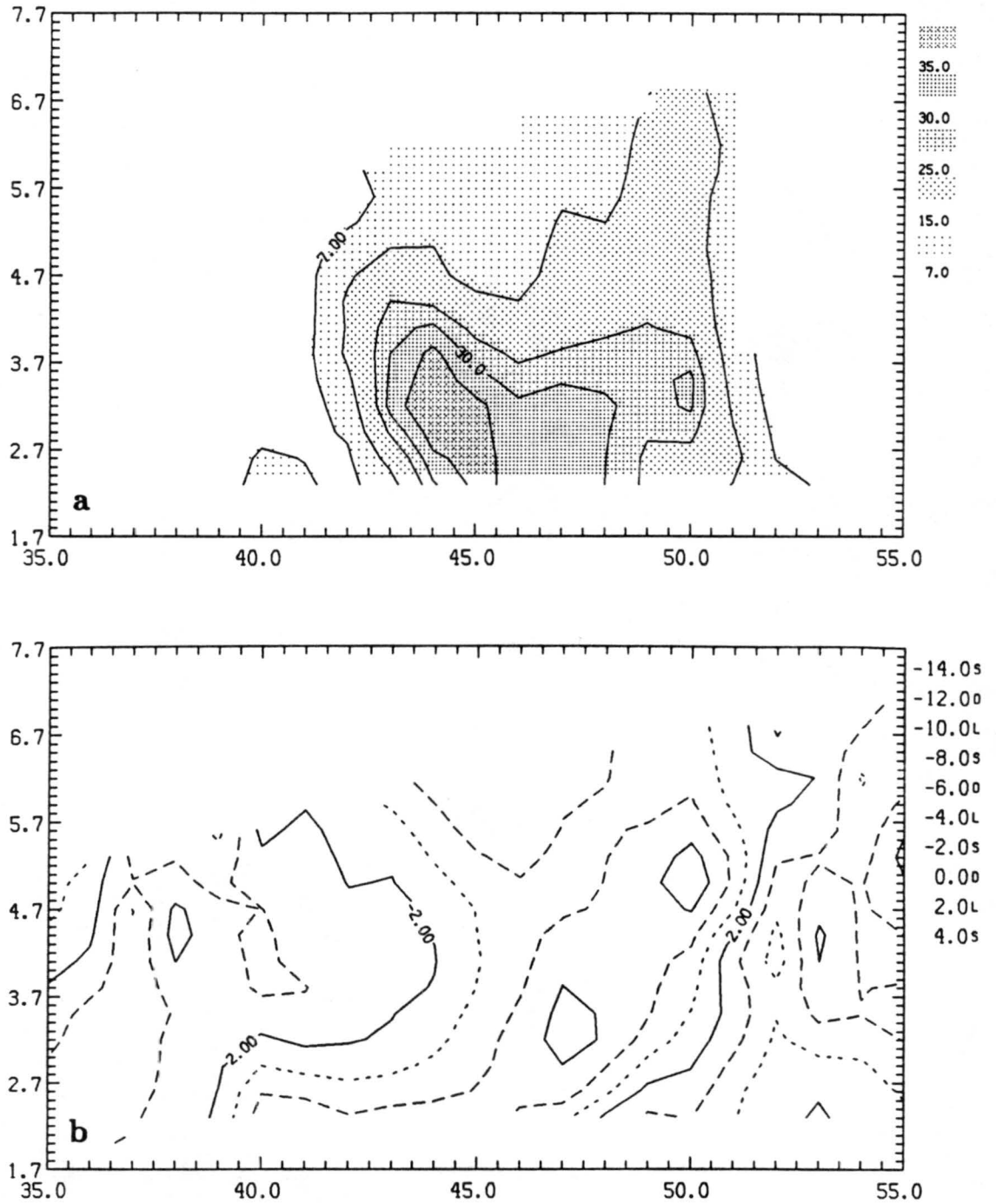


Figure 4.27: RHI scan at 14:12 through the storm and outflow of GF A of 27 June, showing in (a) the reflectivity field and in (b) the radial velocity field. Ground level is 1.6 km MSL.

radial velocity field, the top and leading edges of the outflow appeared as a gradient in the velocities. The head of the outflow was well-defined, and extended up to 1.6 km AGL, while the mean outflow depth was about 0.8 km. The RHI scan also indicates the radial configuration of the outflow, with air moving both ahead of and to the rear of the downdraft. Wind speeds observed by the radar were stronger ahead of the downdraft because the speeds are in a ground-relative frame, and this was the direction in which the storm was moving.

Calculations for the downdraft air speed obtained by mass balance are summarized in Table 4.6. These calculations were carried out for the downdraft for a period of over 26

Table 4.6: Mass balance calculations of downdraft speeds from the outflow of GF A of 27 June. The outflow height $h=0.8$ km. Error limits are for ΔV : 5 km^3 and for A_{dd} : 2 km^2 .

Time	Δt (min)	V_{out} (km^3)	ΔV (km^3)	A_{dd} (km^2)	\bar{A}_{dd} (km^2)	\bar{w} (ms^{-1})
140326		77		21		
	4.7		51		18	10 ± 3
140809		128		15		
	4.7		39		16	9 ± 3
141251		167		16		
	4.7		63		18	12 ± 3
141733		230		19		
	4.7		76		17	16 ± 4
142215		306		15		
	4.7		42		14	11 ± 4
142657		348		12		
Avg						12 ± 3

minutes, extending from about the time the gust front formed to just prior to downdraft dissipation. The average value for \bar{w} calculated is 12 ms^{-1} , good to $\pm 3 \text{ ms}^{-1}$, with discrete values for \bar{w} ranging from 9 to 16 ms^{-1} . From Table 4.6, it is apparent that the downdraft was rather small, especially in relation to the cases in MIST. This seems to be a result of the storm being isolated convection, and not associated with some larger-scale system. The

downdraft areal coverage seems to have remained fairly constant, except at the end of the period, when it was beginning to dissipate. The volume rate of increase for the outflow, which was not very large, was rather steady over the 26 minute period, but there was some oscillation, and this led to an oscillation in the calculated values for \bar{w} .

Unlike with the cases in MIST, this outflow did not move into the surface mesonet network at any time, and no surface data are available, so no assessment of how the density current approximation predicts gust front speed can be made for this situation. Another gust front did, however, move into the network, and surface data were collected as it passed over the stations. This gust front, GF B, is discussed in the next subsection.

GF B

This gust front was of unknown origin, since the parent thunderstorm was never found in the radar scans. Either the thunderstorm was out of range of the CP-3 radar, or else it had already dissipated. The radar first observed the gust front at around 15:42 MDT, at a range of 55 km from the radar. Before this time, it is likely that even the lowest elevation scan, which was 0.4° , was looking above the gust front due to the curvature of the earth. The gust front appeared in the PPI scans as a well-defined band of up to 20 dBZ when it was first observed. The radar observed propagation speed was 11 ms^{-1} , and the gust front was moving southward. By 16:25, the gust front had just edged into the northern portion of the network. As it continued its southward movement through the network, it began to show signs of losing its identity. It is suspected that the outflow by this time had been propagating without the aid of an active cold source for some time.

Surface analyses for this gust front were carried out at 17:00 MDT. This is the only case out of six where the gust front appears to be dying as it moves through the network, and the analyses depict this quite nicely. The isochrone analysis (fig. 4.28) shows that after about 45 minutes in the network, the gust front had essentially lost its identity. The propagation speed calculated from this analysis is 10 ms^{-1} , agreeing with the speed observed by the radar.

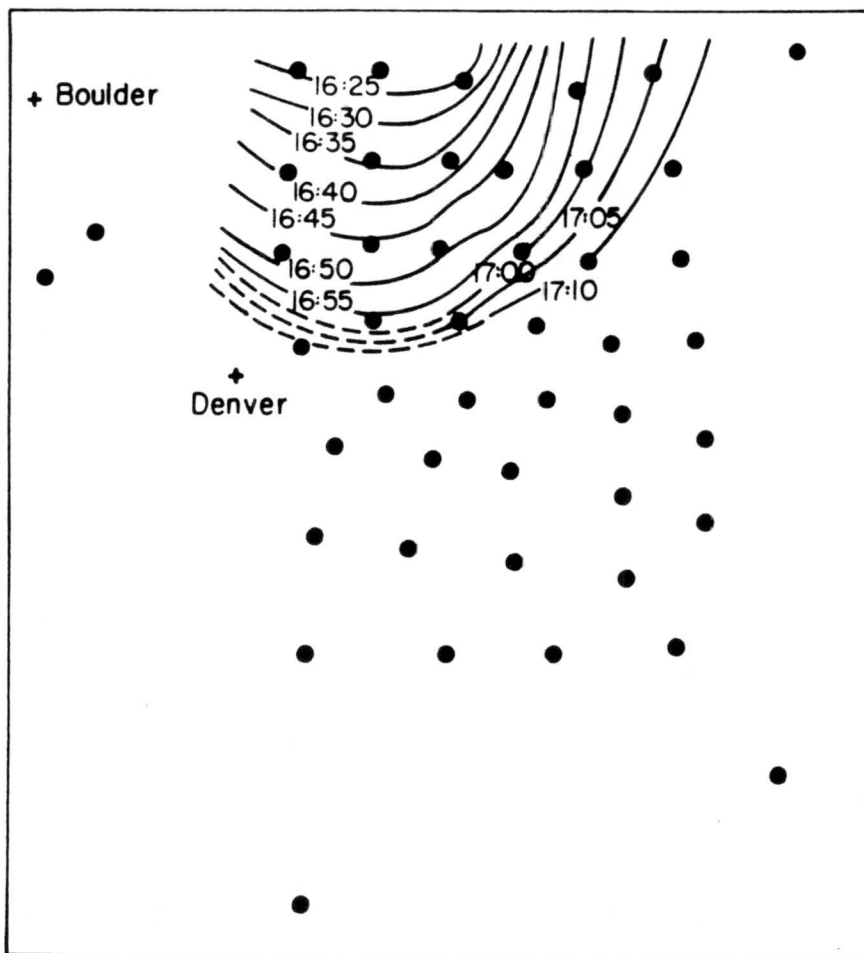


Figure 4.28: Isochrones of the leading edge of GF B of 27 June.

The wind field associated with this gust front is given in Figure 4.29. The streamline analysis shows that winds within the outflow were still flowing perpendicular to the gust front orientation, even as it was dying. This indicates that even after a gust front has lost many of its characteristics, it may still continue on as a wind shift or convergence line. Thus, it may still go on to initiate new convection if conditions are favorable. Out ahead of the gust front, the winds were nearly perpendicular to the axis of gust front motion. The isotach analysis shows that the strongest winds were behind the eastern portion of the gust front, and the subsequent analyses will show that, at this time, the western portion of the gust front had lost most of its identity, while the eastern portion still retained gust front characteristics. Radar scans at 16:48 (fig. 4.30) show that the radar observed wind speeds were somewhat stronger than those observed at the surface by the network stations, again illustrating the effects of friction near the surface.

The temperature and dewpoint field associated with this gust front are shown in Figure 4.31. The gust front, on its eastern side, was weakly defined as a gradient in both dry-bulb and dewpoint temperatures. On its western side, no well-defined gradient existed, indicating the weakening of the gust front as mixing between the outflow and environmental air was occurring. Where the outflow was somewhat defined, it appeared as cooler, moister air, relative to the environment. The pressure field (fig. 4.32) shows that there was general higher pressure in the outflow, as well as a pressure rise associated with the passage of the gust front. Along the weaker portion of the front, the pressure rise was ill-defined, while along the stronger portion, there was about 1 mb of pressure increase in the outflow over the environment.

The divergence and vorticity fields are given in Figure 4.33. There is evidence of weak convergence along the entire length of the gust front, which is in keeping with the observations of the other cases. The outflow itself was characterized by divergence, mostly behind the eastern portion of the gust front, where the front had a large bend in it. The vorticity field (fig. 4.33b) shows that there was some cyclonic rotation just behind the bend on the east side of the front. Other areas of rotation occurred ahead of the front, and these coincided with the rotations implied by the streamline analysis of Figure 4.29.

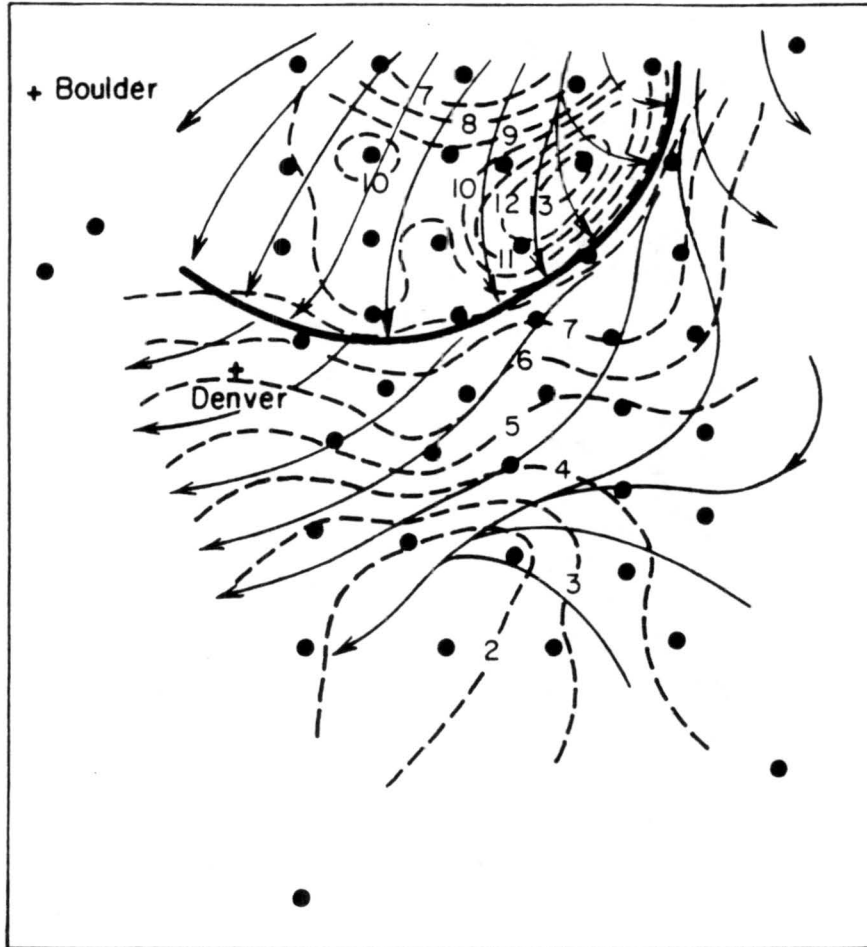


Figure 4.29: Streamline and isotach analysis at 17:00 on 27 June 1987. Streamlines are thin solid lines, isotachs are dashed lines in ms^{-1} , and the gust front is indicated by the thick solid line.

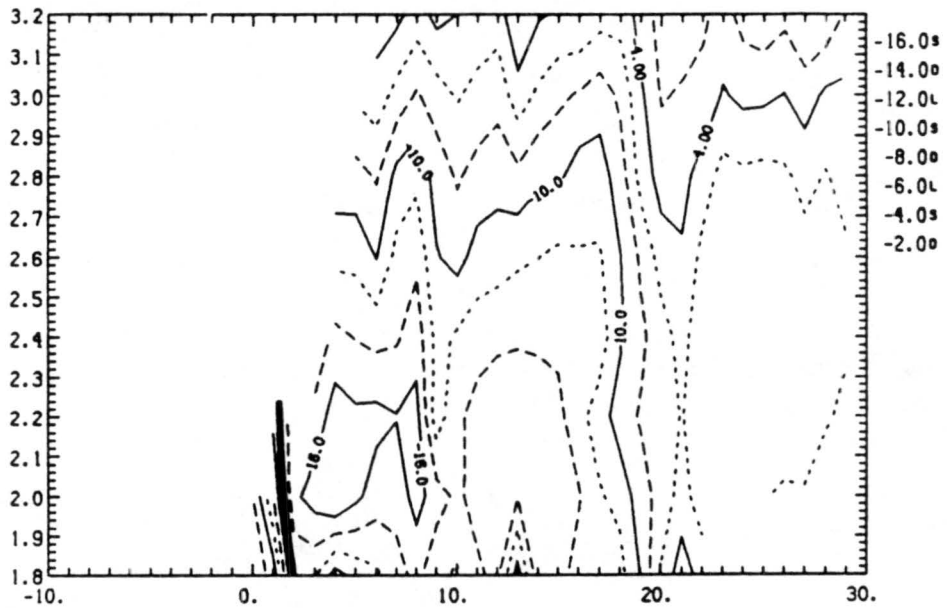
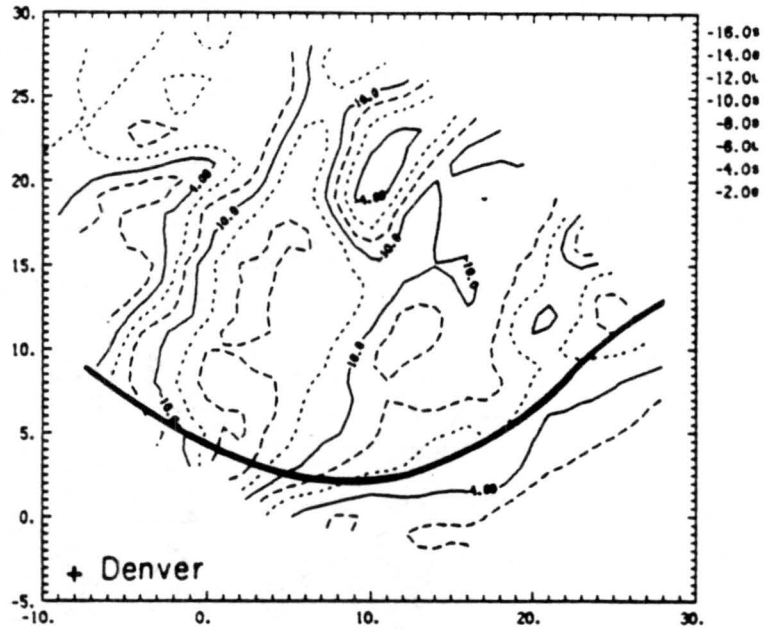


Figure 4.30: PPI and RHI scans at 16:58 showing observed radial velocities associated with GF B of 27 June 1987. Scan height is 0.6 km AGL, ground level is 1.6 km MSL, and the CP-3 Doppler radar is located at (0,0).

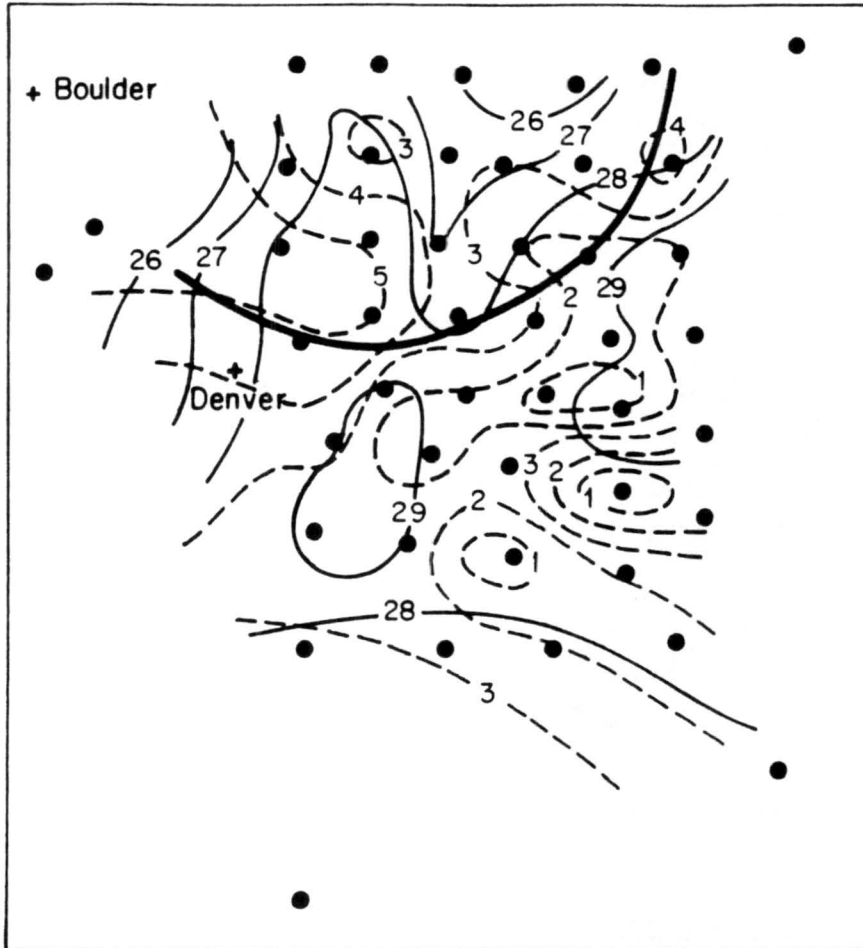


Figure 4.31: Dry-bulb and dewpoint temperature analysis associated with the gust front of 27 June 1987. Solid lines are isotherms in $^{\circ}\text{C}$, dashed lines are isodrosotherms in $^{\circ}\text{C}$, and the thick solid line is the gust front.

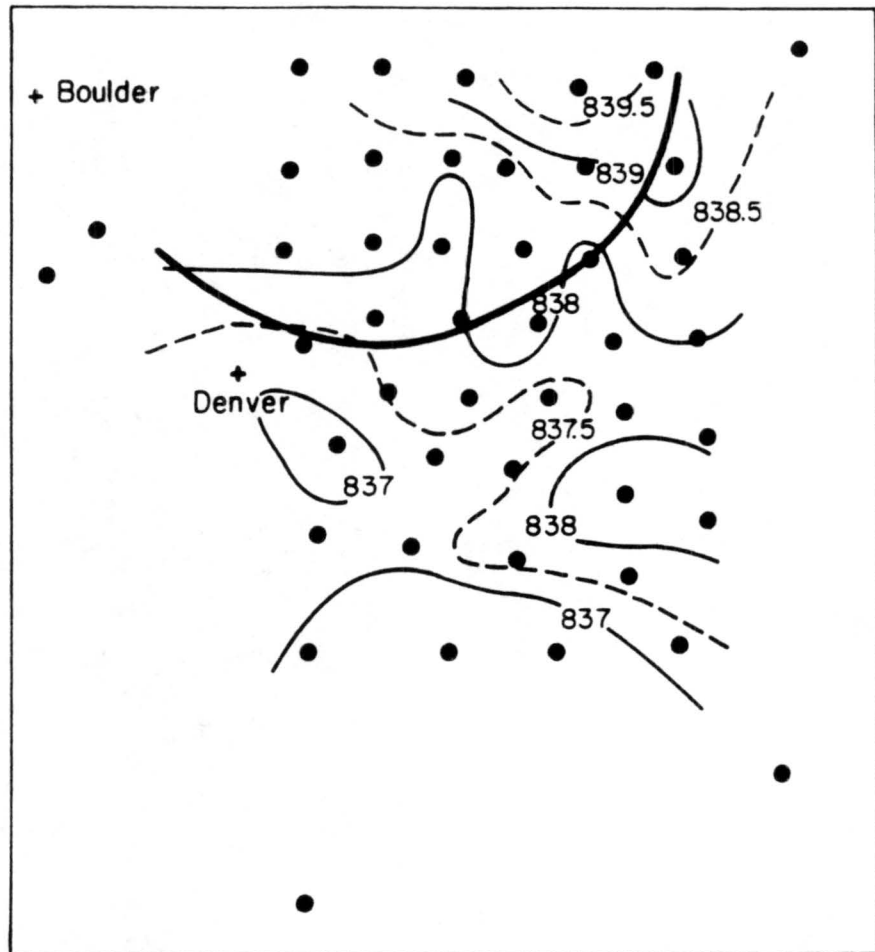


Figure 4.32: Surface pressure field associated with the gust front of 27 June 1987. Contours are in 0.5 mb increments, with solid lines representing whole values and dashed lines representing half-values. Pressures have been adjusted to a mean height of 1594 m.

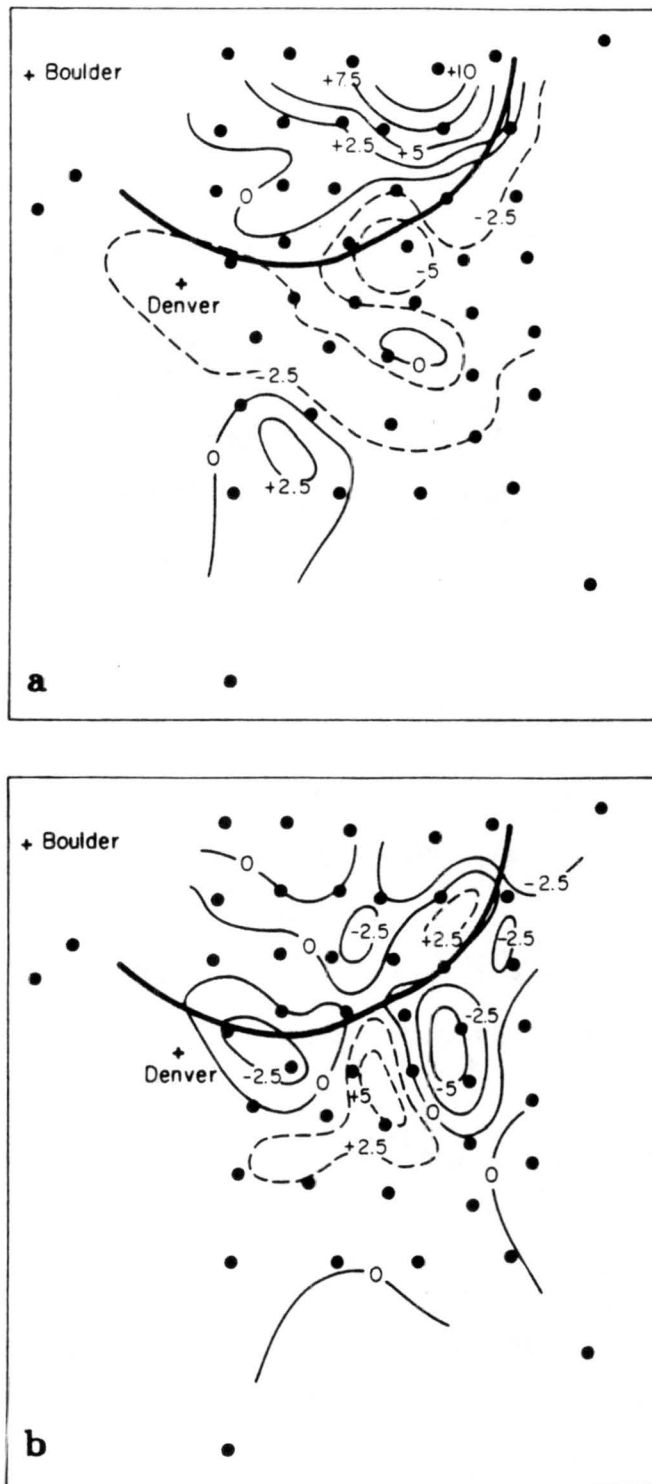


Figure 4.33: Divergence (a) and vorticity (b) fields associated with the gust front of 27 June 1987. In (a), solid lines indicate divergence and dashed lines indicate convergence ($\text{s}^{-1} \times 10^{-4}$), and in (b), solid lines indicate anticyclonic vorticity and dashed lines indicate cyclonic vorticity ($\text{s}^{-1} \times 10^{-4}$).

4.2.2 28 July 1987

Two separate gust fronts were observed on this day, both of which were located inside the surface mesonet network. Radar data is available for both gust fronts, but because the scans do not cover the entire outflow behind one of the gust fronts, calculations made from mass balance were made only for the other outflow. Surface data, however, is available for both gust fronts and outflows. What is probably the most interesting facet of the two gust fronts of 28 July is that they collide over the surface network. Surface analysis was carried out for a time after which the gust front collision had occurred, and several interesting features associated with the collision are revealed in these analyses. From this point on, the two gust fronts will be referred to as GF X and GF Y, so as to differentiate between the two, and also to avoid confusion with GF A and GF B of 27 June.

Radar Analysis

Doppler radar on this day observed the formation of an isolated thunderstorm and its associated outflow in the mid-afternoon hours. This storm formed to the northeast of Denver, over the high plains of Colorado. From formation to dissipation, the entire life cycle of the thunderstorm lasted about 30 minutes. During this time, the thunderstorm initiated a gust front and outflow, making it of interest to this study.

On 28 July, the FLOWS FL-2 Doppler radar observed the formation of an isolated thunderstorm to the northeast of Denver, CO. The thunderstorm formed in the mid-afternoon hours, at about 16:40 MDT, and was located 35 km northeast of the radar site. No sounding data are available for the pre-storm environment or through the depth of the outflow. After formation, the storm began to move northwestward, and the radar observed a speed of 6 ms^{-1} . Within about ten minutes of genesis, the storm developed a downdraft, and subsequently initiated an outflow and gust front, GF Y.

The cell became fairly strong, attaining maximum reflectivity factors of over 60 dBZ and a top to over 8 km AGL. Just after the downdraft formed, a gust front was initiated, which proceeded to expand radially away from the parent downdraft. This gust front became

visible in the radar PPI scans as a band of up to about 5 dBZ and an region of surface divergence in the observed radial velocities, with the downdraft nearly centered over the downdraft.

The PPI scans of the reflectivity and radial velocity fields at 16:57 are shown in Figure 4.34. The downdraft, which was associated with the 35 dBZ contour, was seen to be centered over the outflow, which was defined by reflectivities below about 1 dBZ. The leading edge of the outflow appeared as a band of up to about 5 dBZ. In Fig. 4.34a, the outflow of interest can be seen to be nearing collision with the outflow boundary of GF X on this day, which was approaching from the southwest as this outflow was expanding radially away from its parent downdraft. The radial velocity field shows that the outflow appeared as surface divergence in the observed velocities, with the 0 ms^{-1} contour running nearly northwest to southeast and perpendicular to the gust front, indicating the radial nature of the outflow. Air speeds measured in the outflow were weak, ranging from $5\text{--}7 \text{ ms}^{-1}$, with speeds as high as 8 ms^{-1} at the base of the downdraft.

An RHI scan through the outflow and downdraft are shown in Figure 4.35. The leading edge of the outflow is not shown well in the reflectivity field because of the confused situation caused by the proximity of the other outflow. It was visible in the radial velocity field, however, and it was located about 5 to 7 km distance from the downdraft. Its leading edge and top were marked by a gradient in the observed radial velocities, and a mean depth of 1.0 km was observed. Weak inflow into the storm updraft can be seen on either side of the downdraft, above the low-level outflow.

Calculations of the downdraft air speeds were made from mass balance for the outflow and downdraft for a period of 15 minutes, and the results are summarized in Table 4.7. This period of time extended from soon after gust front initiation to just prior to downdraft dissipation. The resulting average value for \bar{w} is 11 ms^{-1} , good to $\pm 3 \text{ ms}^{-1}$, and this is very similar to that obtained for the outflow of 27 June, which was another isolated thunderstorm situation. Table 4.7 shows that during the 15 minute time period, the volume rate of increase of the outflow remained nearly steady, as did the downdraft areal coverage, though it did begin to decrease at the end as the downdraft began to dissipate. This resulted in nearly

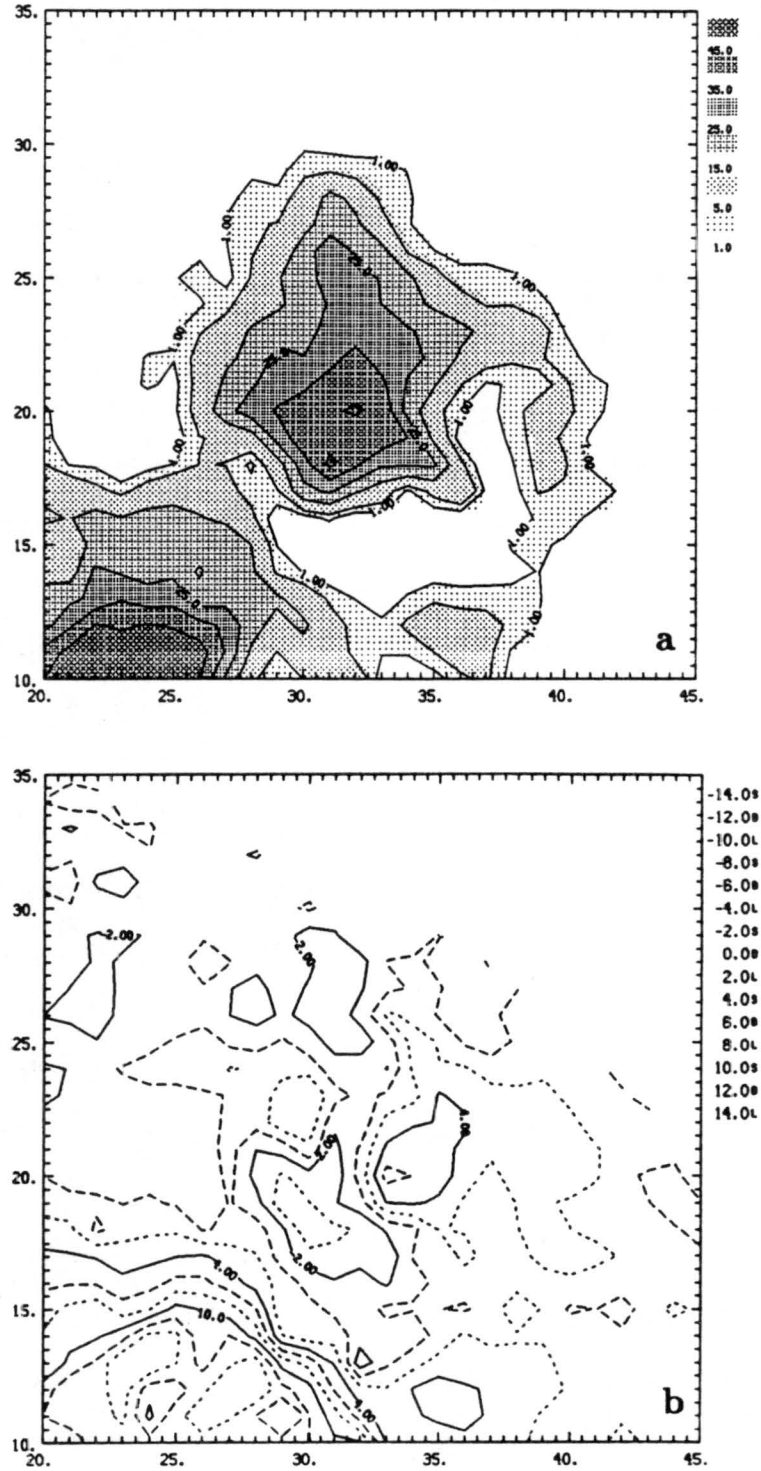


Figure 4.34: PPI radar scan for the outflow of GF Y of 28 July 1987 showing in (a) the radar reflectivity field and in (b) the radial velocity field. The scan height is 0.5 km AGL and the FLOWS FL-2 radar is located at (11.4, -7.8).

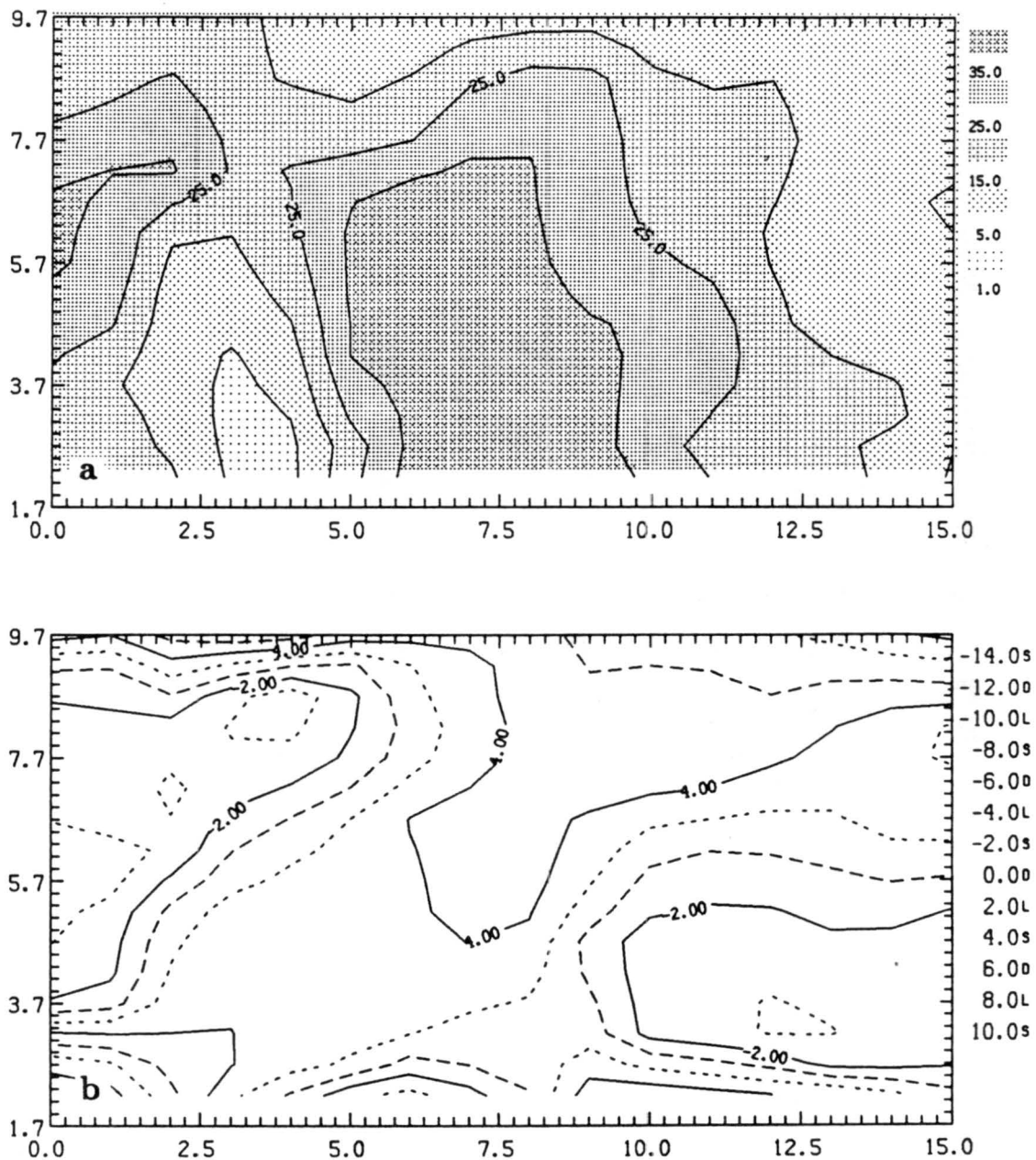


Figure 4.35: RHI scan at 16:57 through the outflow and downdraft of GF Y of 28 June, showing in (a) the reflectivity field and in (b) the radial velocity field. Ground level is at 1.7 km MSL.

Table 4.7: Mass balance calculations of downdraft speeds from the outflow of GF Y of 28 July. The outflow height is $h=1.0$ km. Error limits are for ΔV : 5 km^3 and for A_{dd} : 2 km^2 .

Time	Δt (min)	V_{out} (km^3)	ΔV (km^3)	A_{dd} (km^2)	\bar{A}_{dd} (km^2)	\bar{w} (ms^{-1})
164730		68		17		
	5.0		55		18	10 ± 3
165230		123		19		
	5.0		57		19	10 ± 3
165731		180		19		
	5.0		61		16	13 ± 4
170232		241		12		
Avg						11 ± 3

constant discrete values for \bar{w} , which ranged from 10 to 13 ms^{-1} . This outflow was the smallest of the five cases, and the downdraft was not large either, being about the same size as the downdraft of 27 June.

Surface Mesonet Analysis

Surface analysis was carried out at 17:10 CDT, by which time the gust front collision had occurred. This collision occurred over the northeast portion of the surface mesonet. The isochrone analyses for each gust front are shown in Figure 4.36. GF X appears to have been initiated sometime around 16:20, over the southeast portion of the network. It subsequently began its movement to the north-northeast. The initiation of GF Y occurred over the northeast portion of the network before 16:50. This gust front then expanded radially away from its parent thunderstorm. The analyses of Figure 4.36 show that the outflow associated with GF Y was much smaller than the one associated with GF X. While GF X affected nearly all of the surface stations in the network, GF Y affected only 7 stations in the northeast part of the network, before GF X collided with it and then subsequently overran it. The propagation speeds for the two gust front figured by the isochrone analyses

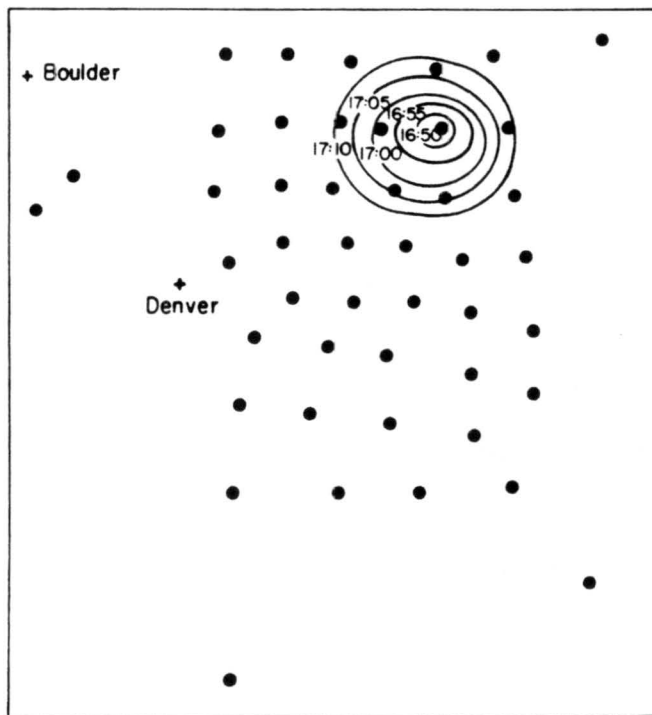
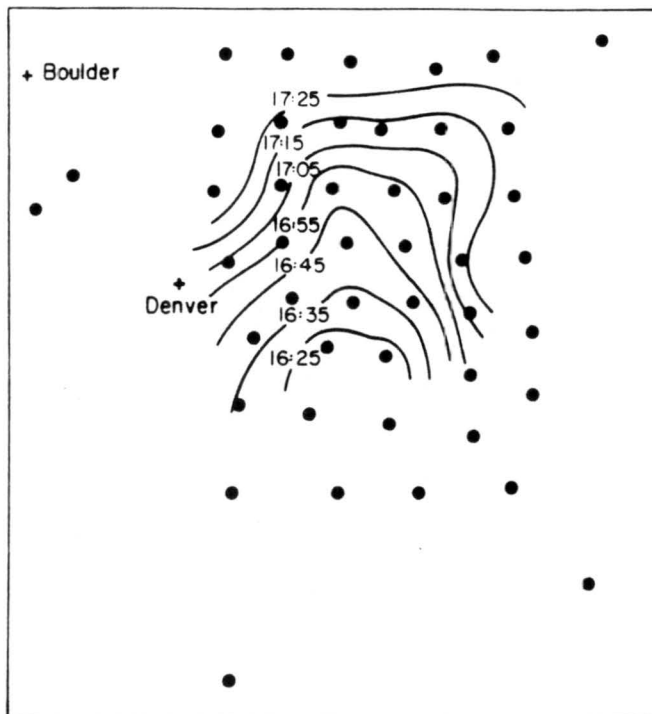


Figure 4.36: Isochrones of the leading edge of the gust fronts of 28 July.

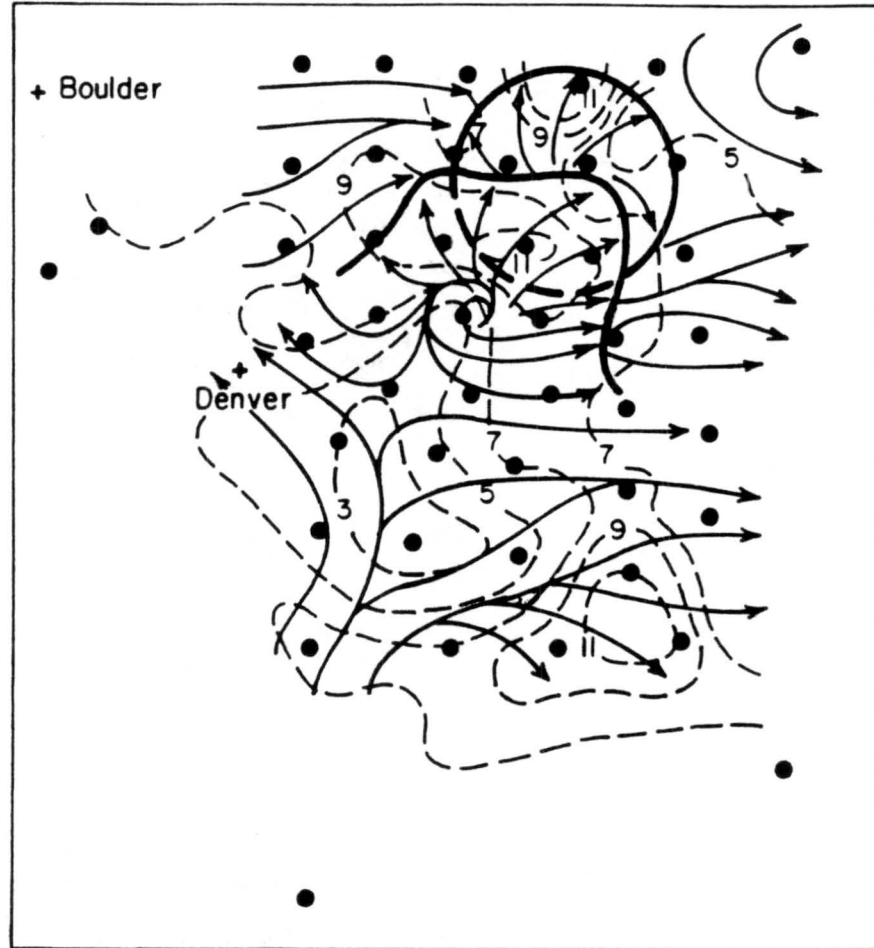


Figure 4.37: Streamline and isotach analysis at 17:10 on 28 July 1987. Streamlines are thin solid lines, isotachs are dashed lines in ms^{-1} , and the gust fronts are indicated by the thick solid lines.

are 13 ms^{-1} for GF X and 6 ms^{-1} for GF Y. Both speeds are in agreement with Doppler radar observed propagation speeds for the two fronts.

The streamline and isotach analysis of Figure 4.37 shows the wind field at 17:10, after the gust front collision had occurred. The streamline analysis indicates that there was marked divergence in the outflows behind both gust fronts. These areas of divergence were co-located with downdrafts within the two outflows. The flow behind both gust fronts was perpendicular to the fronts, as in the other cases. The radial nature of the outflow behind GF Y is nicely depicted in this analysis. The wind speeds, from the isotach analysis, were

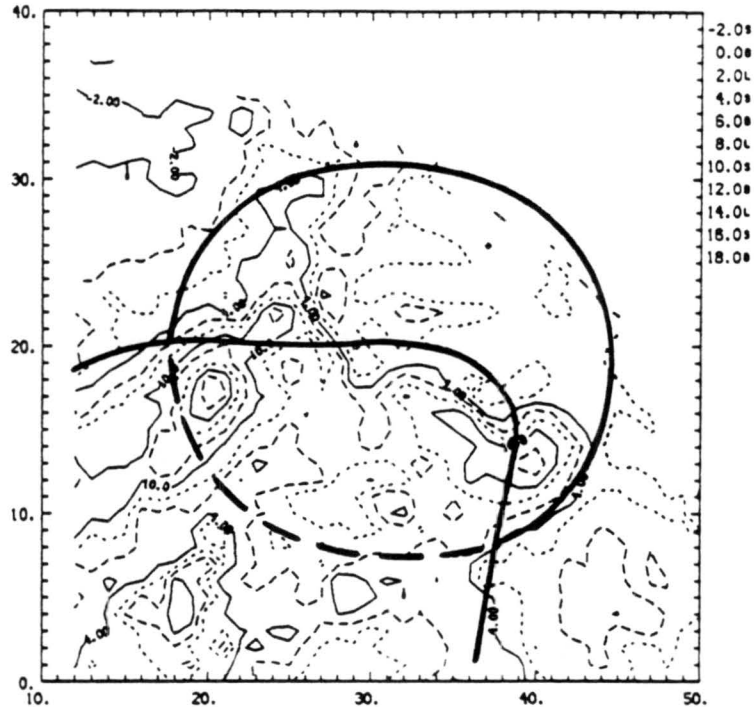


Figure 4.38: PPI scan at 17:09 showing observed radial velocities associated with the gust fronts of 28 July 1987. Scan height is 0.6 km AGL and the FL-2 radar is located at (11.4,-7.8).

strongest behind the gust fronts, though the situation became somewhat confused because of the overrunning of GF Y by GF X. The radar scan (fig. 4.38) for this time showed stronger observed winds than did the mesonetwork stations, indicating the frictional effects near the surface.

The temperature and dewpoint analysis for the gust fronts is shown in Figure 4.39. Both gust fronts appeared as steepened gradients in the temperature and dewpoint fields, with the outflows being characterized by cooler, moister air relative to the ambient environment. Evidence of the overrunning of GF Y by GF X was given in this analysis. Just behind

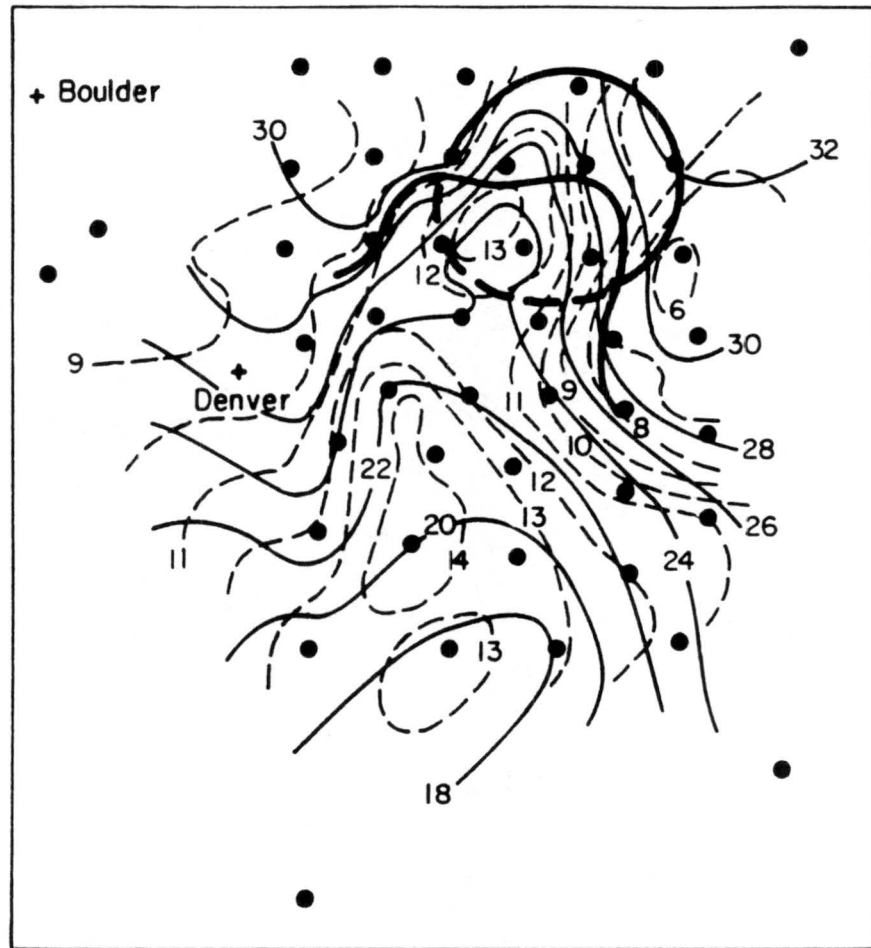


Figure 4.39: Dry-bulb and dewpoint temperature analysis associated with the gust fronts of 28 July 1987. Solid lines are isotherms in $^{\circ}\text{C}$, dashed lines are isodrosotherms in $^{\circ}\text{C}$, and the thick solid lines are the gust fronts.

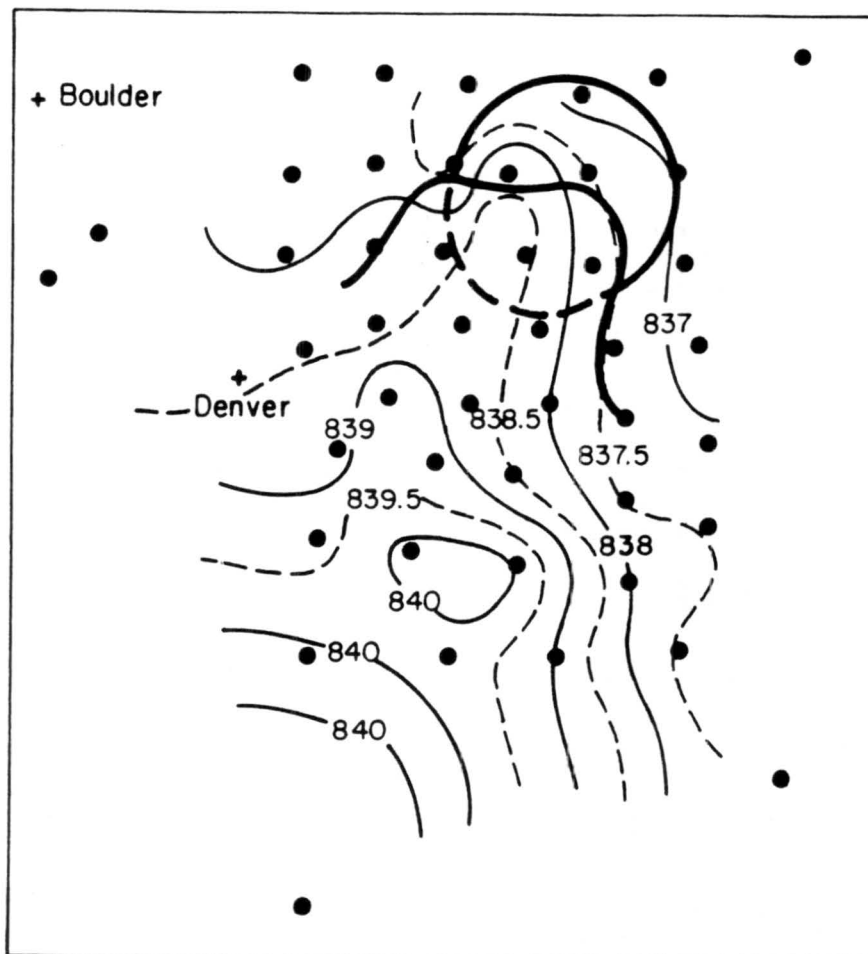


Figure 4.40: Surface pressure field associated with the gust fronts of 28 July 1987. Contours are in 0.5 mb increments, with solid lines representing whole values and dashed lines representing half-values. Pressures have been adjusted to a mean height of 1594 m.

GF X is a maximum in dewpoint and a minimum in temperature, with a second dewpoint maximum and temperature minimum much further back in the outflow. In the previous cases, it was observed that the temperature decreased steadily back from the gust front into the outflow, along with a similar trend in dewpoint, either increasing or decreasing with distance into the outflow. The difference noted here as compared to the other cases is a direct result of the overrunning of one outflow by the other. The pressure analysis (fig. 4.40) also illustrates the overrunning, with two pressure maximums behind GF X, one of which was the pressure maximum of the outflow of GF Y. The pressure rises associated with

the passages of the two gust fronts is clearly indicated by the analysis, with the outflows being characterized by the highest pressures.

The divergence and vorticity fields are given in Figure 4.41. Both gust fronts are defined as regions of enhanced convergence, but it is noted that the two gust front intersection points were associated with the largest convergence, as has been observed by other research on gust front intersections. Both outflows were characterized by weak divergence, with the largest values in association with downdrafts behind the gust fronts. The vorticity field (fig. 4.41b) indicates several areas of rotation. However, none of these seem to have been associated with the gust front intersection. The most pronounced rotational areas occurred in association with bends in the gust fronts, as well as with the downdrafts, which were again characterized by anticyclonic rotation.

4.2.3 6 August 1987

On this day, a gust front was observed to move through the surface mesonet network. This gust front had moved in from the west, so it is assumed that it probably originated somewhere in the mountains of Colorado. The FLOWS FL-2 Doppler radar was the only radar available on this day, and it shows the gust front in the PPI scans, but the parent thunderstorm was never observed, most likely due to distance from the radar. In addition, although the gust front was visible in the scans, the choices for scan azimuth limits made measurements of the gust front speed difficult. Therefore, only surface data for this gust front are used in this study.

The gust front of 6 August moved into the northwest side of the surface network during the mid-afternoon hours. The two stations to the south of Boulder were first affected, at around 16:10 MDT. Over a period of nearly an hour and a half, the gust front moved eastward across the northern half of the network, exiting on the northeast side (fig. 4.42). From the isochrone analysis, a gust front propagation speed of 15 ms^{-1} was calculated. Since the radar data show a portion of the outflow but not the gust front, no comparison can be made between radar and mesonet network observed propagation speeds.

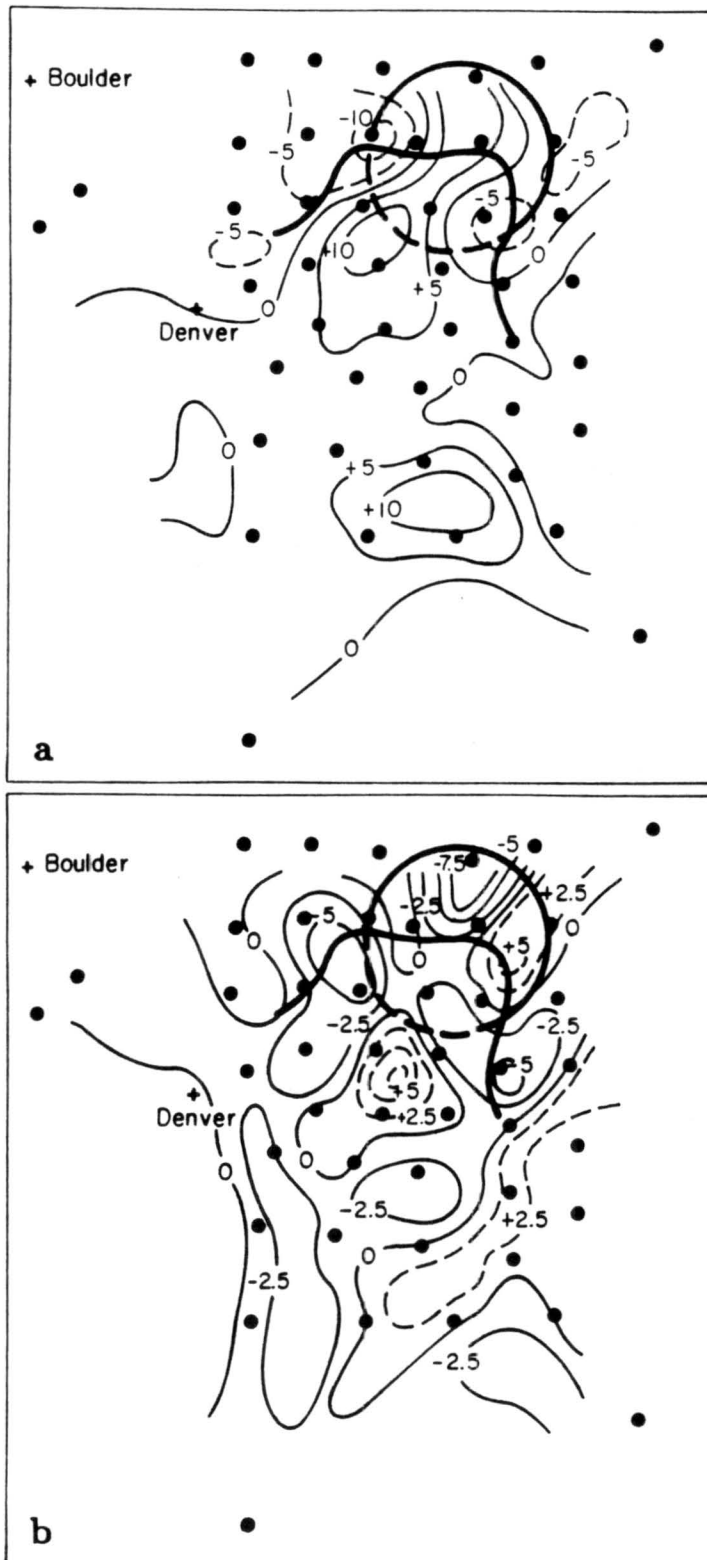


Figure 4.41: Divergence (a) and vorticity (b) fields associated with the gust fronts of 28 July 1987. In (a), the solid lines represent divergence and the dashed lines represent convergence ($s^{-1} \times 10^{-4}$), and in (b), the solid lines represent anticyclonic vorticity and the dashed lines represent cyclonic vorticity ($s^{-1} \times 10^{-4}$).

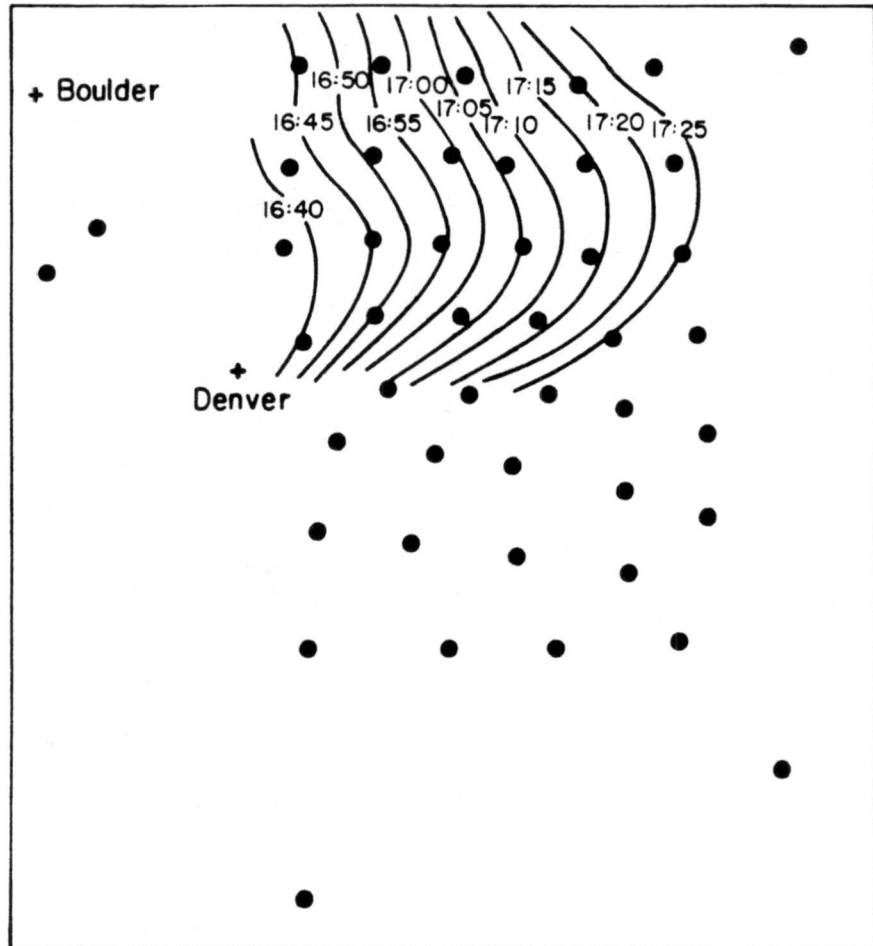


Figure 4.42: Isochrones of the leading edge of the gust front of 6 August.

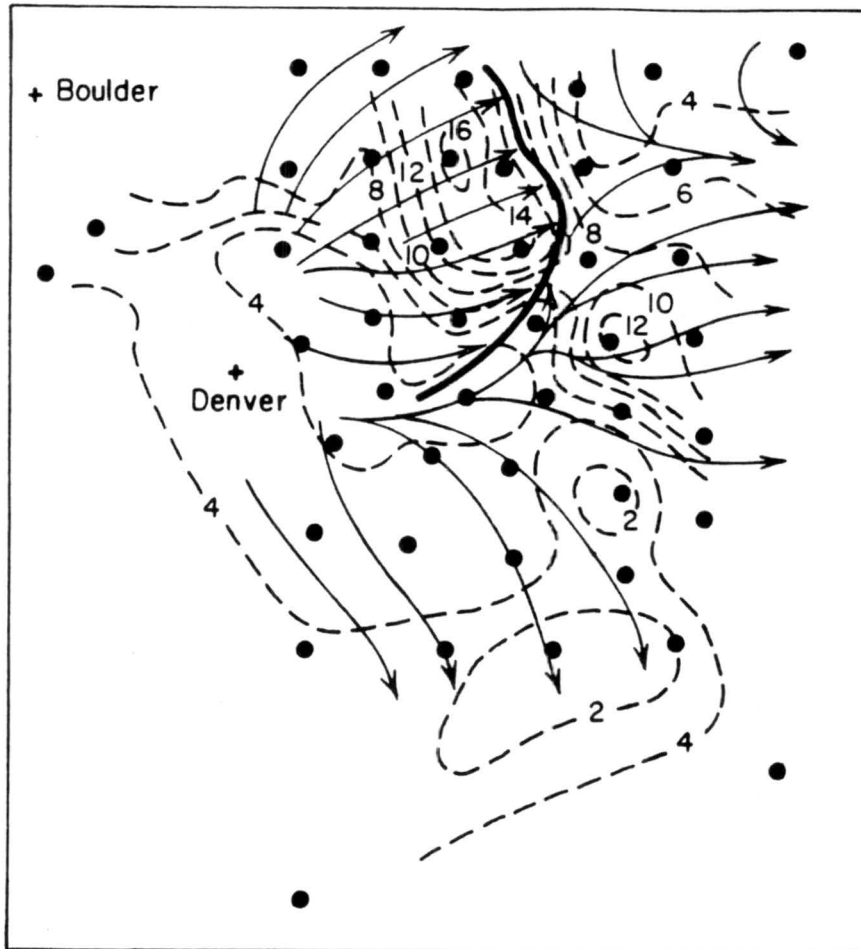


Figure 4.43: Streamline and isotach analysis at 17:10 on 6 August 1987. Streamlines are thin solid lines, isotachs are dashed lines in ms^{-1} , and the gust front is indicated by the thick solid line.

Surface analysis was carried out for this case at 17:10. By this time, the gust front had crossed the northwest half of the network. It is not known for how long the gust front had been in existence prior to this time, and so the lifecycle stage is unknown, but since the parent thunderstorm could not be located, it is suspected that either the cold source had already decayed, or else it was at such a distance that the radar could not see it. In either case, it seems that the outflow was simply a moving pool of cold air.

The streamline and isotach analysis of Figure 4.43 show what has been observed in the previous cases. Flow within the outflow was perpendicular to the gust front, and the wind

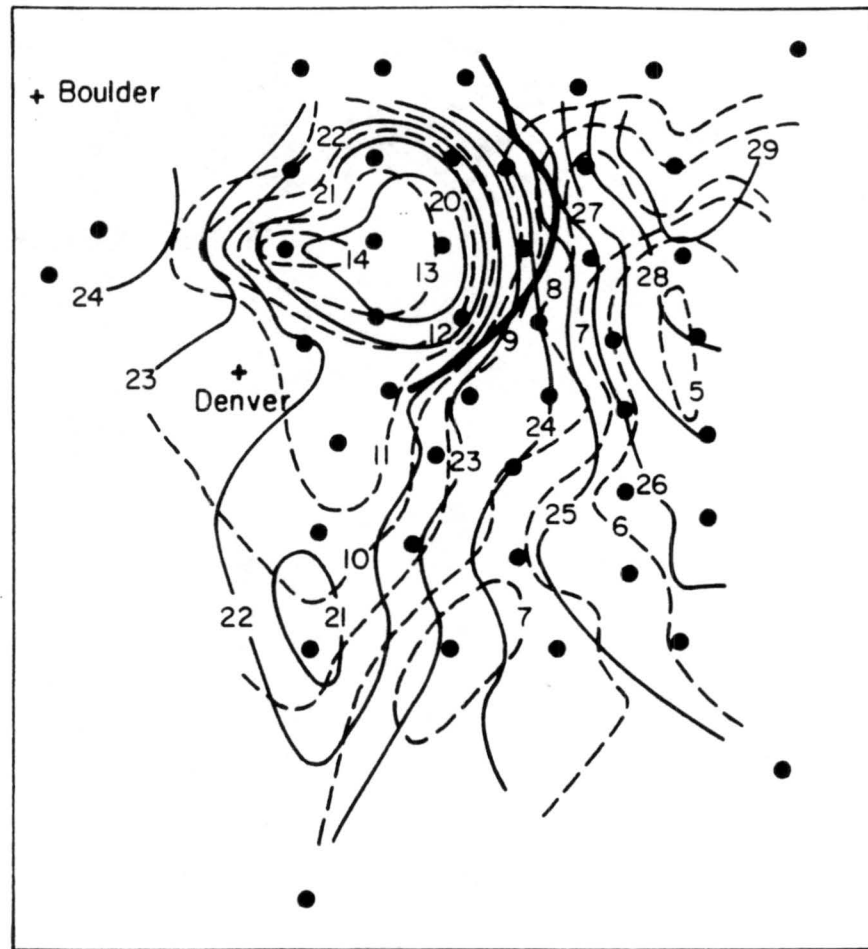


Figure 4.44: Dry-bulb and dewpoint temperature analysis associated with the gust front of 6 August 1987. Thin solid lines are isotherms in $^{\circ}\text{C}$, dashed lines are isodrosotherms in $^{\circ}\text{C}$, and the thick solid line is the gust front.

speeds behind the front are seen to be somewhat lower than the speed of the front itself. Again, the radar observed wind speeds were somewhat stronger than those observed at the surface. The gust front was marked by a steep gradient in the wind speeds at the surface, and ahead of the front, the environmental flow is in essentially the same direction as the gust front is moving.

The air and dewpoint temperature analysis of Figure 4.44 depicts the outflow quite nicely as a pool of cooler, moister air as compared with the environment. The gust front was well-defined as increased gradients in both dry-bulb and dewpoint temperature. The

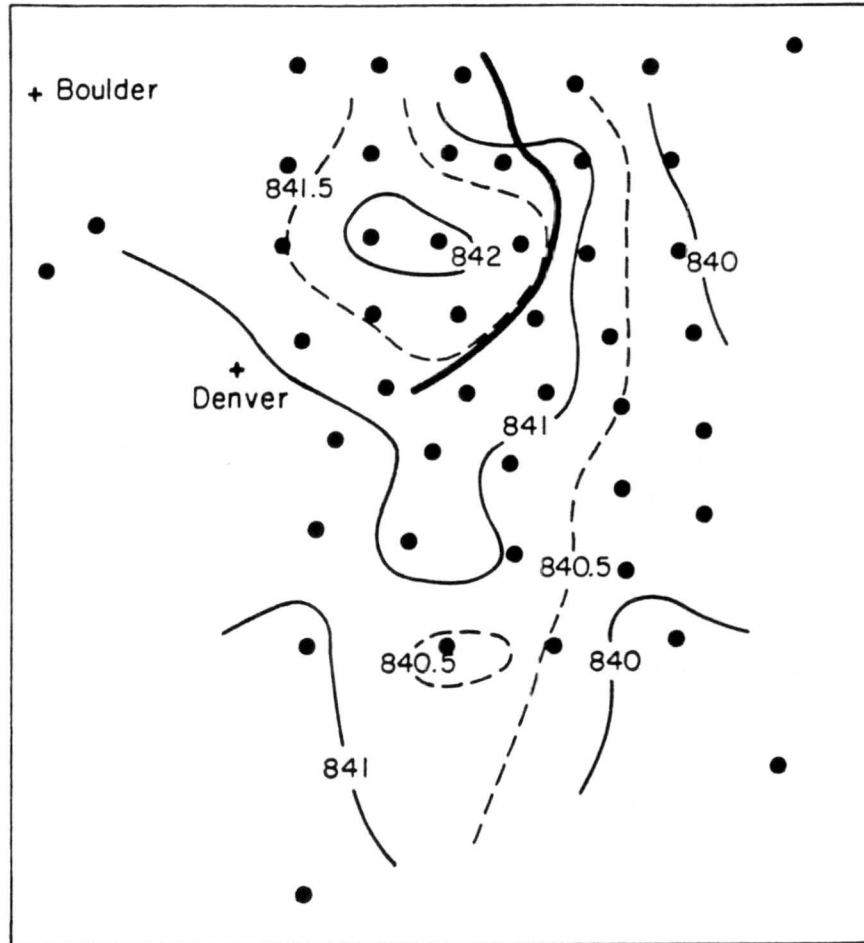


Figure 4.45: Surface pressure field associated with the gust front of 6 August 1987. Contours are in 0.5 mb increments with solid lines representing whole values and dashed lines representing half-values. Pressures have been adjusted to a mean height of 1594 m.

temperature drop across the front was on the order of 9°C , and the dewpoint rise was about $7\text{-}8^{\circ}\text{C}$. Both of these were the largest temperature changes of the four CINDE gust fronts. The pressure analysis (fig. 4.45) shows higher pressure in the outflow. The pressure rise associated with the gust front passage is also evident, with post gust front pressures on the order of 2 mb over environmental values.

The divergence and vorticity fields associated with the gust front are shown in Figure 4.46. The gust front was generally defined by enhanced convergence, with the outflow being characterized by divergence. The divergence along the south side of the front was due to

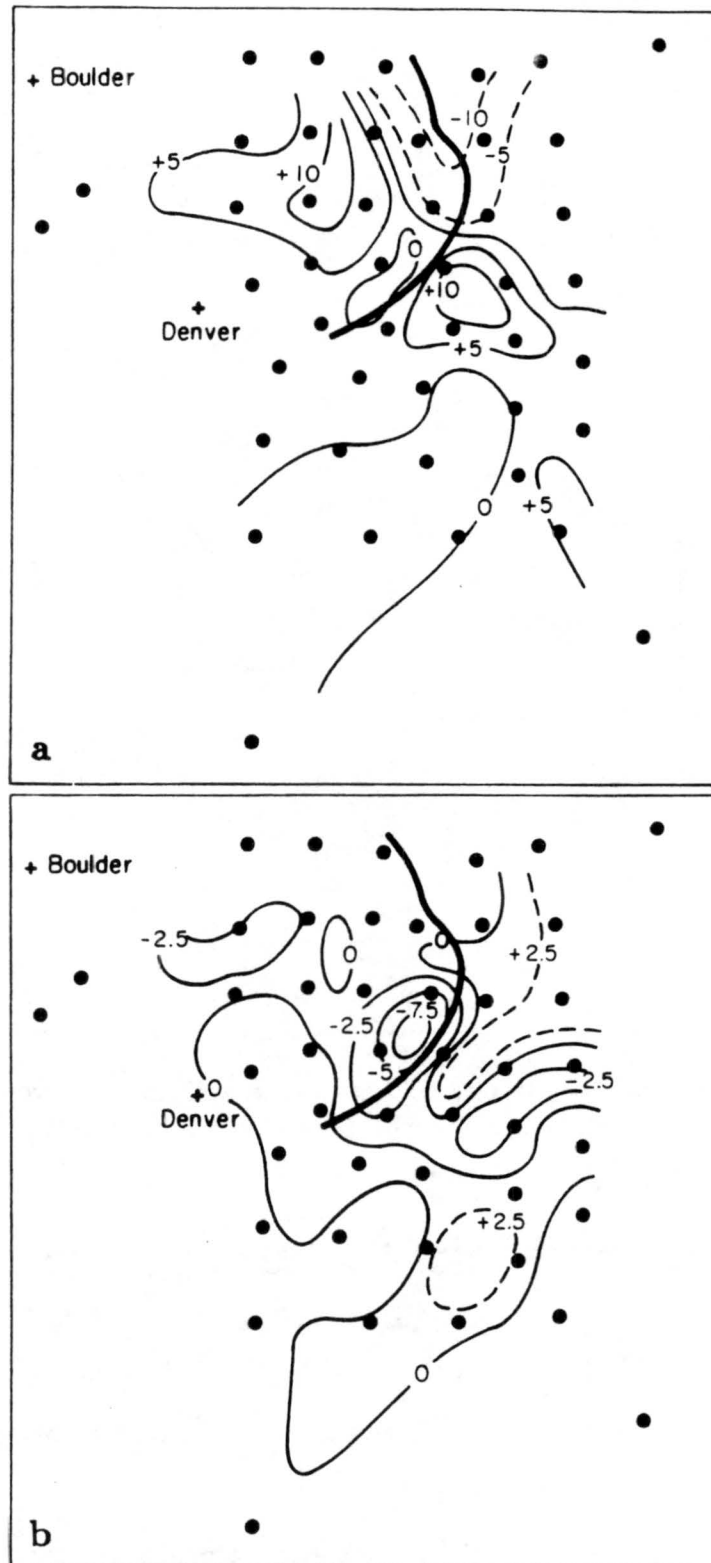


Figure 4.46: Divergence (a) and vorticity (b) fields associated with the gust front of 6 August 1987. In (a), solid lines indicate divergence and dashed lines indicate convergence ($s^{-1} \times 10^{-4}$), and in (b), solid lines indicate anticyclonic rotation and dashed lines indicate cyclonic rotation ($s^{-1} \times 10^{-4}$).

some directional divergence in that region which overcame any speed convergence that was occurring there. The vorticity field (fig. 4.46b) shows that the outflow was essentially non-rotational, but that there was some cyclonic rotation along the gust front. This cyclonic rotation has also been observed in the other cases, and it is these cyclonically rotating areas that have occasionally been observed in association with vortices along the gust front.

4.3 Summary

Table 4.8 summarizes the calculations for downdraft speeds of the five cases in this study. First, it is important to establish that the errors on these speeds are not of greater magnitude than the speeds themselves. With each of the tables in this chapter giving

Table 4.8: Summary of the average downdraft speeds calculated for the five cases in MIST and CINDE.

Date	\bar{w} (ms^{-1})	Outflow Configuration
14 July 1986	7 ± 2	Unidirectional
25 July 1986	5 ± 1	Unidirectional
31 July 1986	5 ± 1	Unidirectional
27 June 1987	12 ± 3	Radial
28 July 1987	11 ± 3	Radial

downdraft speed calculations for their respective cases, estimates of the error limits of the volume change of the outflow and the cross-sectional area of the downdraft were given. From these, error limits for the downdraft speeds followed, and these are also given in Table 4.8. It is noted that the possible errors in downdraft speeds for each case are within about 25% of the calculated values, lending credibility to the calculated speeds.

Having established that the errors do not swamp the results, it is next a question of whether or not the calculated downdraft speeds are reasonable. Referring back to Table 2.1, it can be seen that mean downdraft speed measurements from aircraft range from

2.5–12 ms^{-1} . Also, the work of Knupp (1987) showed that downdraft speeds in the mean are found within the range of 1–15 ms^{-1} . It is evident from Table 4.8 that the calculated mean downdraft speeds do indeed fall within the range that has been established by prior researchers. Again referring to Table 2.1, where the locations of the measurements are given, it can be assumed that Florida and Illinois measurements are representative of downdraft speeds of Alabama storms, and thus may be compared to the calculations for the MIST cases, while the N.E. Colorado measurements may be compared to the calculations for the CINDE cases. Again, it can be seen that the results in Table 4.8 agree well with the ranges of downdraft speeds given in Table 2.1 for each region of the country.

Table 4.8 also includes the type of outflow orientation for each case, either being a radial or a unidirectional outflow. Addis (1984), in his numerical modelling study of tropical outflows, observed different results for downdraft speeds, depending on which type of outflow the downdraft was driving. He observed that smaller downdraft air speeds are required to drive a unidirectional outflow, while larger speeds are required for radial outflows. His reasoning for this is that a downdraft driving a radial outflow must provide enough mass flux so that the air can spread out in all directions at the ground, while a downdraft driving a unidirectional outflow must only provide a flux great enough to produce a flow of air in one direction. The results of this study show that, indeed, the calculated downdraft speeds are smaller for the unidirectional outflows and larger for the radial outflows, and thus, are in agreement with the findings of Addis. So, from the above discussion, it appears that the assumption of mass continuity between the downdraft and outflow is a valid one. If there is mixing with and entrainment of environmental air, these processes do not appear to be significant.

In summarizing the surface analyses for the seven cases, it is noted that several features associated with a gust front and outflow are recurring from case to case. All of the cases show maximums in wind speed just behind the gust front, and this is why it is so named. The intensity of the wind speed gradient behind the front appears to indicate its strength, with the strongest fronts preceding the strongest wind speeds. The wind flow itself is perpendicular to the gust front in all cases, and when the environmental flow is not in the

same direction as the flow behind the gust front, a wind shift is noted just ahead of the gust front, continuing until the gust front passes. Another feature that is observed relating to the winds in the outflow is that the speeds behind the gust front are weaker right near the surface, and they increase with height in the outflow, before decreasing again up to outflow top. This maximum in wind speed above the ground is observable by the radar scans through the outflow depth, and it illustrates the frictional effects at the surface which tend to retard the flow.

All of the outflows are cooler than the environment through which they move, indicating the cooling that is occurring in the thunderstorm downdrafts. The moisture content of the outflow varies, however, depending on geographical location. For the MIST gust fronts, dewpoints fall off with gust front passage, since the environment in Alabama on thunderstorm days is characterized by high dewpoint temperatures. For the CINDE cases, the dewpoints rise with frontal passage because dewpoints are hard-pressed to get very high in Eastern Colorado, even on thunderstorm days. In addition to the observed temperature and dewpoint changes, a pressure rise is noted with the gust front passage, and the outflow pressures are higher than environmental values in all cases, due to the colder, denser air. In cases where a downdraft is present in the analysis, an even higher pressure area is observed in association with the thunderstorm high. As in the case of wind speed gradient, the intensity of the gradients of dry-bulb and dewpoint temperature and pressure are indications of the strength of the gust front, with the largest temperature and pressure changes occurring with the strongest fronts.

The divergence fields are consistent for all of the gust front-outflow cases. Enhanced convergence is noted usually along the entire length of the gust front as the faster moving cold air plows into the slow-moving environment. Because of this, the strongest fronts would then be expected to exhibit the largest convergence values, and this is observed. This convergence pattern is often responsible for maintenance of the parent thunderstorm or new convective development along the gust front. Enhanced convergence is also observed at gust front intersection points, targeting these intersections as possible areas of new convective development. The outflow is often characterized by some divergence when the gust front

has some curvature to it, and this occurs because the flow is perpendicular to the front, causing it to diverge from the outflow center. When downdrafts are present in the analysis, marked divergence is observed in these locations as the downdraft air rapidly diverges into the outflow. The vorticity fields are rather interesting. Both cyclonic and anticyclonic rotation is often observed along the gust front, especially in bends and clefts in the front. These areas may be possible areas of vortex development, depending on the strength of the rotational area. The downdrafts tend to be consistently anticyclonically rotating in all of the cases where downdrafts are observed in the analysis.

4.4 Gust front speed prediction

Several previous researchers have come to the conclusion that the propagation speed of a gust front is predictable because of its similarity to a density current, and theory on density currents has led to a relationship between the speed of the leading edge and certain characteristics of the current. From this, an empirical relationship for the propagation speed of the leading edge of atmospheric density currents has been determined, and this is given by Equation (2.2), with $k=0.75$. This relationship was applied to each of the seven gust fronts in MIST and CINDE for which surface data were available, so as to assess the accuracy of the relationship in predicting gust front speed.

Table 4.9 gives the results obtained from application of the density current approximation for atmospheric gust fronts. In all seven gust front cases, it is seen that Equation (2.2) underpredicts the propagation speeds, and in some cases, this underprediction is substantial. In four of the cases, Equation (2.2) underpredicts the speeds by as much as 50%, while for the other three cases, the underprediction ranges from 20–32%. The average for these seven cases is a staggering 37%. For the MIST gust fronts, the value of k for $v_{calc}=v_{obs}$ would have to be increased to an average of 1.20, and for CINDE to an average of 1.25. However, even if these averages for k were used, large errors would still result since the range of values for k is from 0.94 to 1.49. It is obvious that this equation is inadequate in predicting gust front speed, at least for the seven cases given here.

Table 4.9: Density current predictions for gust front speeds in MIST and CINDE.

Date		$\overline{\Delta p}$ (mb)	ρ_e (kg m ⁻³)	v_{calc} (ms ⁻¹)	v_{obs} (ms ⁻¹)	Error	k
14 July 1986		0.70	1.15	5.9	10.0	-41%	1.28
25 July 1986		0.81	1.13	6.3	8.1	-22%	0.96
31 July 1986		0.80	1.12	6.3	11.6	-46%	1.37
Avg							1.20
27 June	GF B	0.59	0.96	5.9	11.7	-50%	1.49
28 July	GF X	0.78	0.96	6.8	13.1	-48%	1.45
	GF Y	0.39	0.96	4.8	6.0	-20%	0.94
6 August		1.67	0.97	9.8	14.5	-32%	1.10
Avg							1.25

While it has been shown in studies on laboratory density currents that it is the pressure difference across the density current interface that drives the front, in the case of atmospheric density currents, there is airflow within the outflow that is moving faster than the front, and it must be responsible for some contribution to the gust front propagation speed. Also, Simpson and Britter (1980) showed that for an environment that is not at rest, there is some effect on the propagation speed of the gust front, either in retarding it or causing it to move faster than it otherwise would. They determined from several laboratory simulations, that a headwind reduces the speed of the density current by just over three-fifths, and a tailwind increases the speed by that amount. From these results, they modified Equation (2.2) to be written as

$$V = k\sqrt{\frac{\Delta p}{\rho}} + 0.62\bar{u}, \quad (4.1)$$

where \bar{u} is the environmental flow perpendicular to the gust front, being positive if flow is in the direction of gust front motion and negative if flow opposes gust front motion. Seitter (1983) applied Equation (4.1) to 20 gust front cases and found an average value for k of 0.79 for those cases. If Equation (4.1) is applied, with $k=0.79$, to the seven gust front cases in this study, some improvement over Equation (2.2) is noted, but the average error is still 20%, and as high as 32%. Because of this, it is proposed that Equation (4.1) be further modified to include contribution from the airflow within the outflow, so as to be written

$$V = k\sqrt{\frac{\Delta p}{\rho}} + 0.62(\bar{u} + \bar{v}), \quad (4.2)$$

where \bar{v} is the flow behind the gust front, and the same coefficient of 0.62 is also applied to \bar{v} , so as to retain as simple an equation as possible, then Table 4.9 is modified, with the new results for k given in Table 4.10. From surface data, the environmental flow ahead of the gust front can be determined, and radar data gives the wind speeds in the outflow behind the gust front. Radar data is used in determining \bar{v} because the flow at the surface is reduced by friction, and this is not representative of the actual flow within the outflow. The observed gust front speed was subtracted from the observed average wind speed in the outflow, so as to give values for \bar{v} relative to a motionless gust front. It is noted that this new value for k is fairly consistent for all seven gust fronts, with a range of 0.75–0.94. This

Table 4.10: Recalculations of k for the gust front speeds in MIST and CINDE from the modified density current approximation.

Date		\bar{u} (ms^{-1})	\bar{v} (ms^{-1})	v_{obs} (ms^{-1})	k
14 July		1.8	3	10.0	0.90
25 July		1.8	1	8.1	0.75
31 July		1.9	5	11.6	0.87
Avg					0.84
27 June	GF B	5.1	3	11.7	0.85
28 July	GF X	5.4	2	13.1	0.94
	GF Y	-0.7	1	6.0	0.91
6 August		3.5	1	14.5	0.89
Avg					0.90

is a significant improvement over the previous value of $k=0.79$, which had a range of 0.94–1.49 for these cases, and a range of 0.70–1.08 from previous research on gust front speed prediction.

If this new average for k of 0.87 is substituted into Equation (4.2), the modified density current approximation, then the results are given in Table 4.11. It is evident from these results that by including the flow in the environment and within the outflow, and by using

Table 4.11: Recalculations of MIST and CINDE gust front propagation speeds from a modified density current approximation and $k=0.87$.

Date		v_{calc} (ms^{-1})	v_{obs} (ms^{-1})	Error
14 July		9.8	10.0	-2%
25 July		9.1	8.1	+12%
31 July		11.6	11.6	0
27 June	GF B	12.0	11.7	+3%
28 July	GF X	12.4	13.1	-5%
	GF Y	6.6	6.0	+10%
6 August		14.2	14.5	-2%

the newly calculated value for k , the equation shows marked improvement in the prediction of the propagation speeds for all seven of the gust fronts, with five of the gust fronts exhibiting a reduction in error of between 30% and 47%.

An important thing to note in comparing Table 4.9 to Table 4.11 is that, as density current theory has shown, the pressure difference across the density current interface is important as a motive force to frontal propagation speed, but in the case of atmospheric density currents, the airflow in and around these outflows also contribute significantly to

the gust front motion. Referring back to the original calculations of Table 4.9, it can be seen that the largest errors in gust front prediction occurred for the cases of 31 July and 27 June, when either the downdraft was still very active or the environmental flow had a significant along front component (see Table 4.10). So it is concluded that, while the thunderstorm outflow is similar to a density current, some modification must be made to the density current approximation which takes into account other forces affecting the outflow, and then this modified density current approximation can be used as a predictive tool.

Chapter 5

CONCLUSION AND FURTHER RESEARCH

Doppler radar and surface mesonetwork data were used in this study to address two topics in the area of thunderstorm outflows and gust fronts. The first topic is a question of whether or not the assumption of mass balance for the downdraft-outflow system is a valid one, even though it has been used extensively in numerical modelling experiments but never actually tested, at least to the author's knowledge. The second topic addressed was the adequacy of the density current approximation in predicting gust front speed. A third focus of this study came as an aside, due to the good combination of Doppler radar and surface network data, and this was to present analyses from radar and surface data in order to show the characteristics typical of gust fronts and outflows.

Data were obtained from two programs that were designed for the study of thunderstorms and outflows. These programs are the **MI**croburst and **Severe Thunderstorm (MIST)** program of Summer, 1986, operated near Huntsville, AL, and the **Convective IN**itiation and **Downburst Experiment** of Summer, 1987, operated near Denver, CO. Both programs had associated research Doppler radars and instrumented surface mesonetworks, producing several gust front-outflow cases that were well documented by the data.

The mass balance assumption was tested by making measurements of the outflow volume rate of increase and the size of the downdraft from Doppler radar data. It was assumed that all mass flowing vertically within the downdraft was transferred to the outflow, with no loss through the sides or top of the outflow. The average downdraft speed was then calculated that would be required for the observed volume rate of increase to be realized. This was done for five downdraft-outflow cases. The calculations showed that reasonable downdraft speeds

resulted, as compared to previous measurements of downdrafts from aircraft and modelling experiments, from the assumption of mass continuity. In addition, the configuration of each outflow was noted, being either radial or unidirectional in nature, and the resulting calculations showed that stronger downdrafts are required to drive radial outflows than are required to drive unidirectional outflows, confirming the results of the numerical modelling study of Addis (1984).

In assessing the accuracy of the density current approximation, the empirical equation that has been derived for predicting gust front propagation speed by previous research was applied to seven gust front cases. The value of $k=0.79$, which has been agreed upon as a useful average for the Froude number for gust fronts, was used, and the hydrostatic pressure rise that occurs with a gust front passage was determined for each of the seven cases from surface mesonet data. The density current approximation proved to be inadequate in predicting the frontal speeds, with some errors as high as 50% lower than observed and an average error of 36%. Seitter (1983) had previously modified the density current approximation to include the effects of the environmental flow through which the gust front moves, and this equation was further modified in this study to also include the effects of the airflow in the outflow behind the gust front. The airflow behind the gust front was determined from radar data which scanned the gust front and outflow. The resulting recalculations produced a new value for k of 0.87, and this new value along with the modified approximation exhibited marked improvement in the frontal speed predictions. The largest error was 12%, and the average error was 5%. In comparing these results to the results from the unmodified density current approximation, it was obvious that the pressure difference across the front is indeed a primary force responsible for driving the gust front, but in the case of an active cold source and/or a significant along-front component in the environmental flow, large contributions to the gust front speed are supplied by these additional forces, and the Δp across the front may be responsible for only a little more than 50% of the gust front motive force.

Analyses from radar and surface data for the gust front-outflow cases of this study corroborated with previous analyses of thunderstorm outflows and gust fronts. The gust

front was found to be a zone of increased wind speed, temperature, dewpoint, and pressure gradients. These gradients were observed to be indicative of the strength of the gust front. Air flow in the outflow was noted to be perpendicular to the gust front in all cases, indicating the ability of a radar to observe the wind speeds behind a gust front when a radial is oriented perpendicular to the front. Convergence was characteristic of the entire length of the gust front, with the strongest convergence associated with the strongest fronts. Enhanced convergence was also noted at gust front intersection points. Some divergence was observed in the outflows behind curved gust fronts, as the air had to spread away from the outflow center so as to flow perpendicular to the gust front. The strongest divergence was observed in analyses where downdrafts were present. Vorticity fields associated with the outflow-gust fronts showed areas of rotation, both cyclonic and anticyclonic, along the gust fronts, mainly in bends and clefts in the fronts. Anticyclonic rotation seemed to be characteristic of all of the downdrafts that were present in the analyses.

The results obtained from this study show that the gust front is a predictable phenomena. If measurements, or even estimates, of the size and magnitude of a downdraft can be made, then an estimate as to how large its associated outflow will get and over what areas it might move can also be made. Measurements of the pressure difference across the gust front, once it has formed, and the wind speeds within the outflow and in the environment, can lead to predictions of how fast it will move. This is important since the gust front has been identified as a region of large horizontal wind shears, often as serious or worse than those associated with microbursts, which can be hazardous to aircraft during takeoff and landing procedures, and it has been shown that the gust front is instrumental in the development of new convection. By being able to predict where a gust front will move and how fast it will get there, better safety can be attained for aircraft operations and better short-range predictions can be achieved.

While it appears that, with a good degree of confidence, the mass balance assumption for the outflow-downdraft system is a valid one from the results of this study, better confidence could be achieved by comparing the calculated downdraft speed with observed speed of the same downdraft obtained from aircraft penetrations or the use of triple-Doppler radar data.

The density current approximation could also benefit from some further research. While the results of this study indicate the need for considering the outflow and environmental airflow when predicting gust front speed, the new value for k obtained here should be backed up by several more gust front cases. This continued research should help in making the gust front more easily predictable, hopefully in real-time.

REFERENCES

- Addis, R.P., 1984: A numerical model of surface outflows from convective storms. *Bound.-Layer Meteor.*, **28**, 121-160.
- Benjamin, T.B., 1968: Gravity currents and related phenomena. *J. Fluid. Mech.*, **31**, 209-248.
- Brown, H.A., 1960: Report on radar thin lines. *Proc. Eighth Wea. Radar Conf.*, Boston, Amer. Meteor. Soc., 65-72.
- Byers, H.R. and R. Braham, 1949: *The thunderstorm*. U.S. Government Printing Office, Washington D.C., 287 pp.
- Charba, J., 1974: Application of gravity current model to analysis of squall-line gust front. *Mon. Wea. Rev.*, **102**, 140-156.
- Droegemeier, K.K. and R.B. Wilhelmson, 1982: The roles of thunderstorm outflows in the production and maintenance of convection. *Preprints, 12th Conf. on Severe Local Storms*, San Antonio, Amer. Meteor. Soc., 516-519.
- Droegemeier, K.K. and R.B. Wilhelmson, 1985a: Three-dimensional numerical modeling of convection produced by interacting thunderstorm outflows. Part I: Control simulation and low-level moisture variations. *J. Atmos. Sci.*, **42**, 2381-2403.

- Droegemeier, K.K. and R.B. Wilhelmson, 1985b: Three-dimensional numerical modeling of convection produced by interacting thunderstorm outflows. Part II: Variations in vertical wind shear. *J. Atmos. Sci.*, **42**, 2404- 2414.
- Droegemeier, K.K. and R.B. Wilhelmson, 1986: Kelvin-Helmholtz instability in a numerically simulated thunderstorm outflow. *Bull. Amer. Met. Soc.*, **67**, 416-417.
- Droegemeier, K.K. and R.B. Wilhelmson, 1987: Numerical simulation of thunderstorm outflow dynamics. Part I: Outflow sensitivity experiments and turbulence dynamics. *J. Atmos. Sci.*, **44**, 1180-1210.
- Fulton, R.A. and D.S. Zrnic, 1985: Structure of a thunderstorm surface outflow from single doppler radar observations. *Preprints, 14th Conf. on Severe Local Storms*, Indianapolis, Amer. Meteor. Soc., 73-76.
- Goff, C.R., 1975: Thunderstorm outflow kinematics and dynamics. NOAA Tech. Memo., ERL NSSL-75, National Severe Storms Laboratory, Norman, OK, 63 pp.
- Goff, C.R., 1976: Vertical structure of thunderstorm outflows. *Mon. Wea. Rev.*, **104**, 1429-1440.
- Goldman, J.L. and P.W. Sloss, 1969: Structure of the leading edge of thunderstorm cold-air outflow. *Preprints, Sixth Conf. on Severe Local Storms*, Chicago, Amer. Meteor. Soc., 75-79.
- Greene, G.E., J.A. Korrell, and P.A. Mandics, 1977: An analysis of the gust-front hazard. *Preprints, Tenth Conf. on Severe Local Storms*, Omaha, Amer. Meteor. Soc., 151-153.
- Harris, F.I., K.M. Glover, and G.R. Smythe, 1985: Gust front detection and prediction. *Preprints, 14th Conf. on Severe Local Storms*, Indianapolis, Amer. Meteor. Soc., 342-345.

- Humphreys, W.J., 1914: The thunderstorm and its phenomena. *Mon. Wea. Rev.*, **42**, 348-379.
- Keulegan, G., 1958: The motion of saline fronts in still water. Nat. Bur. of Standards Rept., U.S. Dept. of Comm., Wash., D.C., 29 pp.
- Knupp, K.R., 1987: Downdrafts within high plains cumulonimbi. Part I: General kinematic structure. *J. Atmos. Sci.*, **44**, 987-1000.
- Mitchell, K.E. and J.B. Hovermale, 1977: A numerical investigation of the severe thunderstorm gust front. *Mon. Wea. Rev.*, **105**, 657-675.
- Mueller, C.K. and R.E. Carbone, 1987: Dynamics of a thunderstorm outflow. *J. Atmos. Sci.*, **44**, 1879-1898.
- Purdom, J.F.W., 1979: The development and evolution of deep convection. *Preprints, 11th Conf. on Severe Local Storms*, Kansas City, Amer. Meteor. Soc., 143-150.
- Purdom, J.F.W., 1986: Convective scale interaction: Arc cloud lines and the development and evolution of deep convection. Atmospheric Science Paper No. 408, Dept. of Atmospheric Science, Colorado State University, Ft. Collins, CO, 80525, 197 pp.
- Seitter, K.L., 1983: The effect of arc cloud generation on thunderstorm gust front motion. *Preprints, 13th Conf. on Severe Local Storms*, Tulsa, Amer. Meteor. Soc., 249-252.
- Simpson, J.E., 1969: A comparison between laboratory and atmospheric density currents. *Quart. J. Roy. Met. Soc.*, **95**, 758-765.
- Simpson, J.E., 1972: Effects of the lower boundary on the head of a gravity current. *J. Fluid. Mech.*, **53**, 759-768.

- Simpson, J.E. and R.E. Britter, 1980: A laboratory model of an atmospheric mesofront. *Quart. J. Roy. Met. Soc.*, **106**, 485-500.
- Sinclair, P.C. and J.F.W. Purdom, 1983: The genesis and development of deep convective storms. *CIRA Paper No. 1*, Cooperative Institute for Research in the Atmosphere, Colorado State University, Ft. Collins, CO, 80523, 56 pp.
- Sinclair, P.C. and J.F.W. Purdom, 1984: The genesis and development of deep convective storms: A new approach to their prediction and possible modification. *CIRA*, Cooperative Institute for Research in the Atmosphere, Colorado State University, Ft. Collins, CO, 80523, 47 pp.
- Sinclair, P.C., J.F.W. Purdom, and R.E. Dattore, 1988: Thunderstorm outflow structure. *Preprints, 15th Conf. on Severe Local Storms*, Baltimore, Amer. Meteor. Soc., 233-239.
- Srivastava, R.C., 1985: A simple model of evaporatively driven downdraft: Application to microburst downdraft. *J. Atmos. Sci.*, **42**, 1004-1023.
- Srivastava, R.C., 1987: A model of intense downdrafts driven by the melting and evaporation of precipitation. *J. Atmos. Sci.*, **44**, 1752-1773.
- Thorpe, A.J., M.J. Miller and M.W. Moncrieff, 1980: Dynamical models of two-dimensional downdraughts. *Quart. J. Roy. Met. Soc.*, **106**, 463-484.
- von Kármán, T., 1940: The engineer grapples with nonlinear problems. *Bull. Amer. Math Soc.*, **46**, 615-683.
- Wakimoto, R.M., 1982: The life cycle of thunderstorm gust fronts as viewed with doppler radar and rawinsonde data. *Mon. Wea. Rev.*, **110**, 1060-1082.

Weaver, J.F. and S.P. Nelson, 1982: Multiscale aspects of thunderstorm gust fronts and their effects on subsequent storm development. *Mon. Wea. Rev.*, **110**, 707-718.

Wilson, J.W. and W.E. Schreiber, 1986: Initiation of convective storms at radar observed boundary layer convergence lines. *Mon. Wea. Rev.*, **114**, 2516-2536.

Zrnic, D.S. and J.T. Lee, 1983: Investigation of the detectability and lifetime of gust fronts and other weather hazards to aircraft. FAA Final Rept. No. DOT/FAA/PM-83/33, 50 pp.

EM
201051